QUALITY CONTROL IN CONCRETE PAVEMENT: EARLY DETECTION OF NEAR-SURFACE HONEYCOMBING WITH GPR

by

Theresa Marie McCabe

A THESIS

Presented to the Faculty of
The Graduate College at the University of Nebraska
In Partial Fulfillment of Requirements
For the Degree of Master of Science

Major: Architectural Engineering

Under the Supervision of Professor Ece Erdogmus

Lincoln, Nebraska
December 2020

QUALITY CONTROL IN CONCRETE PAVEMENT: EARLY DETECTION OF NEAR-SURFACE HONEYCOMBING WITH GPR

Theresa Marie McCabe, M.S.

University of Nebraska, 2020

Advisor: Ece Erdogmus

This thesis presents utilization of Ground Penetrating Radar (GPR) for the assessment of highway pavements to gain a better understanding of this NDE method's capabilities in terms of early detection of consolidation-caused air voids in brittle materials. The objectives are to first, determine the earliest time during the dormant, setting, and early hardening periods of concrete's set that GPR can be used to detect shallow air voids. Secondly, the change in dielectric constant will be tracked over the first 24 hours of concrete setting in order to quantify the impact of the dielectric constant assumptions in early detection. Two different sets of experiments were conducted – the first to determine how early after casting GPR could be used to detect shallow air voids, and the second to track the change in dielectric constant over the first 24 hours of a specimen's lifetime. To accomplish the first objective, two reinforced concrete slabs were cast in the lab environment and two types of artificial air voids were implanted at different depths and locations. Type I voids were made of insulation foam sprayed into oblong and roughly circular shapes with dimensions of 2" x 1.75", 2" x 2.5", and 5" x 1". Type II voids were created by injecting pressurized air at different depths and locations, creating air voids of unknown size and shape. Using GPR, the presence of these two types of air voids was detected as early as three hours after pouring; their locations and depths could be mapped

out within an average error margin of 9%, 5%, and 19%, in the x, y, and z directions, respectively. Since this establishes a detection time earlier than any that has been previously reported in the literature, various post-processing and display techniques regarding color schemes and gains (other than those that are default and typically used, such as grayscale display) were tested and chosen to best identify the presence of air voids. The slabs cast and tested were cored to validate the GPR-based void locations. The work here presents the potential of GPR for early quality control of concrete pavements to minimize consolidation-related air voids and subsequent problems.

To accomplish the second objective, a third slab was cast without artificial voids implanted inside. A steel plate was laid at the base for calibration purposes, and the hourly change in dielectric constant was monitored and recorded for the first 24 hours after casting using GPR. It was found that the dielectric constant decreased at an average rate of 2.0% for the first 4.5 hours, 4.4% from hours 5.5 – 8.5, and leveled off between hours 10.5 and 13.5, before experiencing a drop and leveling off again at hour 15.5. Even though this concrete mix was different than the one used for the first two specimens, when the variation of dielectric constant is considered, the error margin previously established remains at less than 3%. The particular curve generated by the change in dielectric constant over time is unique to the specific type of concrete mix used in this experiment, however, similar curves can be constructed and for other mix designs. Should researchers or DOTs test specimens with mix designs they frequently utilize in highway pavement, they will have a growing archive of data and dielectric constant

curves for reference should calibration of GPR equipment in the field be necessary. This would allow detection of subsurface voids in fresh and setting concrete pavement to be accomplished quickly and accurately, mitigating the need to calculate two-way-travel while in the field to determine an accurate dielectric constant for void detection and provide a quality control resource for reference both in further research and on construction sites.

© Copyright by

Theresa Marie McCabe

2020

DEDICATION

For Jo, Mike, Ann and Jim.

ACKNOWLEDGEMENT

I would like to express my deepest thanks to my advisor, Dr. Ece Erdogmus, for her constant insight, support, guidance, and help. My graduate school experience would not be the same without her. I also thank Dr. George Morcous and Dr. Jiong Hu, for both their insight and willingness to serve on my committee. I would also like to thank Antony Kodsy, for all his assistance in my experiments and teaching me the ways of GPR.

The Nebraska Department of Transportation (NDOT) is acknowledged for the financial support and opportunities they provided, especially by Ms. Lieska Halsey and Mr. Wally Heyen.

Thanks also to Dr. and Mrs. McCormack, for their excellent suggestions and help.

Without my amazing family and friends, I would not be where I am today. Thanks a million especially to my awesome parents and all my fantastic siblings, who have motivated and supported me every step of the way.

Table of Contents

List of Figures

List of Tables

List of Equations

Chapter 1. Introduction

Poor consolidation can cause potholes and spalling, two of the problems Departments of Transportation (DOTs) encounter when dealing with concrete pavement. Improper consolidation results in entrapped air voids (i.e. honeycombing) beneath the surface of pavement, which, after multiple freeze-thaw cycles can develop into potholes and/or spalling – potential driving hazards. Patching these areas after the construction crews leave the site is a costly and time consuming process, in addition to being inconvenient for commuters. The early detection of honeycombing, therefore, allows DOTs to identify pavement sections exhibiting signs of poor consolidation during construction to avoid its spread and repair them before larger sections of pavement are affected and repairs become necessary.

Early detection of these consolidation-caused air voids is possible through the use of Ground Penetrating Radar (GPR), which is a Non-Destructive Evaluation tool (NDE). GPR has been used for reinforced concrete delamination detection and concrete quality control since the 1980s, due to both its mobile method of testing and ease of use (Fernandes and Pais, 2017), although not for the early detection of relatively small voids. The early detection of air voids has been thought to be impossible using GPR due to the scattering effects of moisture in fresh concrete on GPR's electromagnetic waves.

In comparison to other traditional highway pavement condition detection methods, GPR is unique in its ability to provide continuous and nondestructive measurements without

disturbing the pavement surface and structure, and assess subsurface cross-sectional areas quickly (Liu, 2008). Hypothetically, GPR could be used for the detection of honeycombing early in the lifespan of the pavement, while construction crews are still on site. This thesis' aim is to push the thus-far assumed limitations of the use of GPR on fresh concrete pavement for honeycombing detection, as well as track a concrete specimen's change in dielectric constant over its first 24 hours.

To test the first aim of this study, different sized artificial voids were created in laboratory slabs using spray insulation foam, a material with a similar density to naturally occurring air voids. These slabs were then scanned with GPR at varying time intervals after pouring. Two slabs with different dimensions and reinforcement were tested with void depths and configurations varying to test the sensitivity of the measurements to void size and depth over time. NDOT's typical pavement mix was used to cast the slabs: 47B Concrete Pavement Mix with 2" (5 cm) slump. This was done in order to ensure that laboratory specimens were as similar to field pavement as possible. Specimens were scanned both with and without NDOT's typical curing compound sprayed on top of the slab. GPR scanning began on a 4" x 4" (10 cm x 10 cm) grid, and later transitioned to a 2" x 2" (5 cm x 5 cm) grid for improved accuracy, as the smallest voids used during experimentation were roughly 1" (2.5 cm) in diameter. Scan gridlines were initially stenciled directly onto the top of the slab with chalk. In later stages, a plastic sheet with gridlines outlined was used for ease and repeatability of scanning. To avoid stripping the curing compound off of the slab surface during early scans, a 4" x 4" (10 cm x 10 cm)

plywood sheet was laid out with scan gridlines traced on the top face. Four 1.25” (3.18 cm) long screws were inserted into each corner, creating a scanning grid with the bottom elevated 0.5” (1.25 cm) above the surface of the concrete, rather than lying directly on top of it. This modified scanning grid was tested in the laboratory environment after the 24 hour mark had passed and was found to adequately detect voids. Then, it was taken to a section of road that was six weeks old and used to scan three 4” x 4” (10 cm x 10 cm) sections of pavement on site where no voids were detected, leading to the conclusion that the section was adequately consolidated.

To test the second aim of this study, a smaller 36” x 48” x 4” (0.91m x 1.22m x 10.16cm) was cast. Quickcrete High Strength concrete mix with a 7” (17.8 cm) slump was hand mixed and poured into the prepared formwork. Due to the high slump, the specimen did not require vibration for consolidation. A 23” x 23” (58.4 cm x 58.4 cm) steel plate with a 4” (10.16 cm) diameter hole in the center, rather than reinforcement, was used for scanning calibration purposes and was centered at the base of the formwork. No artificial voids were used in this slab, as its primary purpose was for tracking the changing dielectric over the specimen’s first 24 hours using GPR. This slab was scanned hourly at 2” (5.08 cm) o.c. starting 90 minutes after casting using the same handheld GPR device as the first two slabs. The plastic stencil used in earlier specimens was used in lieu of the elevated plywood stencil, as it did not became destabilized or cause cosmetic damage in the first 4.5 hours after casting. As the destabilization and damage caused by the elevated plywood stencil was likely a result of the mix’s high slump, utilization of the elevated

stencil would be feasible and recommended for a mix with lower slump or following 5 hours after casting for a mix with high slump.

Chapter 2. Goals and Objectives

There are advantages in scanning and detecting honeycombing at three or four hours after pouring. Air voids of greater than 1.25” in diameter are visible in GPR scans this early in the curing process, meaning that DOTs can anticipate which sections of pavement might have to be replaced or patched in the future. The early detection of air voids can then be used as a quality control method to ensure consistent mix design and that pavement is meeting predetermined quality control standards. Therefore, the goals of this thesis are twofold. First, to develop a practical method for detecting near-surface air voids (honeycombing) in concrete pavement early using GPR. In this case, “early” is taken to mean the time period before 24 hours has elapsed following the concrete’s initial set. Secondly, this thesis will examine the dielectric constant’s change over the first 24 hours of a concrete specimen’s lifetime.

The tasks to achieve the first objective will include a literature review, followed by laboratory experiments determining detection accuracy of voids, as well as void size, shape, and orientation limitations. The developed procedures will then be investigated in field trials. Tasks for achieving the second objective will include a literature review, casting of a laboratory specimen, hourly scanning, and post-processing of GPR scans.

Chapter 3. Literature Review

This will first review past published research on the fundamentals of GPR theory and its applications, specifically in relation to concrete. Then, the consolidation process of concrete, the importance and difference between entrained and entrapped air voids will be discussed, as well as the relationship between each to the deterioration of concrete roadways. The application of GPR in detecting deterioration in concrete roadways will then be discussed. The long and short term benefits of early detection and case studies will also be briefly discussed.

3.1. GPR Theory and Applications

GPR is a nondestructive testing method which uses radio waves to probe materials with low dielectric loss. Originally, GPR was mainly used on naturally occurring geologic materials such as glaciers, but its use has expanded to include archeological, forensic, geophysical, and infrastructural materials, including concrete roadway and asphalts. The combination of the number of low loss materials and the range of radio frequencies available means that GPR can be used in many different applications. GPR can be used to test roadways in a scale of centimeters, and the same methodology can be used to test deep foundations or geologic stratigraphy on a greater scale of meters using a different antenna frequency. GPR's wide applicability makes it a flexible tool in that its use is not limited to one sector of industry – it can be used in construction quality control, for structural analysis and pre-intervention, as well as in geophysical applications.

To function, GPR requires both emitter and receiver antenna elements; bi-static systems have separate emitter and receiver antennas, while mono-static systems use the same antenna for emission and reception of signals. In many cases, the emitting and receiving elements (whether bi-static or mono-static) are set in a fixed orientation or location on a portable device and are moved over the ground to detect energy reflections from the subsurface. Beginning as a tool used to sound ice sheets in glaciers using airplane radar altimeters in the 1950s, to sounding soil and rocks in the 1960s, the use of GPR for nondestructive testing purposes continues to grow.

3.1.1. Radar

GPR is a non-invasive tool designed for detecting changes in electrical properties below the surface of what is the antenna is scanning (Comas et al., 2004; Neal, 2004). More specifically, a GPR system uses high energy electromagnetic (EM) energy pulses, usually between 10 MHz and 1 GHz, emitted and received by antenna to detect electrical property changes “below-ground” (Holden et al., 2002; Jol and Smith, 1991, Neal, 2004). Because the ground is rarely an absolutely homogenous material, as the EM wave propagates into the subsurface, it encounters other materials present, each with different electrical properties than that of their surrounding material. Electrical conductivity and permittivity are the two physical properties that govern how radar energy responds to the materials present. Permittivity, as a material property, measures how well an external electrical field can pass through a material. When an electrical field is applied to a material with high permittivity, the material will store more energy in its electric field.

Alternately, a material with low permittivity will not store as much electrical potential energy.

As GPR's EM waves move through the ground, they attenuate and are naturally absorbed by the surrounding material as they move through the subsurface (Geophysical Survey Systems, 2001). The electrical conductivity of a material, then, is a measure of how resistive a material is to EM wave propagation. Resistive materials such as very dry soil or concrete have low conductivity – the GPR signal does not experience excessive attenuation through the subsurface and therefore is able to penetrate deep into the material. Conductive materials such as saltwater or wet concrete absorb the GPR signal before it can travel deeply into the material (Geophysical Survey Systems, 2001); the presence of water consequently plays a large role in how GPR EM signals will attenuate in the subsurface. The dielectric constant is a measure of how much electrical charge can be stored in a material, and how fast the radar signal will travel through a material (Geophysical Survey Systems, 2001). The equation for calculating the dielectric constant of a material can be found in Equation 1.

$$k = \frac{E_0}{E} \qquad \text{Equation 1}$$

Where *k* is the dielectric constant of the material, *E* is the permittivity of a vacuum, and E_0 is the permittivity of the material being scanned. The permittivity of the scanned

material, therefore, is an important property to know to understand how EM waves are propagating through the material.

When the EM wave propagating through the subsurface encounters a difference in dielectric constant between the ground and a second material, part of the wave is reflected back to the receiving element and detected. More specifically, if there is an interface with a difference in water content between the ground and a second material, EM waves are reflected back to the receiving element (Comas et al, 2005). As a result, the quality of the results from GPR scanning depends strongly on the subsurface where scanning occurs (Daniels, 2004). For example, a wet material will yield very different results in terms of wave penetration than that of a dry material.

As previously mentioned, radar systems have emitter antenna which propagate EM waves of different frequencies. Low frequency EM waves penetrate deep into the subsurface and detect larger changes in material, whereas higher frequency EM waves have a shallower penetration, but are capable of detecting smaller objects due to their shorter wavelengths. EM waves are not emitted at a single frequency, but across a spectrum, which propagate from the emitter antenna at the surface into the ground. There, they experience delay in returning to the receiver when they scatter or attenuate further into the ground. Two-way travel-time (TWT) is the time it takes the waves to leave the emitter and be detected by the receiver. Typically, TWT is measured in nanoseconds and depends both on its velocity and the depth the wave travels before it is reflected (Jol and

Smith, 1991; Neal, 2004). The velocity of the wave's propagation can be calculated using Equation 2, where *c* is the speed of light (300 mm/ns) and *k* is the dielectric constant.

$$v = \frac{c}{\sqrt{k}} \qquad \text{Equation 2}$$

GPR's output is a continuous cross section of the ground, with horizontal distance versus vertical TWT. Vertical TWT uses the propagation velocity (Equation 2) to determine the depth of the material in the ground's subsurface (Equation 3).

$$d = v \times t/2 \qquad \text{Equation 3}$$

In Equation 3, *d* is the depth of the second material, *v* is the velocity of the wave's propagation, and *t* is the vertical TWT. The velocity of the wave's propagation can be found by scanning a material with a deflecting material at a known depth, and then using the TWT and depth to solve for the velocity. Once this is done, other materials with unknown reflecting materials' locations can then be accurately tested to find their embedment depth.

The receiving system of the antenna, as previously stated, will either be a separate antenna (bi-static system) or will be included in the same antenna as is emitting signals (monostatic systems). Depending on the wavelength and the site limitations, the distance between the emitter and receiving antenna should be as small as is possible – the

resolution of the depth of the interface at the second material decreases as the distance between emitting and receiving elements increases (Ruffell, 2013). There are advantages to either configuration depending on the situation: monostatic systems have no separation between the antennas, which is both convenient for operators and easy to use while having no distance between emitter and receiver. Bi-static systems, on the other hand, can be useful for common midpoint sounding (CMP) and wide angle reflection and refraction (WARR) surveys. CMP and WARR surveys measure TWT changes while increasing the distance between emitting and receiving systems by a set distance (Annan, 2005; Jol and Bristow, 2003; Ruffell, 2013). Although the embedded material's depth resolution decreases as the distance between the antennas increases, the effect does not become significant until the distance between emitter and receiver reaches half of the embedded material's depth (Jol and Bristow, 2003; Ruffell, 2013). For many environmental studies such as glacial, fault lines, coastal, and peatland, bi-static systems are common, although they can have either a fixed or changeable distance between emitter and receiver elements (Annan, 2005; Jol and Bristow, 2003).

Once the signal has been reflected back and is detected by the receiving element, the strength of the EM reflection detected is proportional to how strong the contrast is between the ground and the second material present. The frequency of the antenna plays a huge role in how deep the EM waves can penetrate the ground and the strength of the resulting output's resolution. Low frequency waves do not attenuate as easily as high frequency waves, allowing them to penetrate deeper into the ground. However, the

resolution of high frequency waves is stronger than low frequency waves as they detect and reflect fine characteristics below-ground much better than low-frequency waves (Ruffell, 2013). As a result, antenna choice is often decided by prioritizing either depth or resolution; the rule of thumb is to choose depth, as higher resolution scan outputs are useless if the material embedded in the ground cannot even be found (Annan, 2005; Harari, 1996).

After the signals have been received and processed, and the subsurface of the ground displayed, the data must be processed to interpret the output scans. There are a few steps, which can make data processing and interpretation straightforward when interpreting GPR data, provided they are followed consistently and systematically. Filtering and data correction editing are two of the basic processing steps usually necessary to begin interpreting data correctly. Data editing includes time-zero corrections, background subtraction, and gain adjustments, among other options, depending on the make and model of the system. Time-zero corrections are typically the first step in data processing, and are vital for accurate shallow detections, as their resulting realignment causes all the subsurface reflections to be correctly aligned (Ruffell, 2013). Once this has been accomplished, other data editing and filtering can be used to improve the visual output scans for ease in reading and interpretation. Because waves signals attenuate quickly as they propagate below-ground, it can be difficult to clearly detect material changes at deeper depths (Annan, 2005). Gains enhance the appearance of later arriving waves, which can be caused by signal attenuation and geometric losses and can be defined by the

user or done automatically (Cassidy, 2009; Ruffell, 2013). Filtering done before adjusting the gain works with the data in its purest form and does not have to be complex to remove noise caused by high or low frequencies (Cassidy, 2009; Ruffell, 2013). Removing noise caused by users or the system helps to improve the readability for the user, leading to a quicker, more accurate interpretation of data.

Concrete as a material is not completely homogenous by nature, being a mixture of aggregates, hydrated cement paste (hcp), and entrained air voids. As a result, as the EM waves propagate into the concrete's subsurface, it encounters the interface between the various constituent materials present, each with different electrical properties than that of the surrounding material. Filtering and data correction are useful tools when dealing with scan outputs for concrete, due to the noise level caused by the interface between the different materials. GPR scans of setting concrete require even more care in processing, gain decisions, and filtering, as the difference in water content between the materials in the concrete is much higher.

3.1.2. Material Properties

In most GPR applications, changes in the dielectric permittivity and magnetic permeability are important, but it is not critical if a change in electrical conductivity occurs. In terms of scanning with GPR, an electrical conductivity if 0 would be ideal; a low electrical conductivity indicates a low loss material, as signals can penetrate deeper than in higher loss conditions. Higher loss conditions include areas with either salt and/or

water present – the water present limits the penetration of GPR signals, as it has a much higher dielectric constant than the surrounding materials. Ideal low loss conditions are not usually present in practice. For example, a GPR scan of beach sand yields between 20% and 40% of the volume to be air, water, and dissolved ions. Water and ice are two of the few cases where nearly all, if not all, of the material present is homogeneous. The proportion of the components of the mixture typically does not proportionally determine the properties of the material (Jol and Bristow, 2003).

The combination of materials that make up "the ground" can be soil, asphalt, concrete, steel, or other materials, but whether or not water is present during scanning plays a large role in how materials generally behave. The range of dielectric constants varies from 1.0 to 81. Figure 1 shows ranges of dielectric constants for common materials.

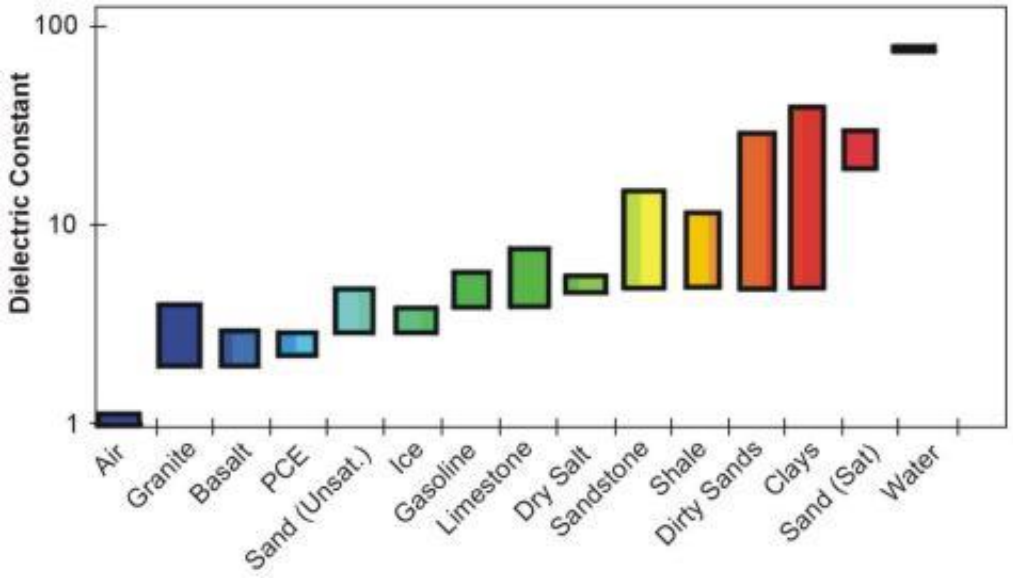

Figure 1: Dielectric Constant Ranges for Common Materials (Wightman et al., 2003)

Water has a high dielectric constant – usually around 80. In comparison, air has a dielectric constant of approximately 1.0 – the lowest possible – and is likely to vary little because of moisture in the air. On the other hand, bulk aggregates usually are between 3 and 8, which make them generally good dielectric insulators as they have almost no conductivity. Table 1 lists some typical dielectric constants for materials. The dielectric for concrete changes over time as it cures, starting on the higher end for concrete (around 12) and decreasing as it cures.

Table 1: Common Material Dielectric Constants

Material	Dielectric Constant
Vacuum	1.00000
Air (dry)	1.00059
Paper	3.6
Ice	3 – 4
Limestone	4 – 8
Concrete (dry)	6
Concrete (wet)	12
Water	80

Construction materials, soils, and rocks have tiny air pockets in between their grains, which can be filled with air and water. When water is in these air pockets, it contains ions, whose mobility is the dominant factor when determining the electrical conductivity of a bulk material. As a result, the conductivity of soil and rock when water is present in their air pockets will be very different than when no water is present. Because water is more than likely present in naturally occurring geologic materials' air pockets, its presence plays a large role in determining the electrical properties of each material.

3.1.3. Interface interaction

The detection of reflected and refracted signals is what GPR depends on to successfully create an image of what's going on under the ground. GPR's emitting antenna generates a cone-shaped EM pulse which travels through the material and either reflects off of or scatters off below-ground changes in material. The receiving antenna on GPR equipment then captures the energy as it travels back to the surface, as previously mentioned. TWT is the time it takes for the EM energy to travel from the emitter to the change in below-ground material and back from the receiver, and is used to calculate the propagation velocity of the below-ground change in material. When an EM wave comes into contact with a material with different electromagnetic properties than the material surrounding it, a part of the wave will scatter upon contact.

There are four different types of possible reflection scattering: spectral reflection scattering, refraction scattering, diffraction scattering, and resonant scattering. Spectral reflection scattering is the main type of scattering observed in GPR scans, but more detail on the other three types of scattering is available by reviewing Daniels et al. (1995). Based on the law of reflection, spectral reflection scattering describes a situation where the angle that the wave hits the interface is equal to the angle at which the wave reflects off the interface, and therefore back to the receiving antenna.

3.1.4. Concrete Setting and Consolidation

Inadequate concrete consolidation can be caused by under or over-vibration, long wait times between batches, or an overly dry mix. As previously mentioned, improper consolidation has decreased strength and durability implications, so adequate vibration is vital for concrete pavement to perform as designed for its lifetime. Entrapped air voids larger than 1" in diameter can cause premature spalling and deterioration in pavement. The adequate consolidation of concrete through proper placement and vibration allows entrapped air to escape and entrained air to be evenly distributed throughout the mix. This properly and evenly distributed entrained air then provides the freeze-thaw resistance necessary for long-term concrete durability. But in the early stages of concrete curing, before the concrete is even exposed to any freeze-thaw conditions, there are three stages characterized by the cement particle setting and curing. The first stage is the dormant period, which extends to approximately 4 hours after pouring. The setting period begins after the dormant period and lasts approximately 8 hours. After the setting period, the concrete enters the hardening period, which continues for the remainder of its lifetime.

Scanning concrete with GPR while the specimen is still in the dormant and setting periods brings complications not present in the scanning of older concrete. The water present in fresh concrete, as previously mentioned, can make interpreting GPR scans difficult due to the moisture and scattering effects on EM waves. Weaker signals caused by GPR detecting voids may also be harder to see when scanning occurs soon after

pouring. Regardless of how early scanning occurs, the presence of evenly-distributed entrained air voids rather than entrapped air voids throughout the specimen is ideal for the best possible specimen strength and durability.

3.2. Fresh Concrete and its Mechanical Properties

The general behavior of concrete is important to understand before going into detail on air void properties, because how larger samples of concrete behave during mixing impacts its entrained and entrapped air on a smaller scale. The main properties of interest in concrete are its fluidity, compactability, and stability (or cohesiveness). These three factors will play an important role when consolidation occurs. Fluidity is the ability of the concrete to be handled and flow around reinforcement in formwork during placement; compactability refers to the removal of the entrapped air by compacting machines (such as vibrators) during mixing and handling; stability, or cohesiveness, refers to the necessity of concrete to remain homogenous and unseparated.

Fluidity and compactability can be combined under the term “consistence”, which can be hard to measure quantitatively. ACI’s defines it as “that property of freshly mixed concrete or mortar, which determines the ease and homogeneity with which it can be mixed, placed, consolidated, and finished” (ACI, 2000; Soutsos and Domone, 2018). Meanwhile, ASTM defines it as “That property determining the effort required to manipulate a freshly mixed quantity of concrete with minimum loss of homogeneity”

(ASTM, 1993; Soutsos and Domone, 2018). While both these definitions are helpful in that they state the requirements in the general sense, they do not reference any mechanical properties, such as the modulus of elasticity.

Yield stress and plastic viscosity are independent properties of each other, and changing mix ingredients and proportions can lead to different combinations of the yield stress needed to overcome particle bonds and the plastic viscosity. These values can affect consistence and fluidity of the concrete mix. More fluid mixes tend to have lower yield stresses and plastic viscosities, since a reduction in yield stress leads to a reduced resistance to flow when shear stresses are low, which can in lead to less entrapped air during vibration. The entrained air bubbles that result from proper vibration and mixing are necessary for durability and strength of the concrete.

Durability, in this case, is the ability for the concrete to remain operational and functional for at least its designed lifetime, given reasonable and regular maintenance. The durability of materials depends on the level of degradation it is exposed to – whether that comes from the surrounding environment or internally. An external source of degradation could be damage caused by water freezing at joints and cracking the pavement from the exterior, whereas an internal source of damage could be a chemical reaction between alkali and aggregates present. What internal and external degradation factors have in common is that the rate of both actions is controlled by how fast and deep moisture and air can penetrate into the concrete. This penetrability of concrete is one of the main factors when considering durability. As previously mentioned, hcp and concrete both

contain air voids of varying shape, size, and orientation – these air voids can be considered “pores”. Therefore, the flow of moisture or air through concrete can be considered a case of flow through a porous material (Soutsos and Domone, 2018). Their rate of flow depends not only on the concrete’s porosity, but also on the size of the pores and their continuity, since they will not flow through a pore less than 150 nm in diameter (Soutsos and Domone, 2018).

3.3. Entrained Air Voids

Since the 1930s, the entraining of air in concrete has been used to resist freezing and thawing as well as meet minimum strength requirements (Ozyildirim, 2004). Air voids ideally must be small in size and closely spaced, to provide a network of space for ice to expand into so as to not damage the surrounding concrete. This is especially vital in roadways, as they are exposed to freeze and thaw cycles throughout their lifespan, and must last a sufficient amount of time to be worth the investment. Most entrained air voids are irregularly shaped and larger than 1 mm (Ozyildirim, 2004); however, poor consolidation during pouring can cause them to be much larger and range up to 2.5 cm or larger, around the size of the small voids tested in this thesis’ experiments. The issue of consolidation arises during vibration – many air voids are caused during the course of vibration, whether it’s due to over-vibration, which causes the coarser aggregate to sink to the bottom of the concrete and the more fluid cementitious portion to rise to the top, segregating the mixture and compromising strength and durability. Alternatively, in under-vibration, insufficient entrained air that compromises strength and entrapped air

pockets are present throughout the concrete. (Soutsos and Domone, 2018). As a result, proper consolidation is an important and necessary step in the concrete casting process.

The durability of concrete directly depends on its porosity, which is considered one of the most important elements influencing its ability to perform over its intended lifespan (Soutsos and Domone, 2018). Porosity describes the ability of the aggregates to absorb and hold water in their pores. All aggregates have pores, and the amount of water stored in them prior to mixing causes them to fall into one of four categories.

Category 1 describes a completely dry aggregate, where all the pores are empty. Category 2 describes air dry aggregate, which is partially saturated – the pores are partially filled with water. Category 3 describes a fully saturated aggregate with a dry surface (SSD); all the pores are full, but there is no excess water on the aggregate. Category 4 describes wet aggregate, where there is excess water and all the pores are full of water. Type 3 is ideal, although challenging to achieve when not in a lab environment (Soutsos and Domone, 2018). Categories 1 and 2, when used in mixes, will absorb some of the mix water, whereas Category 4 aggregate will increase the amount of water in the mix. The absorption of the aggregate, therefore, is related to the aggregate's porosity, and can be calculated using the weight of the sample:

$$Percent\ Absporption\ by\ Weight = \frac{w_2 - w_1}{w_1} \times 100 \qquad \text{Equation 4}$$

In Equation 4, w_1 is the weight of completely oven dried aggregate, and w_2 is the weight of the aggregate when it can be classified as Category 3. Most normal-weight aggregates have absorptions ranging from 1% to 3%. Increasing porosity leads to a decrease in strength (Soutsos and Domone, 2018), but both concrete's need for entrained air and the simultaneous need for strength must be balanced during mix design.

3.4. Concrete and Freeze-Thaw

As concrete is a complex and not completely homogeneous, it can be tempting to overlook the small air voids entrained throughout in favor of its other more active components, such as the amount of cement required or any admixtures present. However, these voids play an important role in how the material avoids cracking and subsequent deterioration, especially in the case of pavements, the majority of which must endure sometimes dramatic temperature changes over their lifespan.

The diffusion of moisture is an important factor to consider, especially in reference to entrained air void shape, size, and location. Water in entrained air pores can take one of four forms: capillary water, absorbed water, interlayer water, and chemically combined water. Capillary water is located in larger gel pores wider than 50 nm or in the capillary voids. This water is most important when considering freeze-thaw, as the water in entrapped air and capillary voids expands when frozen, which leads to internal stresses that can cause rupture within the concrete.

When capillary water freezes, it expands by about 9%; if there isn't enough space in the surrounding entrained air voids to allow for this, internal pressures within the concrete build. Applied stress on the concrete causes changes within the hcp's internal stresses and strain energy, which affects the hcp's thermodynamic equilibrium, causing moisture to move from smaller to larger air voids and concentrations of hcp's stress to rise (Soutsos and Domone, 2018).

Hcp is not the only part of the concrete susceptible to freeze-thaw damage – the aggregates themselves are also at risk. The durability of the concrete depends largely on the aggregate, so knowing the warning signs of aggregate damage (such as pop-outs) due to freeze-thaw is important to timely and early intervention. Limestone aggregates and other porous sandstones are some of the most vulnerable as they have high water absorption, but less absorptive aggregates are still at risk to this type of damage. Aggregates are subject to the same guidelines, as is hcp in terms of pore size. Pores between 4 and 5 μm in diameter are large enough for water to enter but not enough to allow the pressure, once built up, to dissipate. The size of the aggregate plays a role as well, as smaller aggregates have an average shorter distance from ice to a surrounding material that can relieve the pressure. Multiple freezing and thawing cycles causes the "progressive and cumulative damage in the form of cracking and spalling" (Soutsos and Domone, 2018). Initially this is on the surface of the concrete, but as external moisture enters these cracks into the subsurface and endures more freeze-thaw cycles, it worsens the condition of the concrete.

The water in the smaller gel pores is absorbed into the surrounding calcium silica hydrate, and as a result has a much lower freezing point than its surrounding material, around -78°C, which is a highly unusual for concrete pavement to reach (Soutsos and Domone, 2018). After freezing, the water in the gel pores tends to move toward and combine with the capillary water, increasing the pressure of the ice inside the concrete and worsening existing freeze-thaw issues. The water inside of the pores is a mix of calcium hydroxide and other alkali materials, sometimes including chlorides from either de-icing agents or ocean water, depending on the location and climate (Soutsos and Domone, 2018). The water itself separates from the salts when it freezes, leading to salt concentrations, which in turn increases the water migration toward the capillary water.

How strong the internal pressure grows is dependent on capillary porosity, saturation level of the concrete, and how much relief the surrounding entrained air voids or materials can give (Soutsos and Domone, 2018). The amount of relief from internal pressure that can be occur depends on the surrounding material's permeability and distance to the ice, as well as how quickly the ice forms. In a saturated cement paste, the internal pressure can be relieved if the ice forms within 0.1 mm of a surrounding material (the surrounding aggregate, air voids, hcp, etc.). Air-entraining agents can be used in concrete that foresee use in constant freeze-thaw cycle areas, as they entrain air in small bubbles spaced at about 0.2 mm, which helps alleviate this problem.

An alternative way to lessen freeze-thaw effects is by lowering the w/c ratio and ensuring proper curing, so that hydration is as complete as possible (Soutsos and Domone, 2018). This should also result in minimal bleeding, another result of over-vibration.

The US Bureau of Reclamation in 1955 studied the resistance to frost of a moist cured concrete with and without air entrainment agents (Figure 2), and found that presence of properly entrained air in concrete leads to increased durability of the concrete in terms of withstanding freeze-thaw cycles.

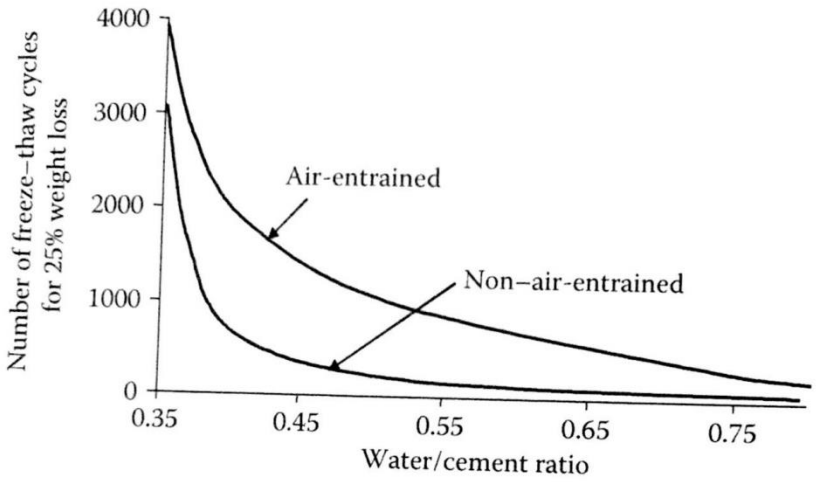

Figure 2: Effect of Air-Entrainment and w/c Ratio on Moist-Cured Concrete's Frost Resistance (US Bureau of Reclamation, 1955)

If the entrained air voids are evenly spaced, and of similar size, the water distributes more evenly than it would if they were unevenly sized and spaced erratically, as is the case with entrapped air voids. Round pores evenly spaced throughout the concrete help ensure that when the concrete's water trapped in the larger capillaries and entrapped air voids

expand, they do so into the evenly distributed entrained air voids, rather than breaking the surrounding concrete.

Because ice has 9% more volume than water, when pores are critically saturated, the expanding ice causes pressure high enough to permanently damage the surrounding concrete. Air voids therefore provide necessary spaces into which the water may be pushed, relieving the pressure and limiting concrete deterioration and cracking. According to Ozyildirim (2004), air voids must be small, closely spaced, and uniformly distributed to ensure adequate strength and resistance to freeze-thaw cycles. Irregularly shaped air voids, such as oblong or bottlenecking ones are not preferred, as the resulting pressure when the water expands causes pressure at the bottleneck point, which can still damage the surrounding concrete. The majority of air voids are not perfect at casting, but adequate vibration can help ensure that they become as evenly spaced and sized as is possible during construction.

In pavement specifically, vibration is necessary because most pavement has low slump and is stiff when poured. However, too much vibration can cause segregation, bleeding, or loss of entrained air. This can be caused by simply operating a vibrator in one space for too long, or vibrating at too high a rate. On the other hand, vibrating too little can cause an uneven distribution of coarse aggregate particulate or large entrapped air voids and lead to poor consolidation. This can be caused by not allowing vibrators enough time in one space, or by vibrating at too low a rate.

3.5. Maintenance costs and roadway costs caused by potholes

Improperly consolidated entrapped air voids in concrete roadways can cause potholes and other road issues that result in the pavement needing to be repaired and replaced. This is costly and inconvenient for both Departments of Transportation and commuters. The average cost to repair automobile damage caused by a pothole per incident is $306. A 2016 study by the American Automobile Association (AAA) revealed that over five years, potholes cost US drivers $15 billion and affected around 16 million drivers across the country. Damages caused by potholes include tire punctures, bent wheels, and suspension damage, which can require expensive repairs or replacements. Blown tires can create dangerous driving conditions and worsen traffic congestion. AAA also responds to over 4 million calls for flat tire assistance, many caused by potholes (Insurancejournal, 2016). In the span of five days in 2019, the City of Omaha alone paid around $260,000 to repair 7,445 potholes (Omaha World Herald, 2019). The early detection of consolidation caused voids that could form potholes in the future is therefore an important and relevant topic worth investigation.

3.6. Early detection

Detecting air voids soon after pouring has been a challenge, because high moisture content of the material being scanned increases absorption of the electromagnetic waves and more scattering. Maierhofer (2003) asserts that it is almost impossible to investigate fresh and setting concrete with GPR. However, early detection before the 24-hour setting window, if possible, has quality control advantages. Early detection of honeycombing

caused by poor consolidation allows DOTs to identify the source of the problem and make repairs before it spreads to larger pavement sections.

3.7. Case studies

As GPR is useful for distinguishing different material layers and their material properties, such as dielectric constants and conductivity for electromagnetic waves (Tosti et al., 2018), GPR's use in the pavement evaluation, specifically in rebar cover depth estimation and void detection, has been in use since the 1980s (Al-Qadi, 2003; Fernandes and Pais). This can be attributed to its relative ease in use and mobility – furthermore, Morcous and Erdogmus (2010) found that the presence of metal objects employed under concrete layers is necessary for reliable measurements of pavement thickness, in addition to improving reflectivity of EM waves at the bottom surfaces. GPR has also been used in pavement layer thickness determination, soil structure change location, concrete bridge deck deterioration evaluation, and void detection under jointed concrete slabs (Maser, 1996; Maierhofer, 2003; Morcous, 2010; Tosti et al., 2018).

In their study on an experimental section of highway located in Missouri, Li et al. (2016) compared GPR and stress-wave techniques to monitor possible air voids in the concrete pavement's interface between the concrete layer and granular base. Different types of NDE methods were used to understand the differences between each type of evaluation in detecting large air voids in the subsurface of the concrete pavement. Specimens were cored at multiple locations to confirm each method's accuracy and reliability. In particular, this study's findings showed that GPR was accurate in approximating the

concrete pavement thickness and locating air voids sized between 0.25” and 0.5” (0.64 cm and 1.27 cm) between the two layers, although the presence of highly conductive material, concrete consolidation, moisture content, and void size affected the GPR result’s reliability. As the moisture content of a material significantly affects its dielectric constant, the dielectric constant of a material with high moisture content is significantly higher than that of the same material in a dry state. During the experimental segment of Li et al.’s research, the GPR data was acquired by a single cart-mounted high frequency (1.5GHz) ground coupled antenna. Using an assumed dielectric constant for dry concrete to convert reflection times to depths, the raw GPR data was processed. The concrete’s obtained average dynamic modulus was found to be more reliable and consistent than the calculated average dynamic modulus based on the full wavelength range, because the under-layer material and identified air voids’ influence at the interface were excluded. At the base of the concrete layer, relatively low dynamic modulus values were identified – an indication of potential air voids between the concrete and granular base layers. Reversing the polarity of GPR signals at the concrete and granular base layer interface allowed Li et al. to observe the present air voids more clearly during post-processing, as the velocity of the electromagnetic waves increased when they propagated into an air void and the resulting parabolas contrasted strongly with the surrounding material in scans. After successfully measuring air voids at the base of cored specimens Li et al. conclude that GPR proves to be an accurate method to estimate the thickness of concrete pavement. Air voids at the concrete-granular base interface were characterized by GPR signals’ reversed polarity and were confirmed by cores of specimens nearby.

In a blind test of underground air void detection done by Hong Kong Polytechnic University (UPoly), Lai et al. implanted eight spherical voids, varying from 0.62 meters to 1.0 meter in diameter, in a test site. Cover ranged from 0.361 meters to 1.596 meters in depth, and UPVC and DI pipes, to imitate realistic conditions of buried utility lines nearby, were also buried in the vicinity of the voids. This experiment was derived from pipe leakage causing air and water filled voids from city water distribution networks. Researchers wanted to test if service providers could distinguish between the implanted voids and imitation utility lines. Six service providers scanned the test site with GPR to map out the implanted void locations. Although they could not replicate the blind void mapping done by the UPoly team, this experiment highlighted how teams could gain varying results while scanning the same location with GPR, and the conclusions of this experiment suggested future experiments on how NDE technology can be commercialized to solve common engineering problems. For example, GPR with a lower operating frequency, such as 10 to100 MHz and a resolution in tens of meters would be useful for deep foundation assessment. GPR with a mid-range operating frequency varying from 100 to 1000 MHz could be used to distinguish between tunnel liners, road pavements, and utilities on a scale of meters. A high resolution system, with a frequency ranging between 1000 and 5000 MHz, would be useful in scanning tunnel liners and other assessments on a centimeter scale (Lai et al., 2017 (1)).

GPR can be ground coupled or air coupled - both option has its advantages. Ground-coupled GPR operates at high frequencies to assess material at a depth of 10 to 40 cm while air-coupled GPR operates at lower frequencies and shallowly penetrates material. Ground-coupled GPR does a better job of penetrating the surface and detecting small subsurface features whereas air-coupled GPR systems are better used for assessing long stretches of the upper section of pavement structures, and can scan while traveling at highway speeds. This lower spatial resolution makes air-coupled GPR scanners unsuitable for detecting small delaminations such as cracks or voids. (Fernandes and Pais, 2017).

Chapter 4. Methodology

Testing was first conducted in the structures laboratory of the University of Nebraska-Lincoln (UNL) to control testing conditions. Two slabs were poured and artificial air voids were implanted for GPR detection. After completing lab casting and testing, a six-week old roadway construction site was field tested using a modified GPR detection technique previously developed and tested in the laboratory. A GSSI 1.6 GHz GPR handheld cart system was used for all scanning. The gain settings during data processing were adjusted depending on the amount of time elapsed after casting so that scanning would generate the best possible void visibility. A third slab was then poured to track the dielectric constant over the first 23.5 hours of the slab's existence.

4.1. Laboratory Testing Methodology

Slabs 1 and 2 were cast and tested in UNL's structures laboratory. NDOT's 47B Concrete Pavement Mix with 2" (5.08 cm) slump was used in both specimens. Both slabs were adequately consolidated using internal vibration, and their surfaces finished and covered with a plastic sheet for curing. No curing compound was used on Slab 1.

Both slabs rested on or were slightly raised above concrete lab floors while they were scanned with GPR. Steel reinforcement was present at the ends of both slabs, which allowed calibration of the slab's depth in scan outputs. The contrast in dielectric between the concrete and steel present allowed ease in differentiating between the specimen and the floor in scan outputs. As previously noted, the depth of the reinforcement was known

and used to confirm the depth of the slab on the scans during processing. Confirming the correct depth of the specimen, which allowed distinction between the specimen slab and the floor slab in data collection and analysis, was done by calibrating the depth of the slab using the reinforcement depths and TWT. This allowed an accurate depth detection of implanted artificial voids in specimens. Cores were then taken to visually verify results. Slab 1 and 2's information overview can be seen in Table 2.

Table 2: Laboratory Specimen Information Overview

Slab Number	Slab 1	Slab 3
Date Poured	September 29, 2018	March 28, 2019
Dimensions	44" x 40" x 8" (1.12 m x 1.02 m x 20.32 cm)	72" x 72" x 9" (1.83 m x 1.83 m x 22.86 cm)
Artificial Void Dimension Range	0.75" – 2" (0.91 cm – 5.08 cm) (smallest to largest dimension)	1" – 5.75" (2.54 cm – 14.6 cm) (smallest to largest dimension)
Artificial Void Depth Range	1" – 2" (2.54 cm – 5.08 cm) (smallest to largest dimension)	1" – 4" (2.54 cm – 10.16 cm) (smallest to largest dimension)

After consulting with NDOT personnnel, the detection of air voids with dimensions greater than 1.25" (3.16 cm) were prioritized. Based on the experience of NDOT engineers, voids of this size and larger can have detrimental effects on pavement durability, whereas smaller voids do not have a significant effect on the concrete's quality and strength.

4.1.1. Slab 1 Methodology

Slab 1 measuring 44” x 40” x 8” (1.12 m x 1.02 m x 20.32 cm) was cast and investigated on September 29, 2018. This specimen was reinforced with two #4 (13 mm) bars placed 1.5” (3.81 cm) from the slab edge in both directions at an average depth of 6 NDOT 47B Concrete Pavement Mix with 2” (5.08 cm) slump.25” (15.87 cm). This slab used, and its mix design components can be seen in Table 3.

Table 3: Slab 1 - Mix Design

NDOT 47B Concrete Mix Design	
Material	Weight
Total Load Weight	5518 lb (2503 kg)
1PF Cement	980 lb (445 kg)
47B Gravel (Limestone)	3040 lb (1379 kg)
47B Rock	1300 lb (590 kg)
LRWR (Pozz 322N)	29 oz (822 g)
Water	34 gl (129 L)
Air entrainment agent (MB AE 200)	8 oz (227 g)
Water/Cement Ratio	0.29
Min Required Strength	500 psf (168 kPa)

Insulation spray foam with a similar density to naturally-occuring air voids was used to create the artificial voids (Figure 3).

Figure 3: Slab 1 – Small Artificial Air Void

After the slab was visually divided into four quadrants (Figure 4), the artificial voids were implanted in each quadrant, grouped by their size and depth (Table 4).

Table 4: Slab 1 - Void Dimensions

Void Size Category	Void Number	Dimensions	Depth
Large Voids	4	2” x 1.75” (5.08 cm x 4.45 cm)	2” (5.08 cm)
	5	2” x 1.5” (5.08 cm x 3.81 cm)	2” (5.08 cm)
	6	1.5” x 1.5” (3.81 cm x 3.81 cm)	2” (5.08 cm)
Small Voids	7	1.75” x 0.75” (4.45 cm x 0.91 cm)	1” (2.54 cm)
	8	1.25” x 1.25” (3.18 cm x 3.18 cm)	1” (2.54 cm)
	9	0.75” x 1.5” (0.91 cm x 3.81 cm)	1” (2.54 cm)

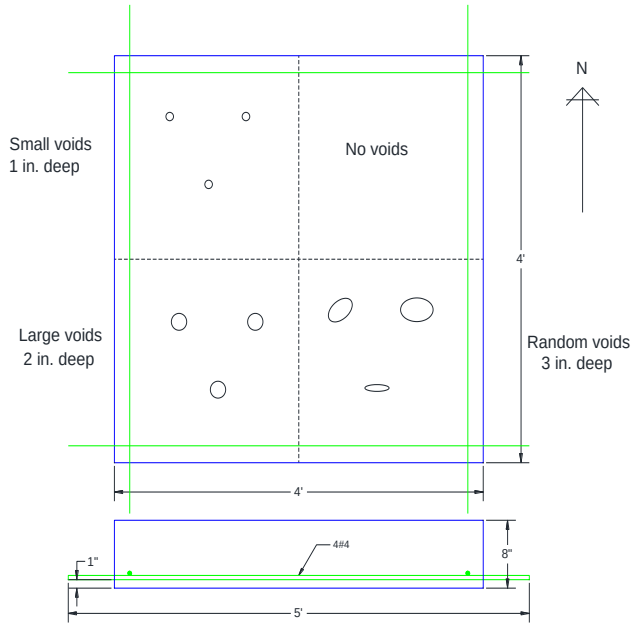

Figure 4: Slab 1 - Void Types and Depths with Reinforcement Locations

The large and small spray foam voids were sprayed outside the slab and allowed to stiffen and harden into defined shapes. The “Random Voids” shown in the bottom-right corner of Figure 5 were created by directly injecting the spray foam into the concrete, causing the size and shape of the artificial voids to be unknown. One quadrant functioned as a control quadrant (top right in Figure 5) with no artificial voids. The concrete was adequately consolidated using internal vibration, and the surface was finished and covered with a plastic sheet for curing. No curing compound was used on Slab 1.

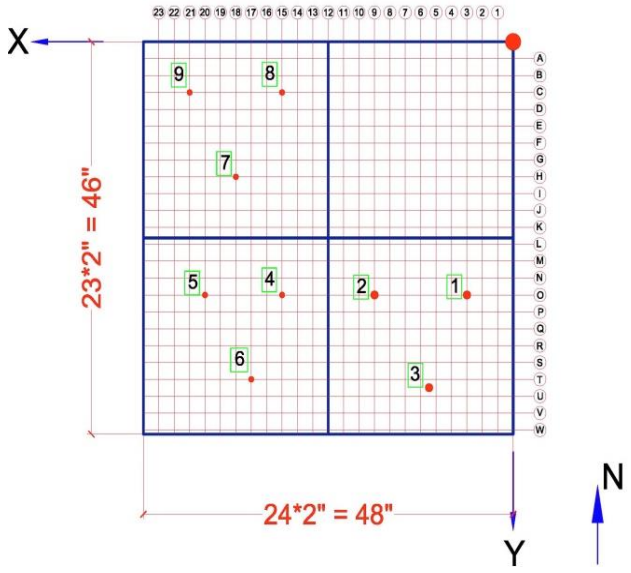

Figure 5: Slab 1 - Core Numbers and GPR Scanning Gridlines

Slab 1 was scanned at 5 and 24 hours, as well as 2, 4, and 9 days after pouring. GPR scan grid lines were initially at 4" (10.16 cm) o.c., and were stenciled with chalk directly onto the top of Slab 1. In later stages, a plastic sheet with gridlines 2" (5.08 cm) o.c. were traced out and used for ease of use and scanning repeatability.

4.1.2. Slab 2 Methodology

Slab 2 was cast in UNL's structures lab on March 28, 2019, measuring 72" x 72" x 9" (1.83 m x 1.83 m x 22.86 cm), using NDOT 47B concrete. A SmartRock Temperature Sensor was embedded in the slab's center to monitor its internal temperature change. The slab had a low temperature of 64.8°F and a max temperature of 95.0°F. The slab's internal change in temperature can be seen in Figure 6, and is specific to NDOT 47B concrete. This change in internal temperature can be used as an example of the range this specific type of concrete experiences.

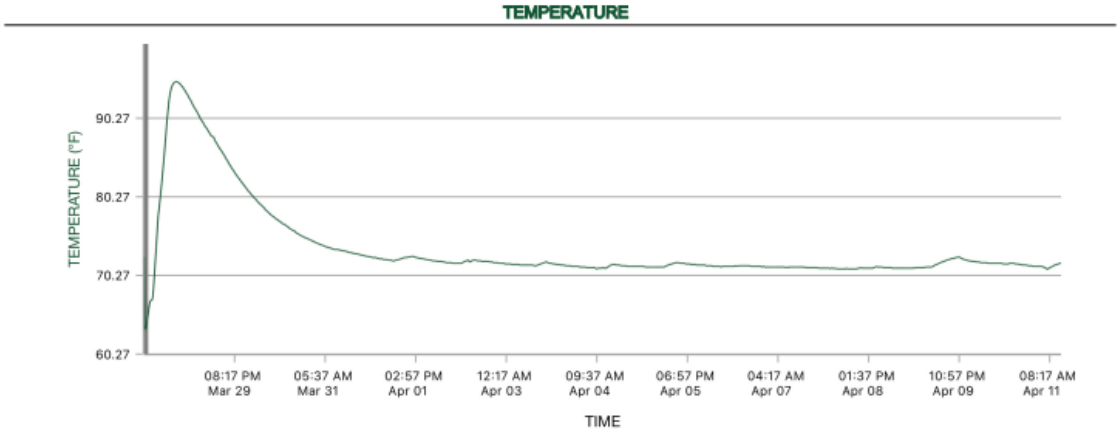

Figure 6: Slab Change in Temperature

The slab was again divided into four quadrants with different sized artificial voids in each. Two types of artificial voids were created and implanted in the slab at depths of 1”-4” (2.54 cm-10.16 cm). Type One voids were created by using insulation spray foam – the same foam successfully used in Slab 1 - were again sprayed into shapes and allowed to harden outside of the slab (Figure 7).

Figure 7: Slab 2 – Artificial Air Voids

Type Two voids were created by injecting compressed air directly into the slab to form voids of unknown size and depth. The voids' locations were measured from the southwest corner of the slab (the "origin") and are recorded as shown in Table 5.

Table 5: Slab 2 - Void Dimensions and Locations

Core No.	Void Size (Quadrant)	Void Dimension	Location from Origin
1	Type One: Small (NW Corner)	2" x 1.5" (5.08 cm x 3.81 cm)	12", 59" (0.3 m, 1.5 m)
2		2" x 1.75" (5.08 cm x 4.45 cm)	14", 50" (0.4 m, 1.3 m)
3		1.5" x 1.5" (3.81 cm x 3.81 cm)	23", 60" (0.6 m, 1.5 m)
4		2" x 1.5" (5.08 cm x 3.81 cm)	23", 48" (0.6 m, 1.2 m)
5	Type One: Large (SW Corner)	2" x 2" (5.08 cm x 5.08 cm)	11", 9" (0.3 m, 0.2 m)
6		2.5" x 2" (6.35 cm x 5.08 cm)	26", 10" (0.7 m, 0.3 m)
7		2.5" x 1.75" (6.35 cm x 4.45 cm)	13", 24" (0.3 m, 0.6 m)
8		4" x 1.5" (10.16 cm x 3.81 cm)	26", 26" (0.7 m, 0.7 m)
9	Type One: Long (SE Corner)	3.75" x 1" (9.53 cm x 2.54 cm)	64", 12" (1.6 m, 0.3 m)
10		5" x 1" (12.7 cm x 2.54 cm)	51", 13" (1.3 m, 0.4 m)
11		5.75" x 1" (14.6 cm x 2.54 cm)	60", 23" (1.5 m, 0.6 m)
12		6.5" x 1" (16.51 cm x 2.54 cm)	46", 26" (1.2 m, 0.7 m)
13-16	Type Two: Compressed Air (NE Corner)	Random	Unknown

NDOT's Right Pointe White Water Wax concrete curing compound was sprayed on the top surface to follow typical field processes. NDOT routinely sprays this particular curing

compound right after concrete placement. When GPR is used on wet curing compound, the wheels of the handheld GPR device removes lines of compound, likely reducing its effectiveness (Figure 8).

Figure 8: Slab 2 – Image after Scanning the Slab with GPR at 3 and 4 Hours on Curing Compound

GPR scanning was conducted on a 2” x 2” (5.08 cm x 5.08 cm) o.c. grid on the western half of the slab, three hours and four hours after pouring, and on the entire slab 24 hours after pouring. Due to lab space restrictions, the slab was moved outside after GPR scanning, and coring was completed outdoors. Three verification cores were taken at void locations 8, 12, and 13 to test for the detection of large voids, oblong voids, and compressed air, respectively.

4.1.3. Slab 3 Methodology

Slab 3 was cast on August 4th, 2020, measuring 36” x 48” x 4” (0.91 m x 1.22 m x 10.16 cm). Quickcrete High Strength concrete mix with a 7” (17.78 cm) slump was hand mixed

and poured into the prepared formwork (Figure 9). Due to the high slump, the specimen did not require vibration for adequate consolidation. A 23” x 23” (58.4 cm x 58.4 cm) steel plate with a 4” (10.16 cm) diameter hole in the center, rather than reinforcement, was used for scanning calibration purposes and was centered at the bottom of the formwork (Figure 10).

Figure 9: Slab 3 - Hand-pouring concrete

Figure 10: Slab 3 – Steel plate used for calibration in formwork

Figure 11: Slab 3 - Finished Slab

The slab was leveled and finished by hand (Figure 11). No artificial voids were implanted in this slab, as its purpose was for tracking the change in dielectric constant over the specimen's first 24 hours using GPR. The specimen was scanned hourly at 2" (5.08 cm) o.c. using the plastic sheet with the scanning stencil marked out

4.2. Field Testing Methodology

After seeing the effects of scanning on a wet curing compound, a modified grid for field scanning was made. The grid was a 4’ x 4’ x 0.75” (1.22 m x 1.22 m x 1.9 cm) sheet of plywood with four 1.25” (3.18 cm) long screws screwed into each corner. A 4” x 4” (10.16 cm x 10.16 cm) grid was marked on the plywood sheet for ease of use. This created a scanning grid elevated 0.5” (1.25 cm) above the surface of the concrete, rather than lying directly on top of it. Using this grid, scanned sections of concrete could stay unmarked by scanning lines when the curing compound was not completely dry.

A six-week old section of pavement on Highway 30 west of North Bend, NE was scanned in three different areas on October 25th, 2019. This scanning occurred after the laboratory testing of Slab 1 and Slab 2 had concluded, and used the modified scanning procedure with the elevated plywood sheet grid. Scans were not done on a 2” x 2” (5.08 cm x 5.08 cm) grid, as it was faster to scan at 4” x 4” (10.16 cm x 10.16 cm) o.c. and time was limited.

Figure 12: Field Experiment - GPR Scanning

GPR scans did not pick up any significant voids in the top four inches of pavement. Coring at three scanning locations yielded no voids of a concernable size, as is shown in Figure 13.

Figure 13: Field Experiment - Three Cores

Chapter 5. Results

5.1. Laboratory Work Results

Three slabs were cast and tested in UNL's structures laboratory. NDOT 47B Concrete Pavement Mix with 2" (5.08 cm) slump was used in the first two specimens, and Quickcrete High Strength concrete mix with a 7" (17.78 cm) slump was used for the third specimen. All slabs rested on or were slightly raised above concrete lab floors while they were scanned with a GSSI 1.6 GHz GPR handheld cart system. The depth of steel plating or reinforcement in all slabs was known and used for calibration purposes and to confirm the depth of the slab in scans during processing. The change in dielectric between the concrete and steel assisted in differentiating between the specimen and the concrete floor they rested on in GPR scan outputs. Confirming the correct depth of specimen allowed an accurate depth detection of implanted artificial voids in Slabs 1 and 2. Cores were taken to visually verify GPR detected results, if artificial voids had been implanted. Gain settings during data processing were adjusted depending on the amount of time that had passed after casting to ensure optimal void visibility in scans. After completing lab casting and testing, a six-week old roadway construction site was field tested using a modified GPR detection technique previously developed and tested in the laboratory. This research has both tracked the change in dielectric constant over the first 24 hours of a specimen, and found that it is possible to scan and detect voids earlier than the 24-hour mark, and as early as three hours after pouring. An overview of the slabs with voids implanted can be found in Table 6.

Table 6: Slab 1 and 2 - Specimen Information Overview

Slab Number	Slab 1	Slab 3
Date Poured	September 29, 2018	March 28, 2019
Dimensions	48” x 46.5” x 8” (1.12 m x 1.02 m x 20.31 cm)	72” x 72” x 9” (1.83 m x 1.83 m x 22.86 cm)
Artificial Void Dimension Range	0.75” – 2” (0.91 cm – 5.08 cm) (smallest to largest dimension)	1” – 5.75” (2.54 cm – 14.6 cm) (smallest to largest dimension)
Artificial Void Depth Range	1” – 2” (2.54 cm – 5.08 cm) (smallest to largest dimension)	1” – 4” (2.54 cm – 10.16 cm) (smallest to largest dimension)

After consulting with NDOT personnel, the detection of air voids with dimensions greater than 1.25” (3.16 cm) were prioritized. Based on the experience of NDOT engineers, voids of this size and larger can have detrimental effects on pavement durability, whereas smaller voids do not have a significant effect on pavement’s quality and strength.

5.1.1. Slab 1 Results

Slab 1 was scanned with GPR at 5 and 24 hours, as well as 2, 4 and 9 days after pouring. The GPR line scans were initilaly done at 4” (10.16 cm) o.c., and later at 2” (5.08 cm) o.c. in both directions. Both the large pre-sprayed voids and “random” soft voids were clearly detected at 5 hours after pouring, while the small voids’ signals were vague at that point in time. After nine days, Slab 1 was cored in 10 places centered on the void locations detected by GPR. In addition to the nine cores taken in each of the three quadrants with implanted artificial voids, Core 10 was taken from the control quadrant.

GPR signals picked up very fine signals throughout this cross section, even though there were no artificial voids located in that quadrant.

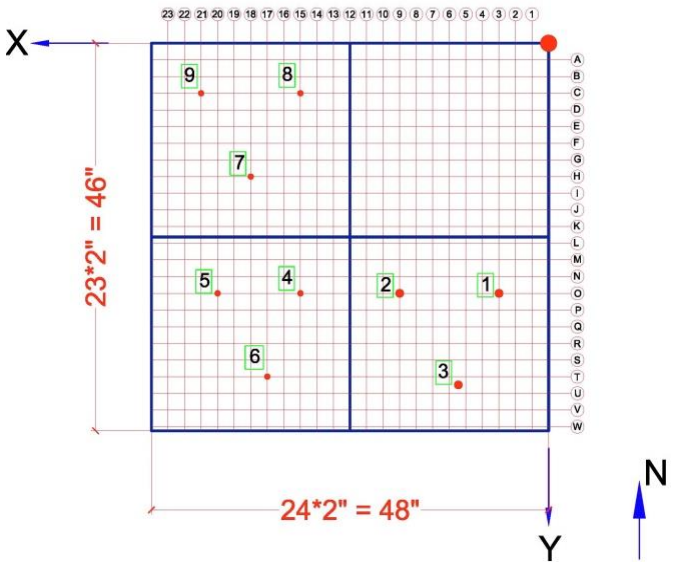

Figure 14: Slab 1 - Core Numbers and GPR grid lines

The dimensions and embedment depths of the artificial voids for Slab 1 are shown in Table 7, and their locations can be seen in Figure 14. The smallest known dimension of the artificial voids was 0.75”, and the largest was 2”. The dimensions and embedment depth of the “random” soft sprayed voids were unknown.

Table 7: Slab 1 - Void Dimensions and Embedment Depths

Void Size Category	Void Number	Dimensions	Depth
Random	1 – 3	Unknown	Unknown
Large Pre-Sprayed and Hardened Foam Voids	4	2” x 1.75” (5.08cm x 4.45cm)	2” (5.08cm)
	5	2” x 1.5” (5.08cm x 3.81cm)	2” (5.08cm)
	6	1.5” x 1.5” (3.81cm x 3.81cm)	2” (5.08cm)
Small Pre-Sprayed and Hardened Foam Voids	7	1.75” x 0.75” (4.45cm x 0.91cm)	1” (2.54cm)
	8	1.25” x 1.25” (3.18cm x 3.18cm)	1” (2.54cm)
	9	0.75” x 1.5” (0.91cm x 3.81cm)	1” (2.54cm)

After measuring void size and embedment depth, the slab was scanned with GPR for the purpose of early void detection. The scans of the Southeast quadrant from five hours after pouring are shown in Figure 15, with the locations of the detected voids shown on the plan view of the slab in Figure 16. The blue arrow on Figure 16 shows the direction of the scans, beginning on the line closest to the center of the slab and moving toward the perimeter at 4” o.c. The detection of the “Random” soft spray foam Voids 1 and 3 are circled in Figure 15 for ease of readability.

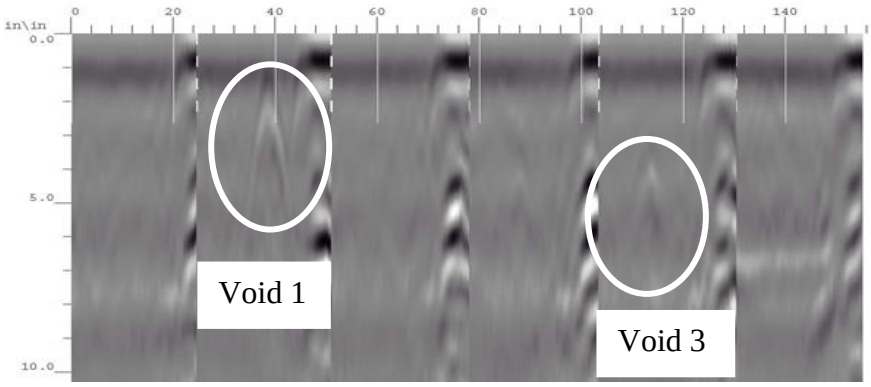

Figure 15: Slab 1 – Five-Hour Scan of Southeast Corner

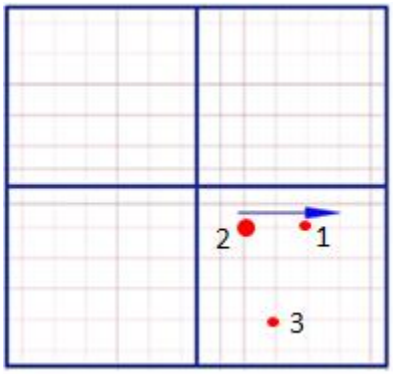

Figure 16: Slab 1 – Illustration of the Five Hour Scan of Southeast Corner with Void Locations and Scan Direction

After the scans were taken, different gains (based on the time elasped after pouring) and color schemes were applied in an effort to improve readability. Examples of signals with different strengths are shown in Figure 17. The scans shown (three in greyscale and three in brown) are grouped into three categories with one grayscale and one brown each. The two leftmost scans show a stong signal before (grayscale) and after (brown) postprocessing. The two middle scans and rightmost scans show a medium and vague signal before (grayscale) and after (brown) postprocessing, respectively. Detected voids are circled for ease in readability. The gain was changed from 0 to 12 in all the scans in Figure 17 for improved contrast, and the default color setting (grayscale) was changed to brown for an example of a potential color adjustment in postprocessing.

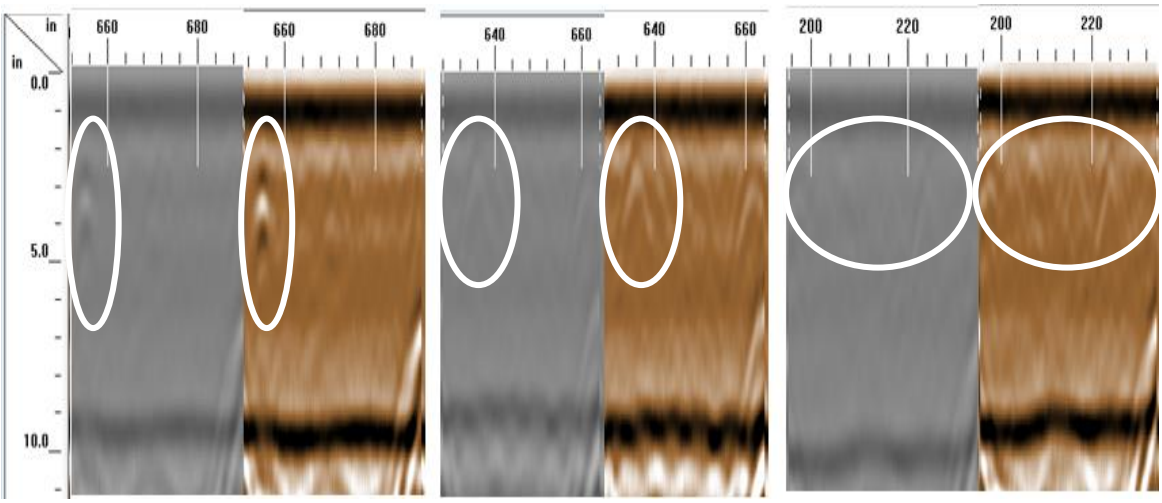

Figure 17: From Left to Right: Clear, Medium, and Vague Signal Examples Using Default Setting and Post Processing

After all scanning was completed, core samples were extracted at locations where strong signals for anomolies were detected (Figure 17 shows examples of signals of varying strengths). Nine days after casting, the specimen was cored in 10 places centered on the void locations detected with GPR. The results of the GPR scans and observations on the cores are shown in Table 8. At least one of each type of void was successfully located in the cores. In Core 10, even though there were no artificial voids present, GPR signals picked up very fine air signals throughout the cross section. As expected, there were fine air bubbles of negligible size present that formed naturally during consolidation.

Table 8: Slab 1 - Void Coring Results

Core Number	Embedded Voids	GPR Signal clarity	Coring Results	Notes
1	Random Free Spray	Clear	Visible artificial void	
2		Clear and Vague	No artificial void at center	Void located half a core diameter off Other, smaller voids present at location of vague signal
3		Clear	Visible artificial void	
4	Large Pre-Sprayed and Hardened Foams	Vague	No artificial void	Void located half a core diameter off Other, smaller voids also present
5		Clear	Visible artificial void	Fine voids also present
6		Clear	No artificial void	No void present when coring
7	Small Pre-Sprayed and Hardened Foam	Vague	No artificial void	No void present when coring Fine voids present
8		Clear	No artificial void	No void present when coring Questionable location
9		Clear	Visible artificial void	
10	No Voids	Moderate	No artificial void	Fine voids present

This laboratory experiment helped to determine the lower size limit of air voids that could be easily detected in the top four inches of pavement, which was 1.25” (3.16 cm).

5.1.2. Slab 2 Results

Slab 2 was embedded with two types of artificial voids:small, long, and oblong spray foam voids, and injected pressurized air. Figure 18 illustrates the slab with scanning grid and void locations, as well as the location of the linear scan, results of which are presented in Figure 19 through Figure 21.

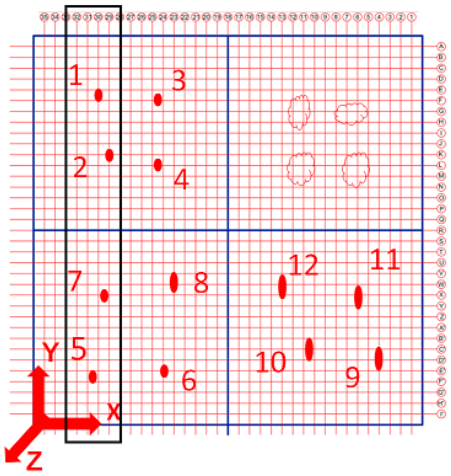

Figure 18: Slab 2 – North-South Linear Scan Location (denoted by rectangle) at 3, 4, and 24 Hours

Corresponding scans are presented in Figure 19, Figure 20, and Figure 21, respectively.

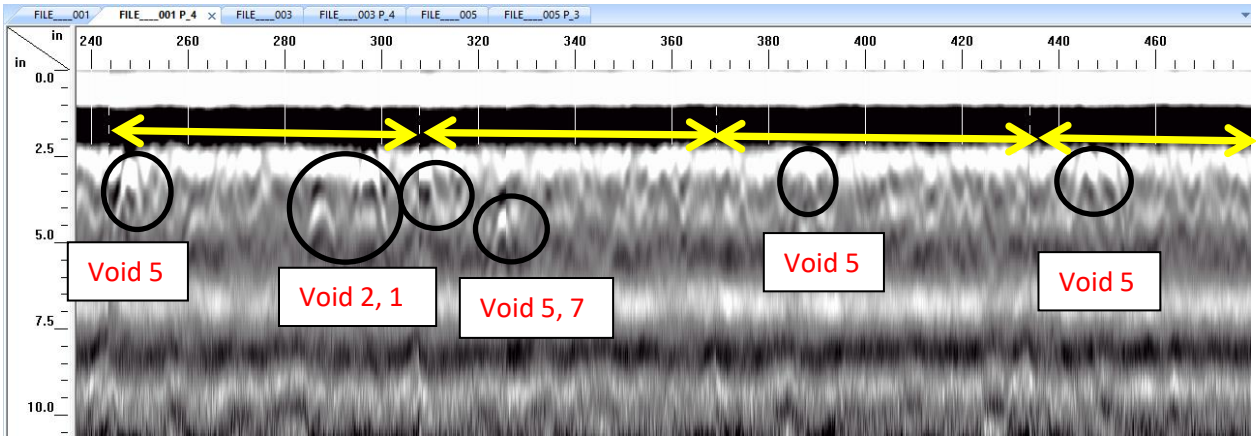

Figure 19: Slab 2 - North-South Scan at 3 Hours

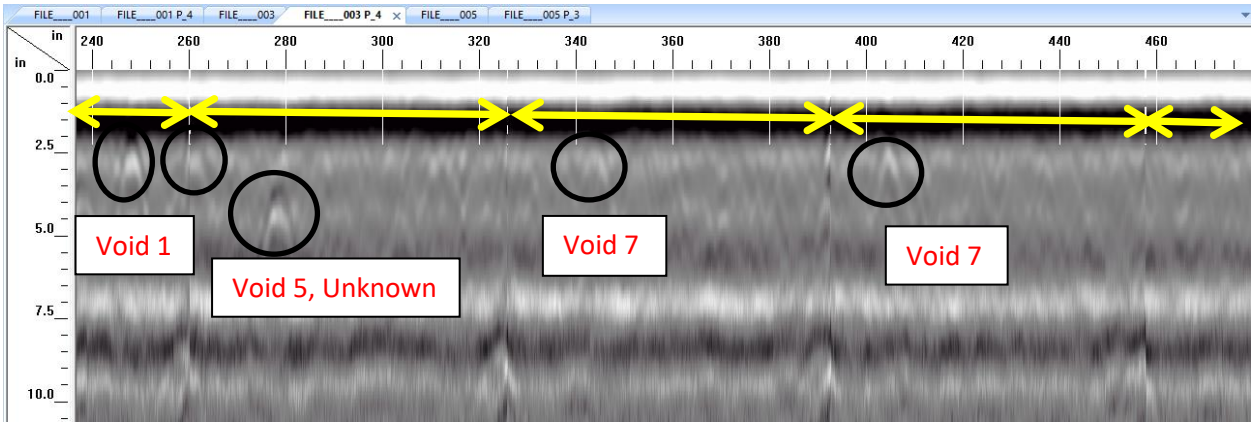

Figure 20: Slab 2 – North-South Scan at 4 Hours

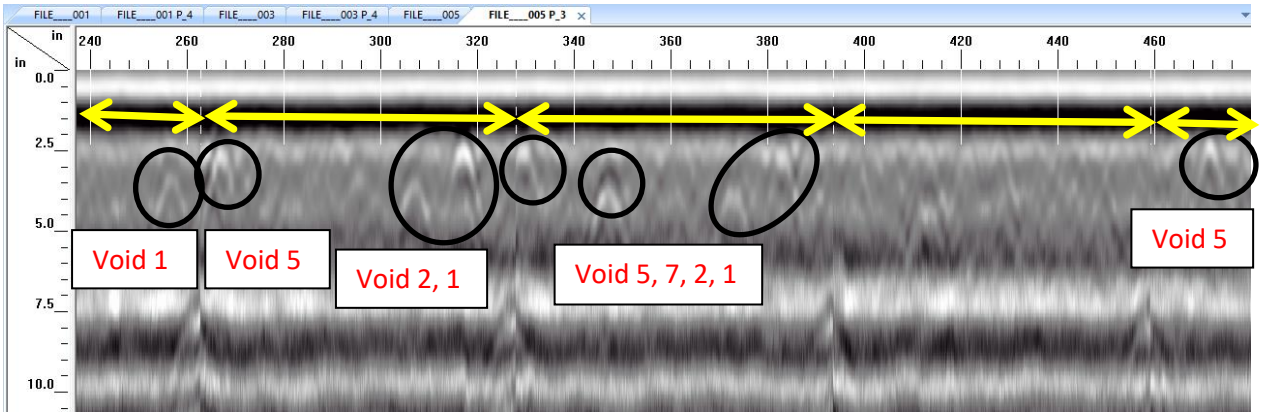

Figure 21: Slab 2 - North-South Scan at 24 Hours

Three verification cores were taken at void locations 8, 12, and 13 to test for the detection of large voids, oblong voids, and compressed air, respectively and are shown in Figure 22 through Figure 24. No cores were taken for small voids (1 – 4), since smaller sized voids, (1" x 1" (2.54 cm x 2.54 cm) in diameter), had been successfully detected and cored in previous testing. Core 8's GPR scans showed one of the weaker signals, whereas Core 12's GPR scan was one of the strongest signals. This can be explained by the surface area perpendiculat to the direction of the magnetic waves propagating into the specimen. Because GPR performance, like all radars, is aspect dependent, it is naturally easier to

detect the oblong voids parallel to the surface (Figure 23) in comparison to a smaller void (Figure 22). The GPR signals for the compressed air area were vague, but a core was taken to examine the effects of the inserted compressed air. It appeared that the compressed air was dispersed into fine bubbles as the concrete consolidated, which explained the vague signals (Figure 24).

Figure 22: Slab 2 - Core 8 (Large Void)

Figure 23: Slab 2 - Core 12 (Oblong Void)

Figure 24: Slab 2 - Core 13 (Compressed Air)

Table 9 shows the average percent error and average inches and centimeters off between the physical locations (measured as the anomalies were inserted into the wet concrete)and the GPR detected void locations for Slab 2. It is important to note that the average percent error and average inches off for the 3 and 4 hour scans did not take into account voids 9 – 12, as only the western half of the slab was scanned at 3 and 4 hours. The 24 hour scan results shown in Table 9 include voids 9 – 12.

Table 9: Slab 2 - Hourly Comparison of Average Percent Error

Coordinate Direction	**X**		**Y**		**Z**	
Time Scanned	3 Hours	24 Hours	3 Hours	24 Hours	3 Hours	24 Hours
Avg Percent Error (%)	-2.9%	-2.4%	-1.6%	1.6%	44.8%	26.4%
Avg Cm off	3.81 cm	3.18 cm	3.18 cm	1.91 cm	2.54 cm	1.78 cm
Avg Inches off	1.5”	1.25”	1.25	0.75”	1”	0.7”

Table 9 shows that the percent error is less than 3% for the x and y-directions on the coordinate system with the exception of the 4 hour-scan in the y-direction. Larger errors can be explained by the slight shift in the starting point of the scan each time, since the experiment included use of a removable stencil. This minor variation is also evident in the scans shown in Figure 19 through Figure 21. Therefore, if several readings are to be taken for repeatability and data validaton, it is important to ensure the start of the scan line is consistent. Marking the gridlines directly on the surface instead of using a stencil is advantageous in this respect, although it adds significant time to the process if several measurements are to be taken over a long pavement section.

A compromise solution involves placing physical marks on the surface for the starting lines in each direction and aligning the stencil over these lines at each reading, but this would only be possible after the curing compound is dry. Despite these errors, the average dimensional error (in “inches off”) between the GPR-based location and the assumed location is 1.5” (3.81 cm) or less, which is less than half of a 4” (10.16 cm)

coring cylinder's diameter. The z-direction (depth) scans seems to give the largest error in percentage; however, the error is not as high in terms of units of length. The additional error in depth measurement also relates to the fact that depth readings are the most affected by the changing dielectric constant as the concrete cures and a concrete test slab sitting on concrete lab floor makes it difficult to adequately determine the base of the test slab for dielectric constant calibration, even with the calibration relying on known reinforcement locations. However, the z-direction errors were not the major concern during testing, as it was more critical to locate these voids in a pavement section horizontally than vertically.

Table 10 compares the assumed location of the artificial void to its GPR based location for Cores 8 and 12 (Figure 22 and Figure 23). Since the cores were taken by centering the GPR detected locations, the center of each core corresponds to the GPR detected location. As can be seen, the error is between 0.5" and 1" (1.27 cm and 2.54 cm) for these cores.

Table 10: Slab 2 – Cores 8 and 12 Assumed vs. GPR Detected Location

Core Identifier	**Core 8**	**Core 12**
Assumed Location	4" (10.16 cm)	4" (10.16 cm)
GPR Detected Location	3.5" (8.89 cm)	3" (7.62 cm)
Location Error	0.5" (1.27 cm)	1" (2.54 cm)
Signal Strength	Weak	Strong

At least one of each void size was identifiable and detectable by GPR at 3 hours after casting, and although the voids were more easily detectable at 24 hours, the noise level of the 24 hour scans were significantly higher than the 3 and 4 hour scans. To process the GPR scans, the gain was changed, from 0 to 30 for three hour scans, from 0 to 20 for four hour scans and from 0 to 12 for 24 hour scans for ease in interpretation and void identification. Different available color schemes were tested and the default "grayscale" was used for optimal ease in reading, as was also the case with Slab 1.

5.1.3. Slab 3 Results

After hand-pouring, leveling, and finishing Slab 3, it was scanned hourly with the same handheld cart GPR system as Slab 1 and 2 to track the change in dielectric constant over its first 24 hours. Although it was planned to scan at hour 1, hour 2, etc. for ease in tracking, at hour 1, the surface of the slab was not solid enough to scan with the handheld cart or use the elevated plywood stencil on. Therefore, scanning began 90 minutes after casting to give the specimen more time to cure and was scanned at 1.5 hours, 2.5 hours, etc. until 23.5 hours had elapsed. The change in dielectric constant can be seen in Figure 25, along with Table 11.

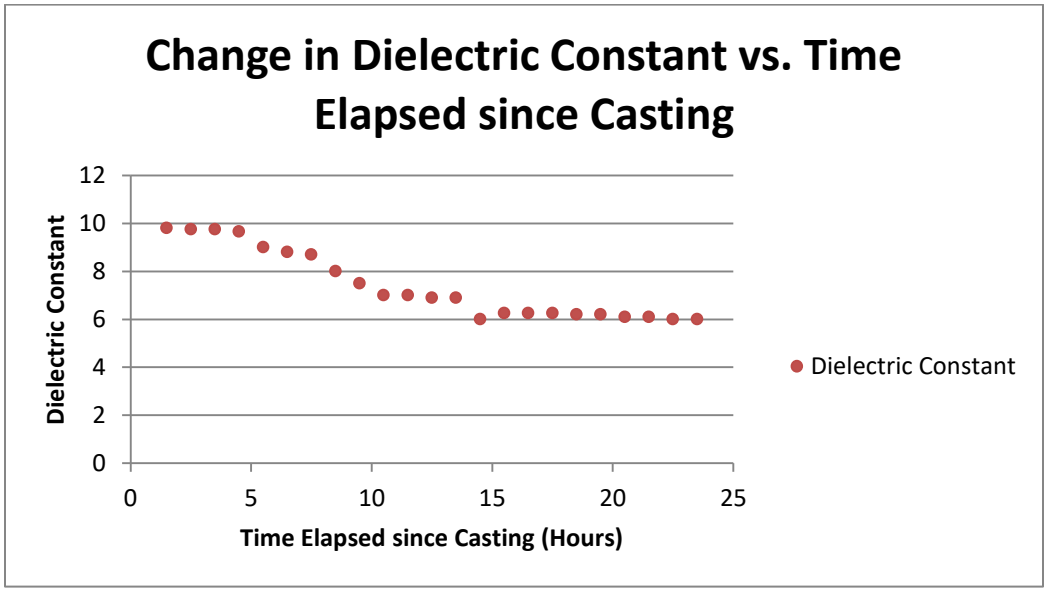

Figure 25: Slab 3 - Change in Dielectric Constant vs. Time Elapsed since Casting

Monitoring the change in dielectric constant over the first 24 hours of a specimen's lifetime yields data that can be used in future fieldwork. While this particular curve is unique to the specific type of concrete mix used in this experiment, similar curves can be constructed and used by DOTs for GPR scanning within the first 24 hours of pavement casting. Should DOTs test specimens with mix designs they frequently utilize in highway pavement, they will have a growing archive of data and curves to reference should they need to calibrate GPR equipment in the field and detect subsurface voids in fresh and setting concrete pavement quickly and accurately.

Table 11: Slab 3 - Hourly Change in Dielectric Constant

Hours Elapsed	Dielectric Constant
1.5	9.8
2.5	9.75
3.5	9.75
4.5	9.65
5.5	9
6.5	8.8
7.5	8.7
8.5	8
9.5	7.5
10.5	7
11.5	7
12.5	6.9
13.5	6.9
14.5	6
15.5	6.25
16.5	6.25
17.5	6.25
18.5	6.2
19.5	6.2
20.5	6.1
21.5	6.1
22.5	6
23.5	6

The scanning method utilizing the elevated plywood stencil was initially attempted. However, the screws on the corners and the plywood itself repeatedly sunk into the slab's surface during the first 4.5 hours after casting, which destabilized the scanning surface and caused cosmetic damage. As this was most likely a result of the mix's high slump, the plastic stencil was used for the full 24 hours for scanning to circumvent this problem.

Figure 26: Slab 3 - Marked Slab Surface

Even while delaying scanning to 1.5 hours after casting, the slab was not fully hardened, and as a result, the handheld cart and plastic sheet left marks on the top surface of the slab. The extent of this is due to the high slump of this specific specimen, so another specimen with lower slump (such as less than 4” (10.16 cm)) would not exhibit the same surface deterioration and the elevated stencil could be used without issue. The marks and indentations caused by the GPR handheld cart and plastic scanning sheet can be seen in Figure 26.

5.2. Field Work Results

After completing lab casting and testing, a six-week old section of pavement on Highway 30, west of North Bend, NE was field tested using a modified GPR detection technique previously developed and tested in the laboratory. A 4’ x 4’ x 0.75” (1.22 m x 1.22 m x 1.9 cm) sheet of plywood with screws on the four corners (to elevate it 0.5” (1.27 cm) above the concrete) was laid on the pavement, and the GPR scans were conducted on a 4” x 4” (10.16 cm x 10.16 cm) grid. The 4” x 4” (10.16 cm x 10.16 cm) grid was marked on the plywood sheet for ease of use.

Three 4” x 4” (10 cm x 10 cm) sections of pavement were scanned on site; scans were not done on a 2” x 2” (5.08 cm x 5.08 cm) grid, as the it was desirable to scan as many different spots as possible and it was faster to scan at 4” x 4” (10.16 cm x 10.16 cm) o.c. GPR scans did not pick up any voids in the top four inches of the pavement (Figure 27) leading to the conclusion that the areas scanned were adequately consolidated.

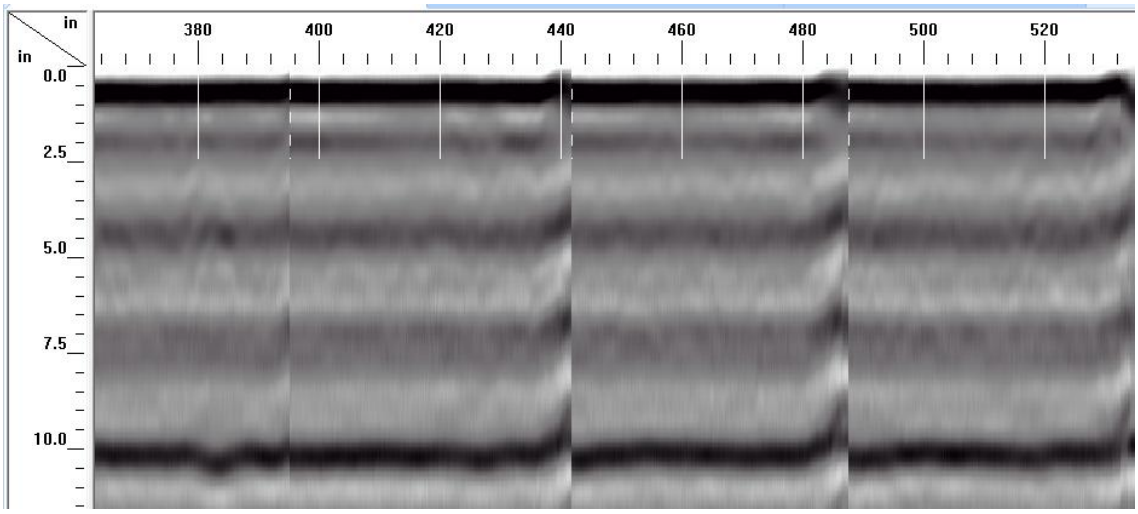

Figure 27: Field Experiment - GPR Scan Outputs

Figure 27 shows a typical GPR scan output from the site. Three cores were taken to validate the GPR scans, and can be seen in Figure 28 through Figure 30.

Figure 28: Field Experiment - Core 1

Figure 29: Field Experiment - Core 2

Figure 30: Field Experiment - Core 3

Coring at each scanning location yielded no voids of the size NDOT would be concerned with in that region as leading to the conclusion that there was proper consolidation at this location and the experiment was successful.

Chapter 6. Conclusions and Future Work

This thesis' aim was to push the thus-far assumed limitations of the use of GPR on fresh concrete pavement for honeycombing detection, as well as to track the change in dielectric constant during the first 24 hours of a lab specimen's lifetime. The objectives were to first, determine the earliest time during the dormant, setting, and early hardening periods of concrete's set that GPR can be used to detect shallow air voids. Secondly, the change in dielectric constant was tracked over the first 24 hours of concrete setting in order to quantify the impact of the dielectric constant assumptions in early detection.

6.1. Conclusions and Limitations

GPR is capable of detecting air voids (honeycombing) ranging in size from 1.5" (3.81 cm) to 4" (10.16 cm) in the top 4" (10.16 cm) of concrete pavement as early as three hours after casting. Honeycombing in this depth range (the top 4" (10.16 cm)) is critical to prevent for pavement durability; the effects of deeper voids were not studied in these experiments. GPR scanning and detection of air voids as early as three hours is possible with an error margin of less than 3% or 1.5" (3.81 cm), as verified by concrete cores. Larger errors leading to detected locations greater than 2" (5.08 cm) off of the physical honeycombing locations are possible, if a stencil is used for gridlines and the start line of scans shift slightly from the intended origin at a particular reading.

Scanning at 2" (5.08 cm) o.c. is recommended for better detection accuracy. However, scanning at 4" (10.16 cm) o.c. still provides acceptable detection accuracy and saves scanning time. An elevated plywood scanning grid can be used above the concrete with

no contact to the surface to avoid damaging curing compound sprayed on top of the concrete pavement. If using an elevated stencil, a mix with a low slump is recommended to prevent sinkage of screws on the stencil corners and subsequent destabilization of the scanning surface in the first 4.5 hours after casting. Since many pavement mix designs have slumps less than 4" (10.16 cm), the elevated stencil will be able to be used without damaging the pavement's surface. For higher slump mixes, it is still possible to use the elevated stencil for scanning after the 4.5 hour mark, but care must be taken to avoid damage to the surface. With carefully laid scan grids and post-processing, GPR can be an accurate NDE method for the early detection (as early as 3 hours from casting) of honeycombing in concrete pavements.

Furthering the application of early detection, monitoring the change in dielectric constant over the first 24 hours of a specimen's lifetime yields data that can be used in future fieldwork. The change in dielectric constant trends downward at an average of 2.0% for the first 4.5 hours, 4.4% from hours 5.5 – 8.5, and leveled off between hours 10.5 and 13.5, before experiencing a drop before leveling off again at hour 15.5. Even though this concrete mix was different than the one used for the first two specimens, when the variation of dielectric constant is considered, the error margin previously established remains at less than 3%. While this particular curve is unique to the specific type of concrete mix used in this experiment, similar curves can be constructed and used by researchers and DOTs for GPR scanning within the first 24 hours of pavement casting. Should researchers or DOTs test specimens with mix designs they frequently utilize in

highway pavement, they will have a growing archive of data and dielectric constant curves to reference should they need to calibrate GPR equipment in the field and detect subsurface voids in fresh and setting concrete pavement quickly and accurately. This will mitigate the need to calculate two-way-travel while in the field to determine an accurate dielectric constant for void detection and provide a quality control resource for reference both in further research and on construction sites.

6.2. Future Work

The overall goal of this study was to determine how early GPR could be used on fresh concrete pavement for honeycomb detection. The change in dielectric constant was also tracked over the first 24 hours of a specimen's lifetime as a calibration means for the first objective. The following recommendations are made for future research in the field of GPR and early void detection in concrete structures, including pavement:

- Further research studying concrete with varying fluidity and w/c ratios and their immediate, short, and long-term effects on the dielectric constant.
- Testing of different concrete mix designs other than NDOT's 47B to expand available data on the change in dielectric constantant as it varies with mix design and compiling a database of graphs for different concrete mixes tracking the change in dielectric constant for the first 24 or 36 hours after casting.
- Research into the long-term effects of deeper honeycombing (greater than 4" (10.16 cm) deep) and its effect on pavement durability.

Chapter 7. References

Al-Qadi, I., Lahouar, S., and Loulizi, A. (2003). Successful Application of Ground-Penetrating Radar for Quality Assurance-Quality Control of New Pavements. *Transportation Research Record: Journal of the Transportation Research Board,1861,* 86-97. doi:10.3141/1861-10

Baker, Gregory S., et al. "An Introduction to Ground Penetrating Radar (GPR)." Special Paper 432: Stratigraphic Analyses Using GPR, 2007, pp. 1–18., doi:10.1130/2007.2432(01).

Benedetto, A., Tosti, F., Ciampoli, L. B., and D'Amico, F. (2017). An overview of ground-penetrating radar signal processing techniques for road inspections. *Signal Processing,132,* 201-209. doi:10.1016/j.sigpro.2016.05.016

Bungey, J. H., Millard, S. G. Radar inspection of structures. Proc Inst Civil Engrs Struct Bldgs 1993;99:173-86.

Cassidy, N. J., Eddies, R., and Dods, S. (2011). Void detection beneath reinforced concrete sections: The practical application of ground-penetrating radar and ultrasonic techniques. *Journal of Applied Geophysics,74*(4), 263-276.

Daniels, D. J. Surface penetrating radar. Inst Elect Engrs 1996:300.

Eghtesadi, S., and Nokken, M. (2017). Effect of Cracking and Improper Consolidation as Important Concrete Defects on Water Absorption and Electrical Conductivity. *Journal of Materials in Civil Engineering,29*(11), 04017201. doi:10.1061/(asce)mt.1943-5533.0002050

Fernandes, Francisco M., and Jorge C. Pais. “Laboratory Observation of Cracks in Road Pavements with GPR.” *Construction and Building Materials*, vol. 154, 2017, pp. 1130–1138., doi:10.1016/j.conbuildmat.2017.08.022.

Geophysical Survey Systems, Inc. *Concrete Handbook*. Geophysical Survey Systems, Inc., 2001, http://gpr.quickbitllc.com/gssi-concrete-handbook.pdf.

http://gprrental.com/gpr-velocity-table-analysis/

https://www.fhwa.dot.gov/pavement/concrete/scant2.cfm

Jol, H. M. *Ground Penetrating Radar Theory and Applications*. Elsevier Science, 2009.

Lahouar, S., I. L. Al-Qadi, A. Loulizi, T. M. Clark, and D. T. Lee. Approach to Determining In-Situ Dielectric Constant of Pavements: Development and Implementation at Interstate 81 in Virginia. *In Transportation Research Record: Journal of the Transportation Research Board, No. 1806*, TRB, National Research Council, Washington, D.C., 2002, pp. 81–87.

Li, M., Anderson, N., Sneed, L., and Torgashov, E. (2016). Condition assessment of concrete pavements using both ground penetrating radar and stress-wave based techniques. *Journal of Applied Geophysics*,*135*, 297-308. doi:10.1016/j.jappgeo.2016.10.022

Liu, J., Zollinger, D. G., and Lytton, R. L. (2008). Detection of Delamination in Concrete Pavements Using Ground-Coupled Ground-Penetrating Radar Technique. *Transportation Research Record: Journal of the Transportation Research Board*,*2087*(1), 68-77. doi:10.3141/2087-08

Maierhofer, C. (2003). Nondestructive Evaluation of Concrete Infrastructure with Ground Penetrating Radar. *Journal of Materials in Civil Engineering,15*, 287-297.

McCabe, T., Erdogmus, E., Kodsy. A, and Morcous, G. (2021). "Early Detection of Honeycombs in Concrete Pavement Using GPR," *Journal of Performance of Constructed Facilities*, 2021, 35(1), ASCE.

Morcous, G., and Erdogmus, E. (2010). "Accuracy of Ground-Penetrating Radar for Concrete Pavement Thickness Measurement," *ASCE Journal of Performance of Constructed Facilities*, ASCE, 24 (6), November/December 2010.

Moruza, G. M., and Ozyildirim, H. C. (2017). Self-Consolidating Concrete in Virginia Department of Transportation's Bridge Structures. *ACI Materials Journal,114*(1). doi:10.14359/51689480

"NDOT on Pothole Patrol." *Official Nebraska Deparment of Transportation Website*, 3 Apr. 2018, dot.nebraska.gov/news-media/transportation-tidbits/ndot-on-pothole-patrol/.

Owsiak, Z. & Zapała-Sławeta, Justyna & Czapik, Przemysław. (2015). Diagnosis of concrete structures distress due to alkali-aggregate reaction. Bulletin of the Polish Academy of Sciences, Technical Sciences. 63. 10.1515/bpasts-2015-0003.

Ozyildirim, C. (2004). Air-Void Characteristics of Concretes in Different Applications. *Transportation Research Record: Journal of the Transportation Research Board,1893*, 70-74. doi:10.3141/1893-09

Perrot, A., and Rangeard, D. (2016). Effects of mix design parameters on consolidation behavior of fresh cement-based materials. *Materials and Structures,50*(2), 117. doi:10.1617/s11527-016-0988-0

Ristau, Reece. “Interstate Pothole Sidelines Four Vehicles at Once as DOT Fights a 'Continual Battle'.” *Omaha.com*, Omaha World Herald, 12 Mar. 2019, www.omaha.com/news/nebraska/interstate-pothole-sidelines-four-vehicles-at-once-as-dot-fights/article_d7fdb9c5-db7f-5efe-a9ed-2ad204e6cf99.html.

Shen, Peiliang, and Zhitian Liu. “Study on the Hydration of Young Concrete Based on Dielectric Property Measurement.” Construction and Building Materials, vol. 196, 2019, pp. 354–361., doi:10.1016/j.conbuildmat.2018.11.150

Shen, Peiliang, and Zhitian Liu. “Study on the Hydration of Young Concrete Based on Dielectric Property Measurement.” Construction and Building Materials, vol. 196, 2019, pp. 354–361., doi:10.1016/j.conbuildmat.2018.11.150

Soutsos, Marios, and Peter L. J. Domone. *Construction Materials: Their Nature and Behaviour*. CRC Press, 2018.

Study: Pothole Damage Costs U.S. Drivers $3B a Year. 16 Mar. 2016, www.insurancejournal.com/magazines/mag-features/2016/03/21/401900.htm.

US Bureau of Reclamation, 1955, Concrete Laboratory, Report No. C-810, Denver, CO.

Wightman, W. E., Jalinoos, F., Sirles, P., and Hanna, K. (2003). "Application of Geophysical Methods to Highway Related Problems." *Federal Highway Administration, Central Federal Lands Highway Division, Lakewood, CO, Publication No. FHWA-IF-04-021*, September 2003.

Chapter 8. Appendix

Slab 1

Void Photos

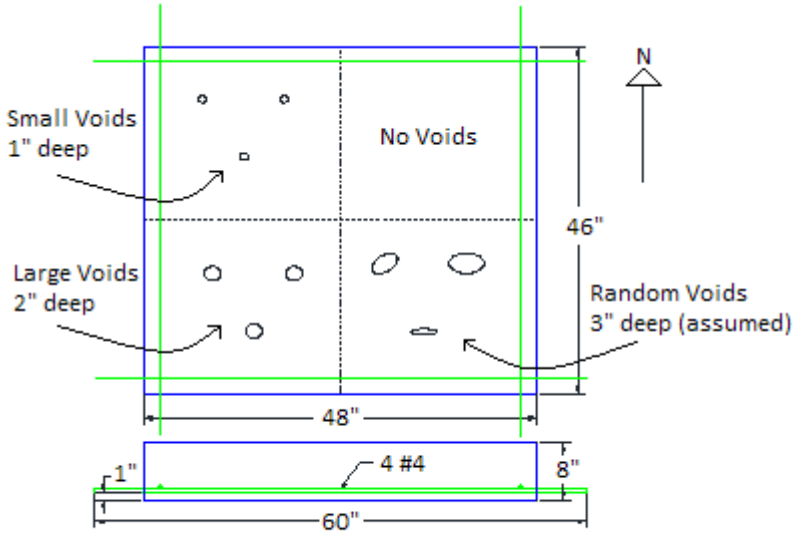

Figure 1: Slab 1 – Insulation Spray Foam Void Types and Depths with Rebar Locations

Figure 2: Slab 1 – Void 1

Figure 3: Slab 1 – Void 2

Figure 4: Slab 1 – Void 3

Figure 5: Slab 1 – Void 4

Figure 6: Slab 1 – Void 5

Figure 7: Slab 1 – Void 6

Casting Photos

Figure 8: Slab 1 – Formwork with Reinforcement

Figure 9: Slab 1 – Slump Measurement

Figure 10: Slab 1 – Concrete Vibration during Placement

Figure 11: Slab 1 – Finished Concrete Surface

Figure 12: Slab 1 –Measuring and Marking Quadrants

Figure 13: Slab 1 – Marked Slab Quadrants

Figure 14: Slab 1 – Measuring and Chalking GPR Scan Lines

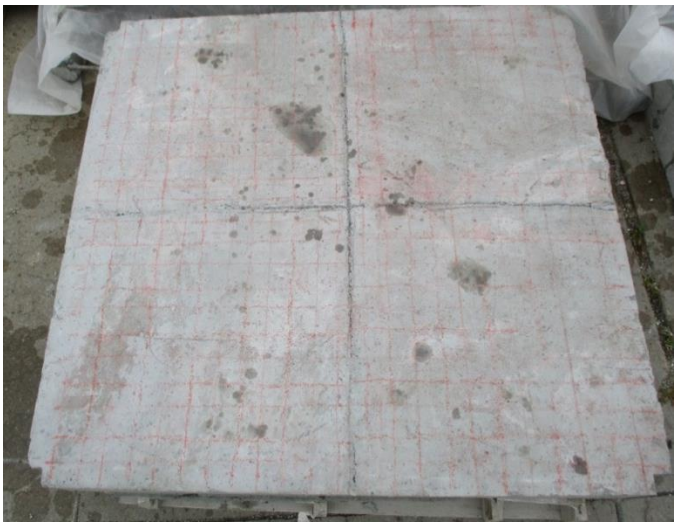

Figure 15: Slab 1 – Chalked Scan Gridlines with Quadrants

Figure 16: Slab 1 – Scanning with GPR

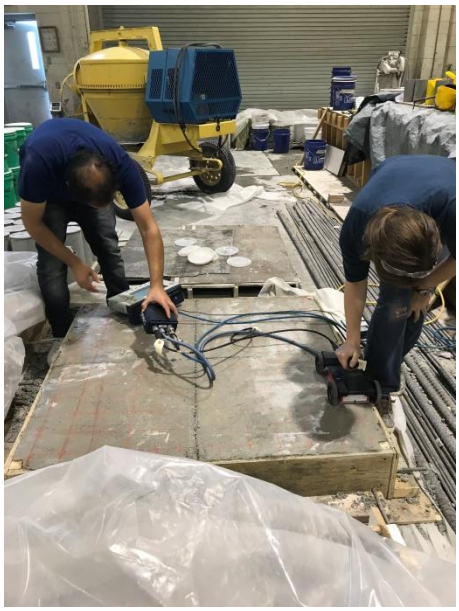

Figure 17: Slab 1 – Scanning with GPR

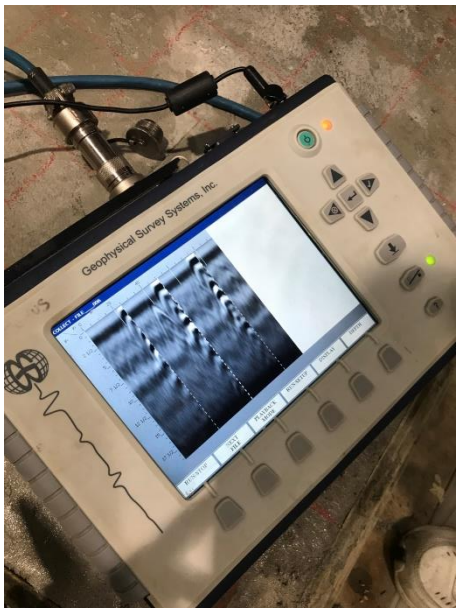

Figure 18: Slab 1 – GPR Equipment Visible Output with Detected Voids

GPR Scans

5 Hours From Production

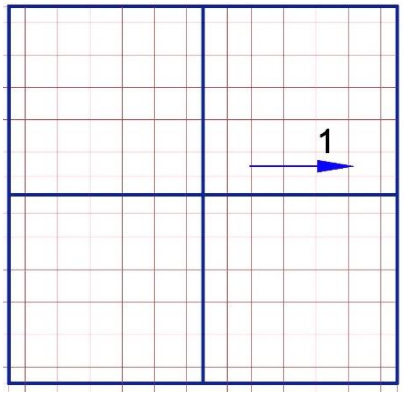

Figure 19: Slab 1 – Quadrant 1 Scan Guide (X-Direction)

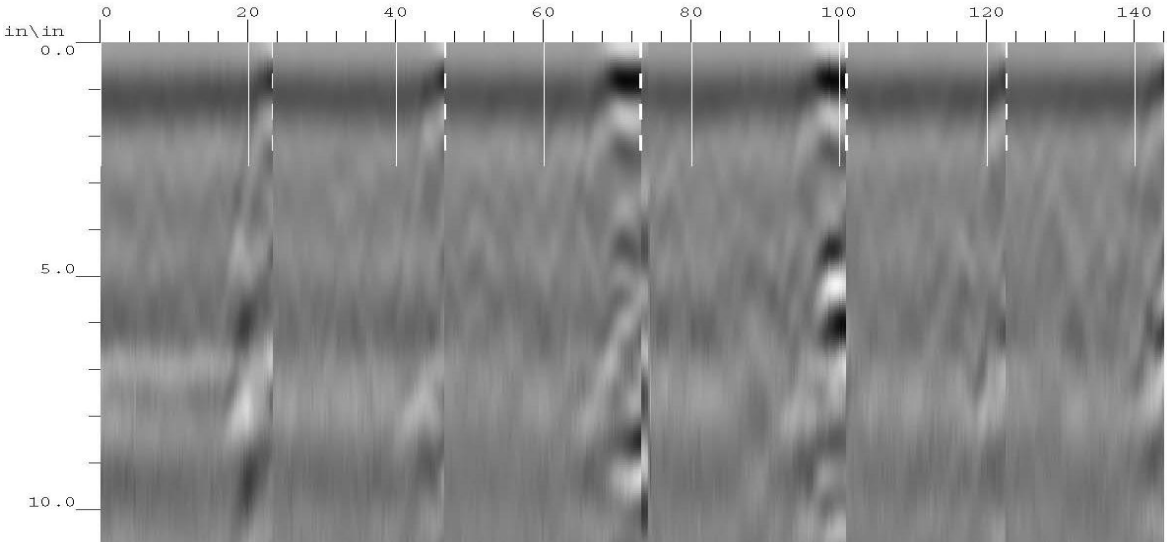

Figure 20: Slab 1 – Quadrant 1 Scan Output (X-Direction)

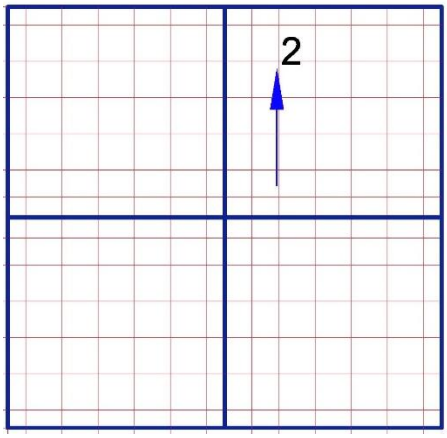

Figure 21: Slab 1 – Quadrant 1 Scan Guide (Y-Direction)

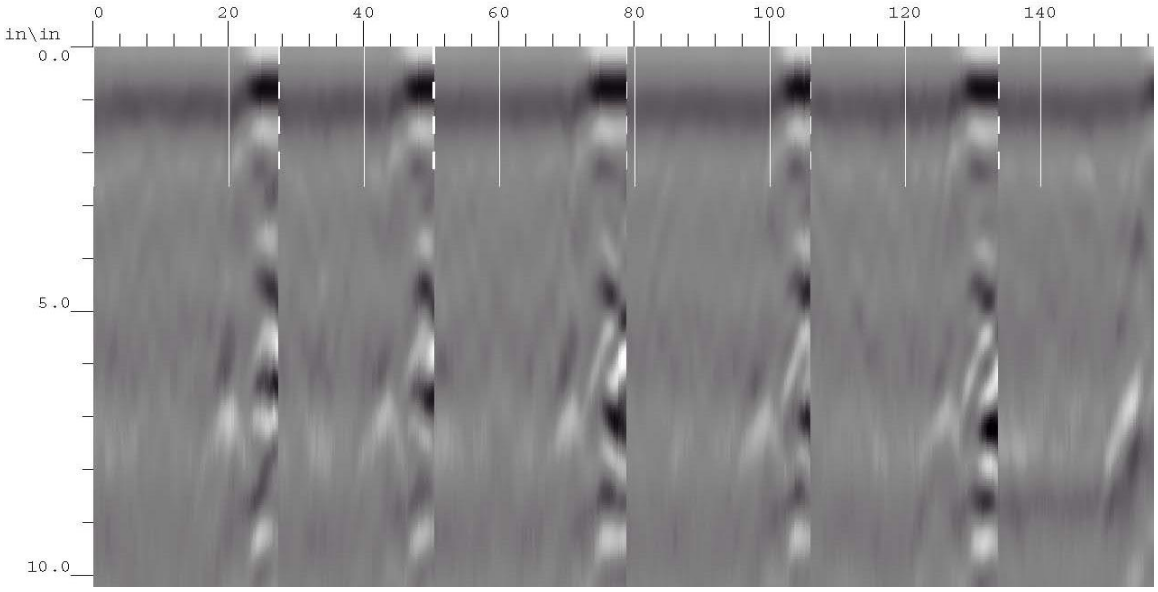

Figure 22: Slab 1 – Quadrant 1 Scan Output (Y-Direction)

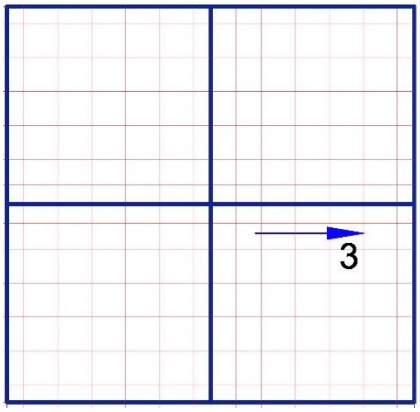

Figure 23: Slab 1 – Quadrant 2 Scan Guide (X-Direction)

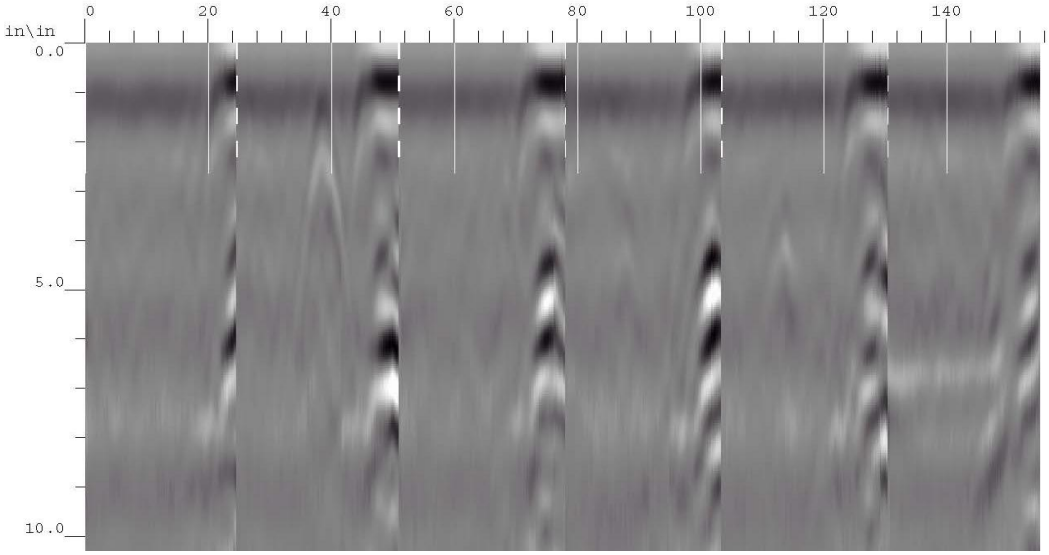

Figure 24: Slab 1 – Quadrant 2 Scan Output (X-Direction)

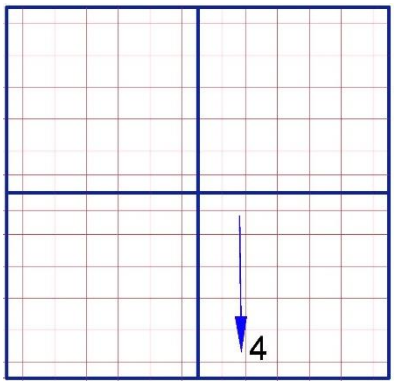

Figure 25: Slab 1 – Quadrant 2 Scan Guide (Y-Direction)

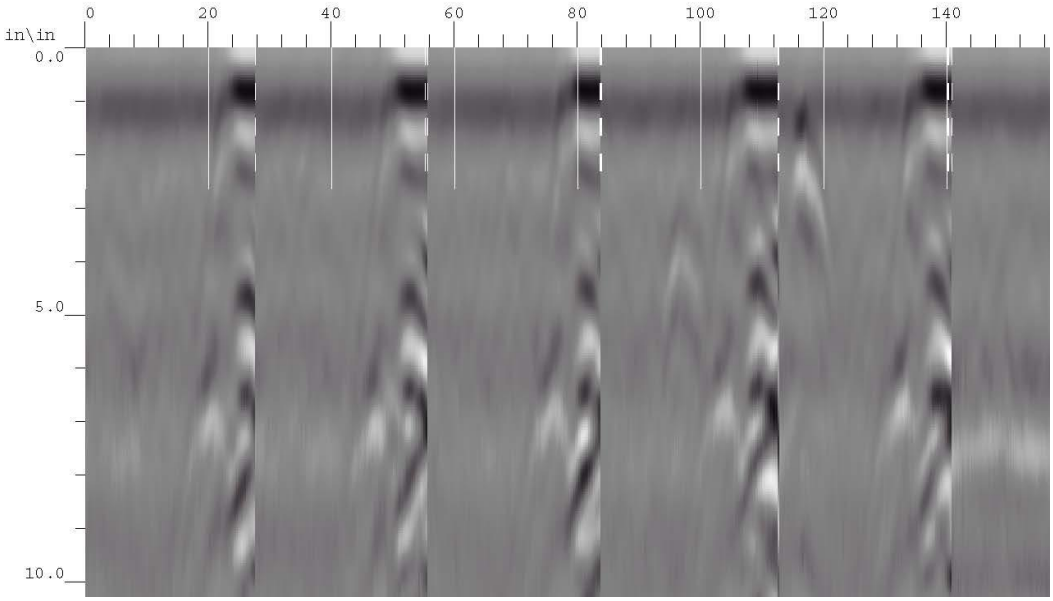

Figure 26: Slab 1 – Quadrant 2 Scan Output (Y-Direction)

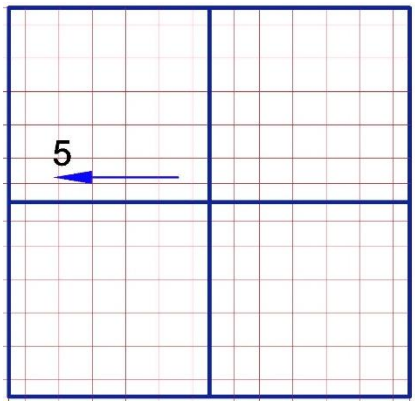

Figure 27: Slab 1 – Quadrant 3 Scan Guide (X-Direction)

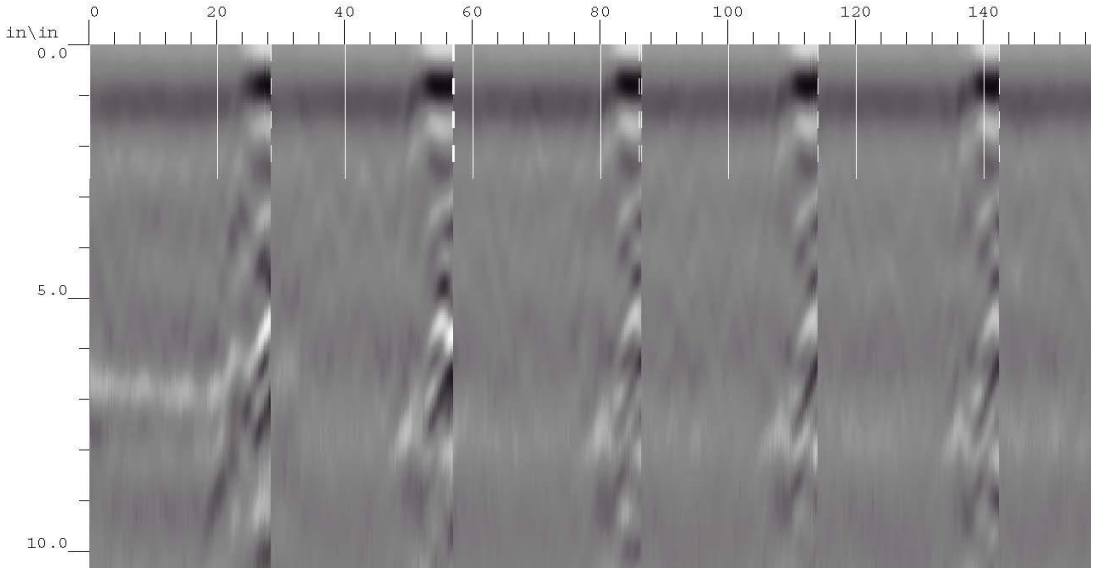

Figure: 28: Slab 1 – Quadrant 3 Scan Output (X-Direction)

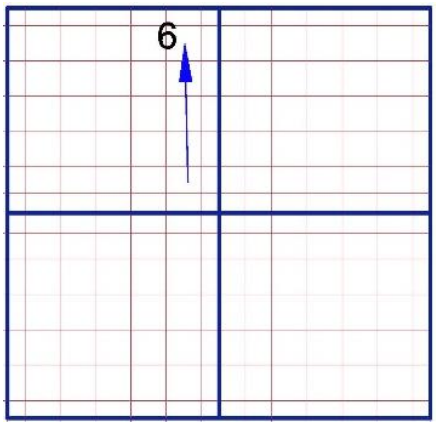

Figure: 29: Slab 1 – Quadrant 3 Scan Guide (Y-Direction)

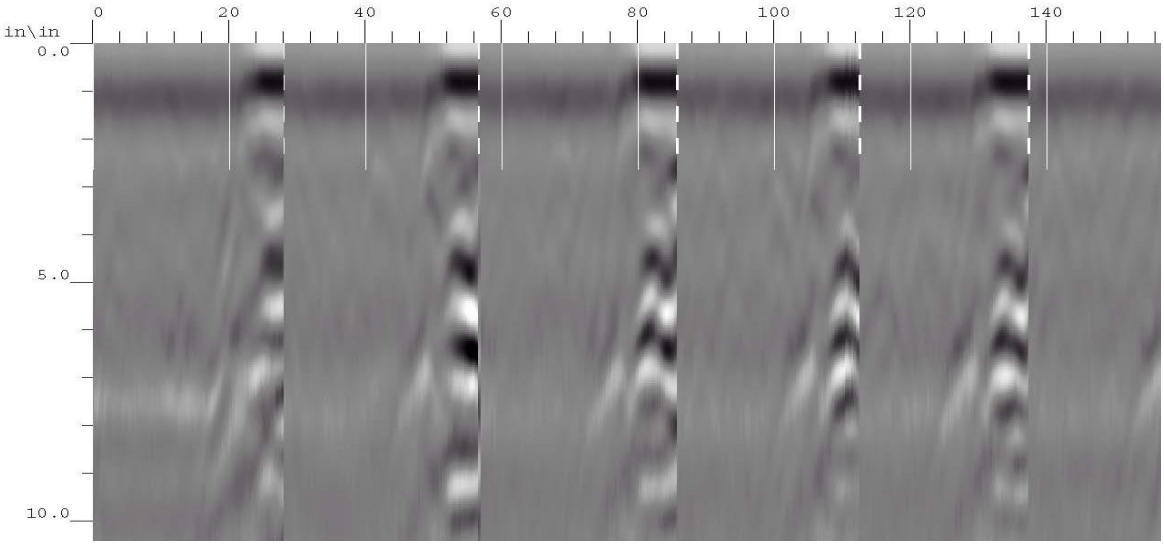

Figure: 30: Slab 1 – Quadrant 3 Scan Output (Y-Direction)

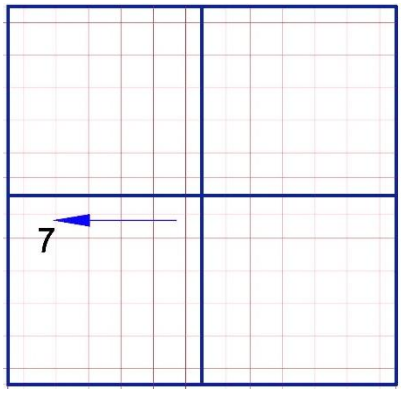

Figure: 31: Slab 1 – Quadrant 4 Scan Guide (X-Direction)

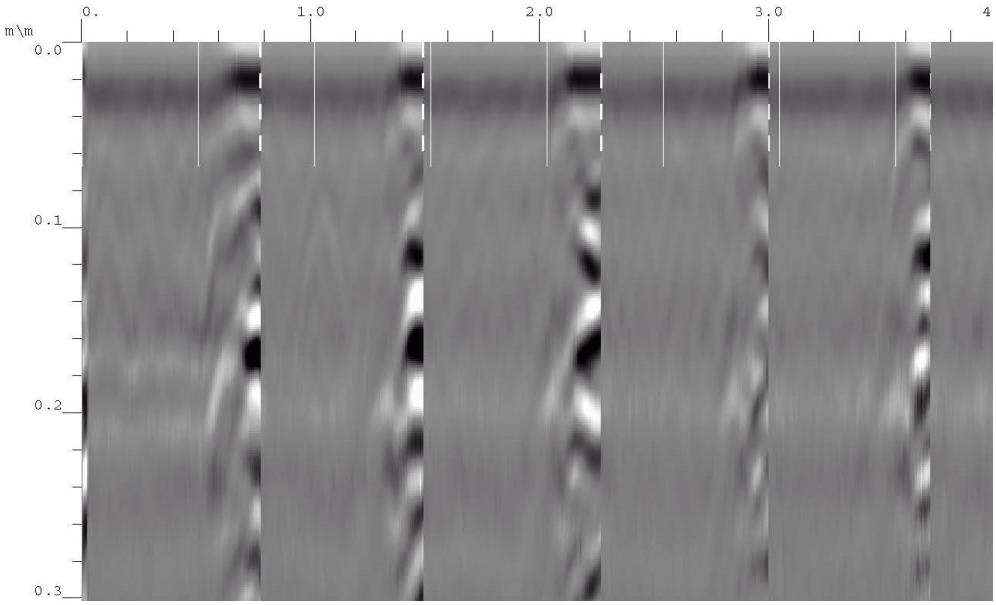

Figure: 32: Slab 1 – Quadrant 4 Scan Output (X-Direction)

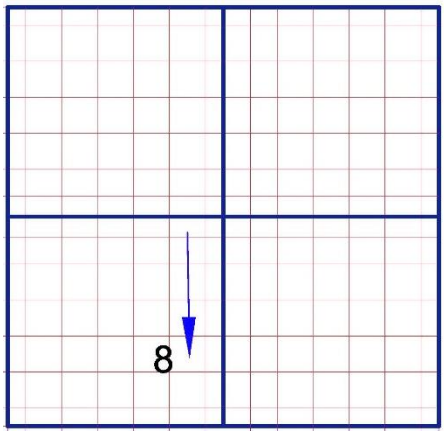

Figure: 33: Slab 1 – Quadrant 4 Scan Guide (Y-Direction)

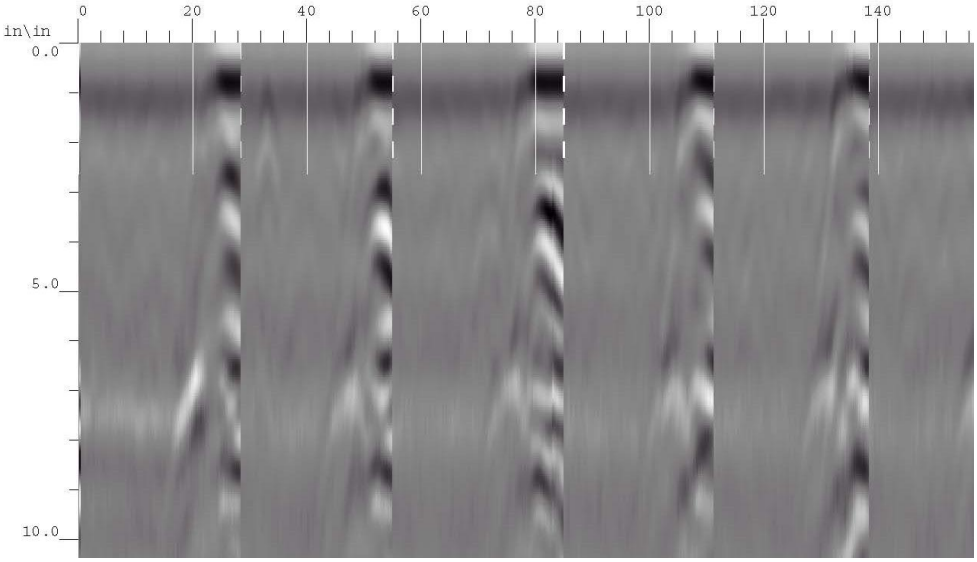

Figure: 34: Slab 1 – Quadrant 4 Scan Output (Y-Direction)

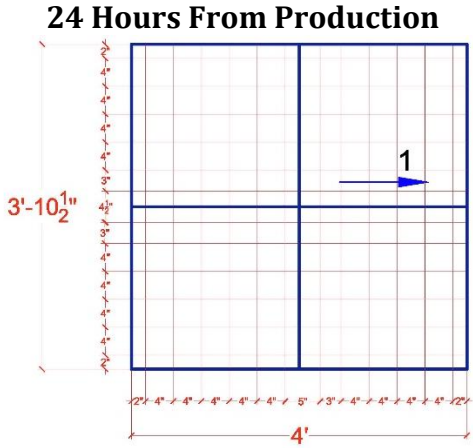

Figure: 35: Slab 1 – Quadrant 1 Scan Guide (X-Direction)

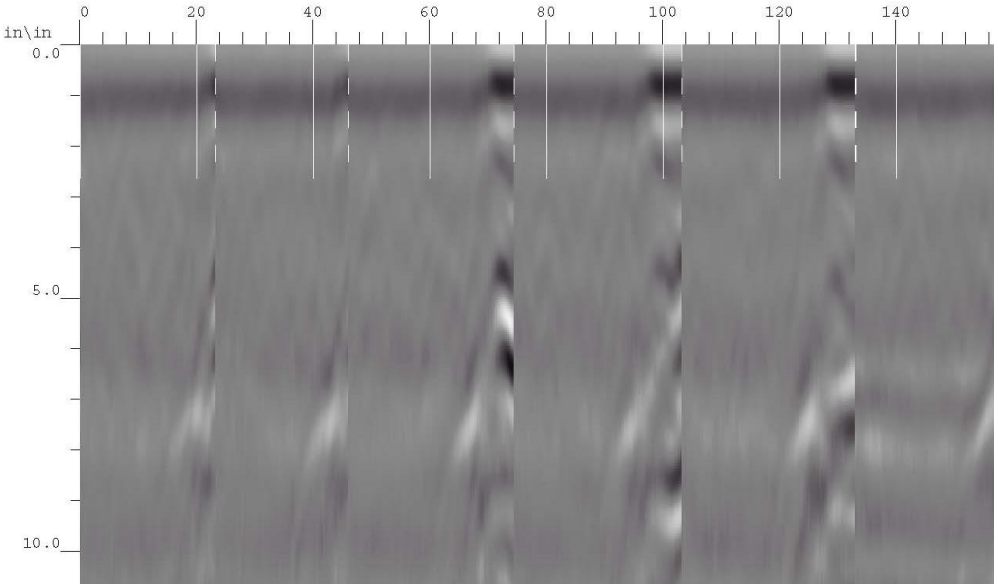

Figure: 36: Slab 1 – Quadrant 1 Scan Output (X-Direction)

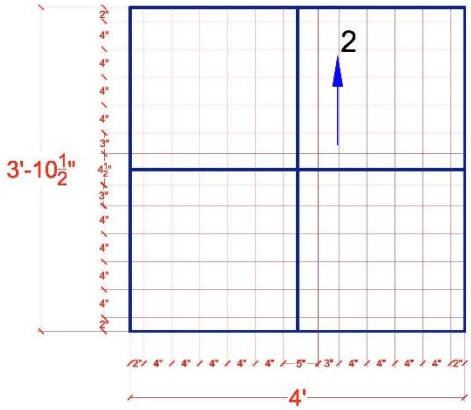

Figure: 37: Slab 1 – Quadrant 1 Scan Guide (Y-Direction)

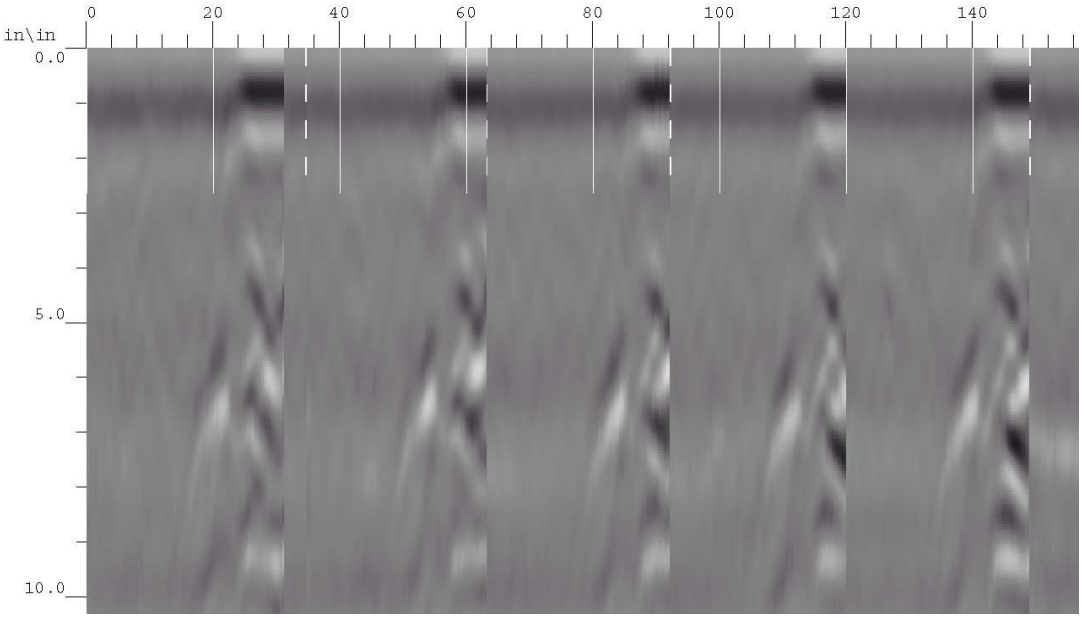

Figure: 38: Slab 1 – Quadrant 1 Scan Output (Y-Direction)

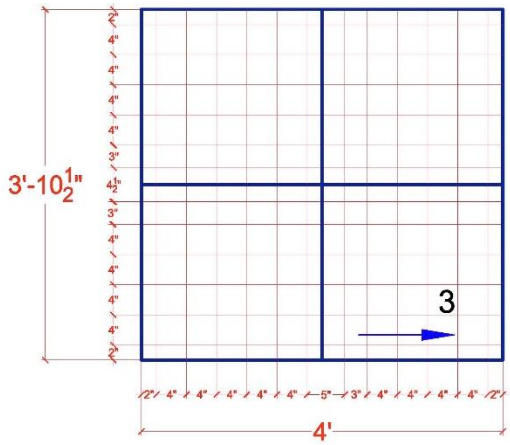

Figure: 39: Slab 1 – Quadrant 2 Scan Guide (X-Direction)

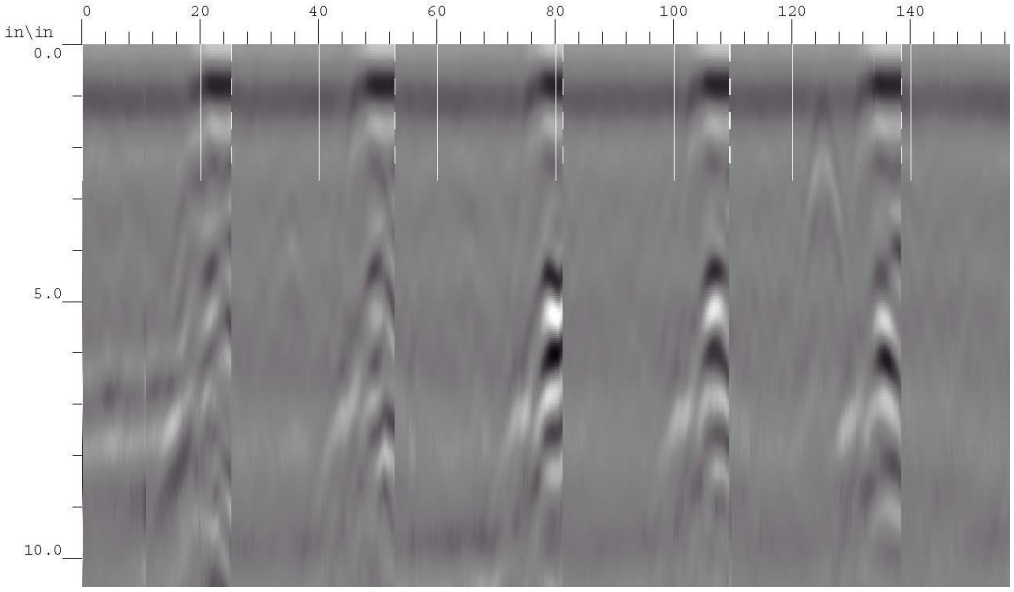

Figure: 40: Slab 1 – Quadrant 2 Scan Output (X-Direction)

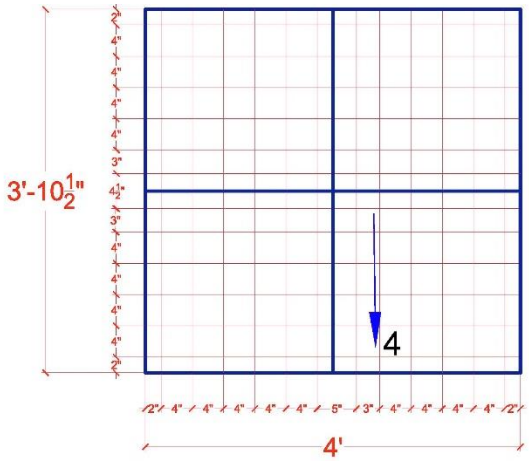

Figure: 41: Slab 1 – Quadrant 2 Scan Guide (Y-Direction)

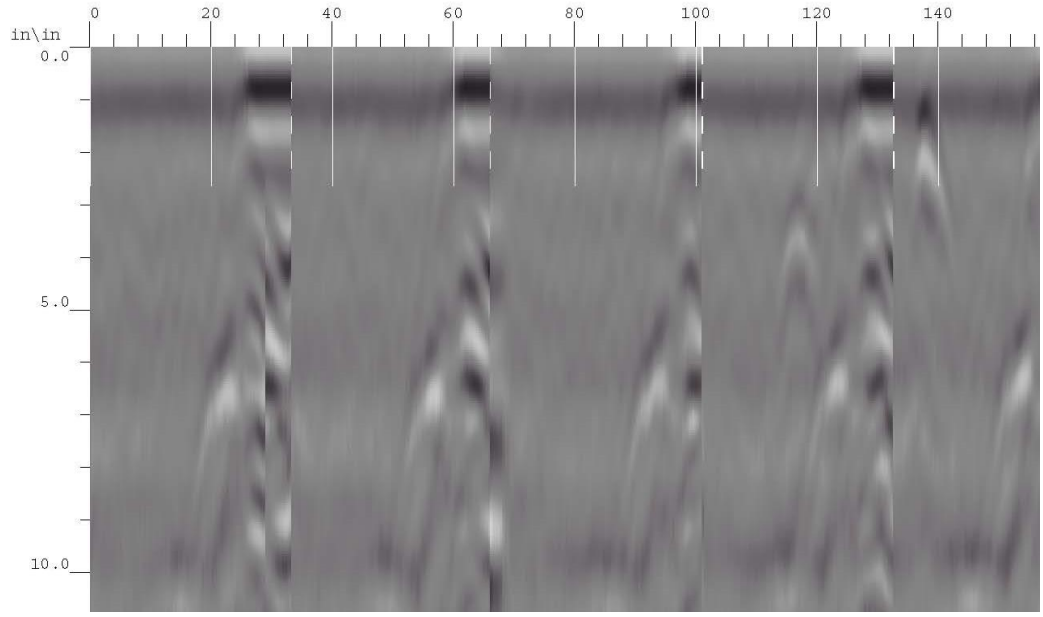

Figure: 42: Slab 1 – Quadrant 2 Scan Output (Y-Direction)

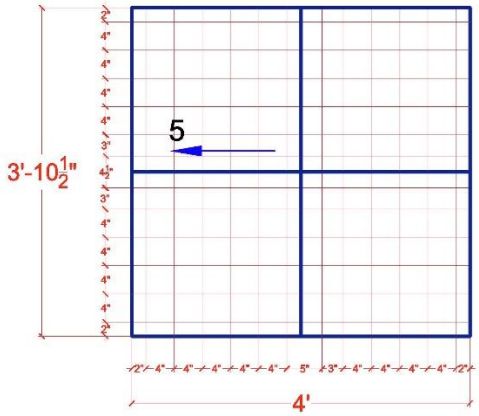

Figure: 43: Slab 1 – Quadrant 3 Scan Guide (X-Direction)

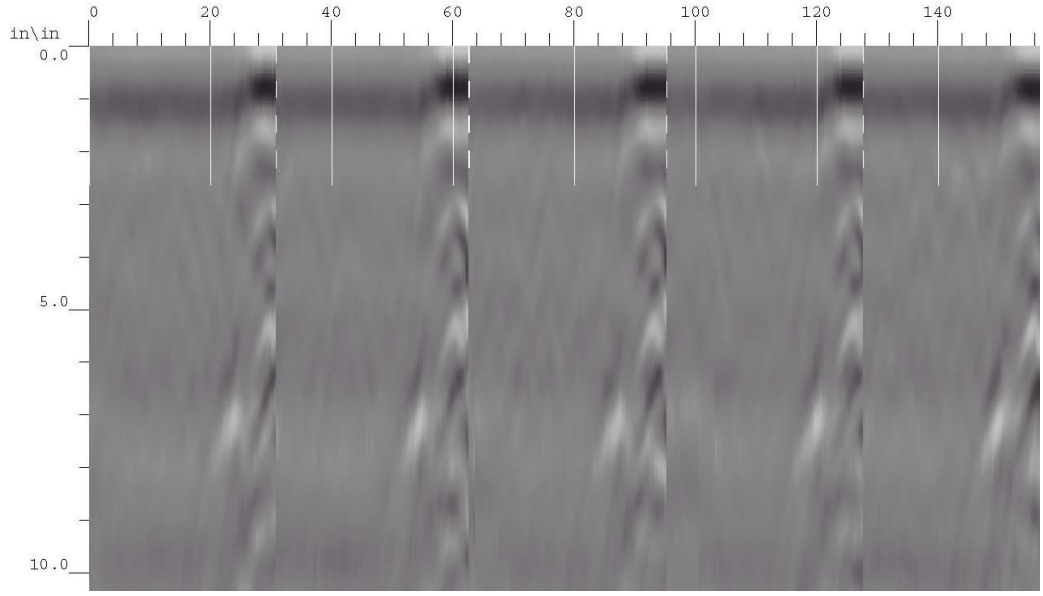

Figure: 44: Slab 1 – Quadrant 3 Scan Output (X-Direction)

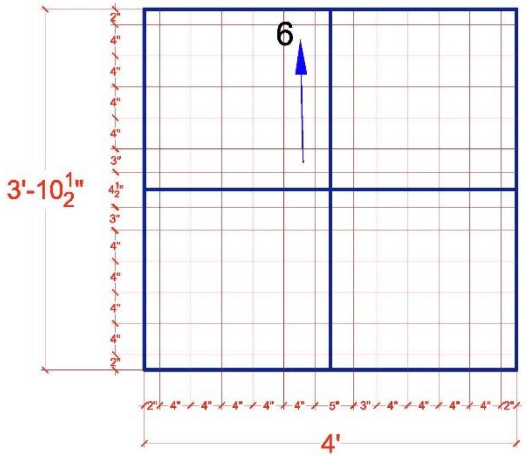

Figure: 45: Slab 1 – Quadrant 3 Scan Guide (Y-Direction)

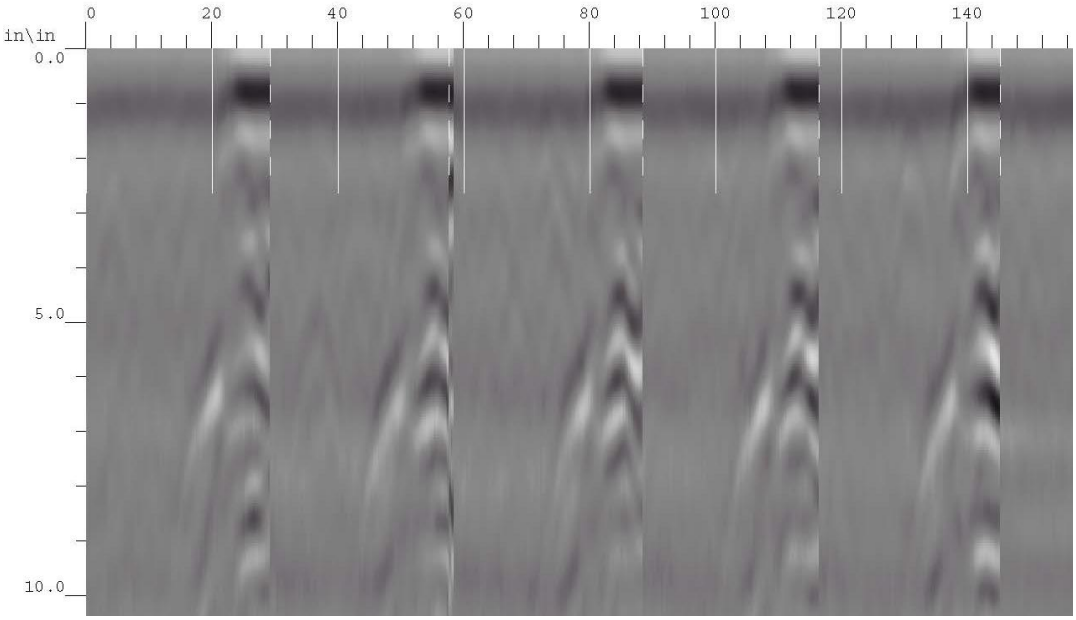

Figure: 46: Slab 1 – Quadrant 3 Scan Output (Y-Direction)

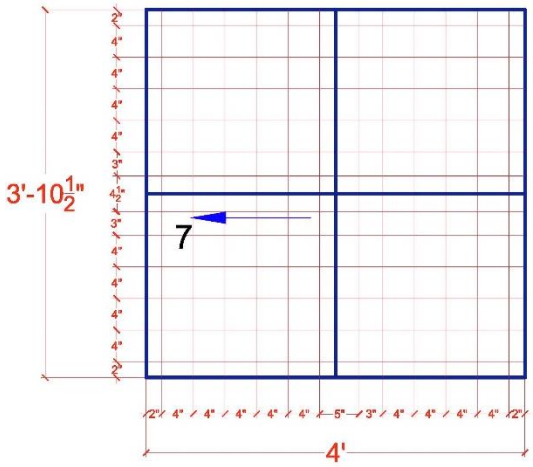

Figure: 47: Slab 1 – Quadrant 4 Scan Guide (X-Direction)

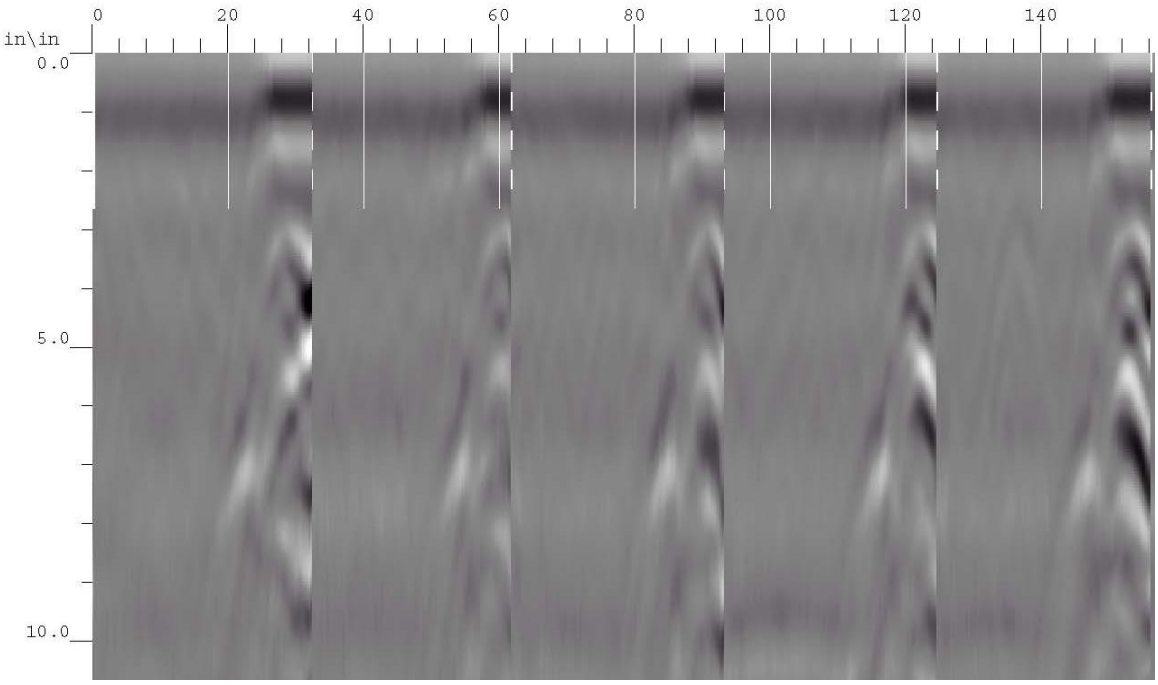

Figure: 48: Slab 1 – Quadrant 4 Scan Output (X-Direction)

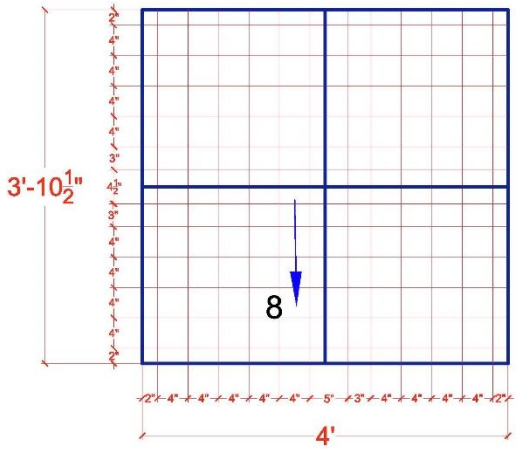

Figure: 49: Slab 1 – Quadrant 4 Scan Guide (Y-Direction)

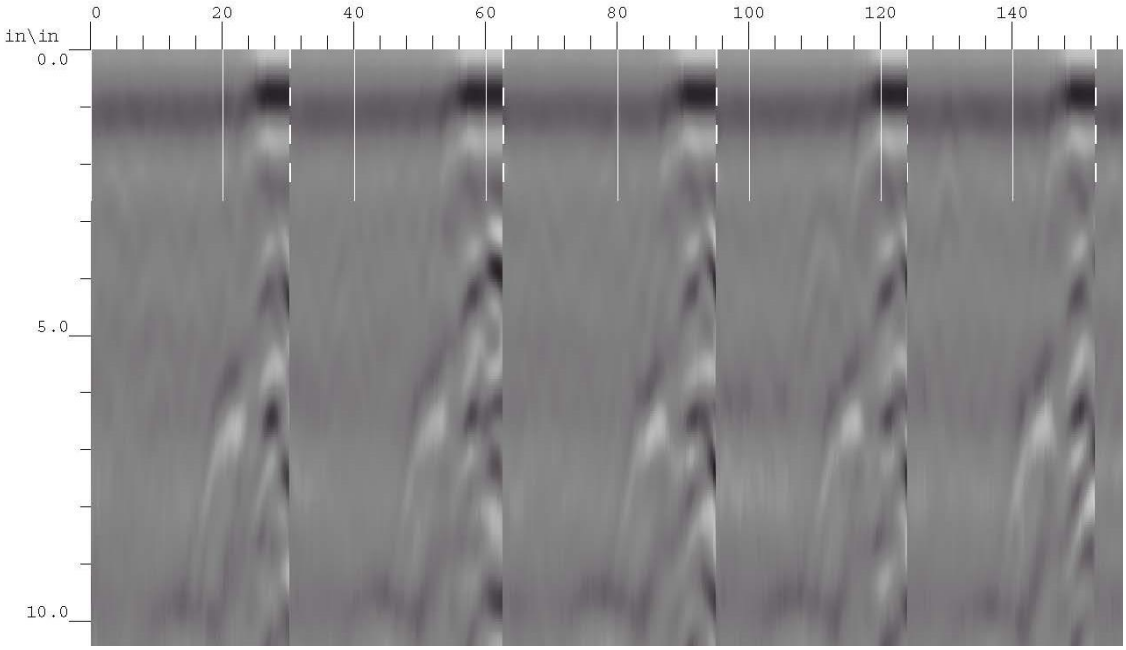

Figure: 50: Slab 1 – Quadrant 4 Scan Output (Y-Direction)

4 Days From Production

The following shows the direction of the scan's output for the X-direction grids and Y-direction grids presented continuously.

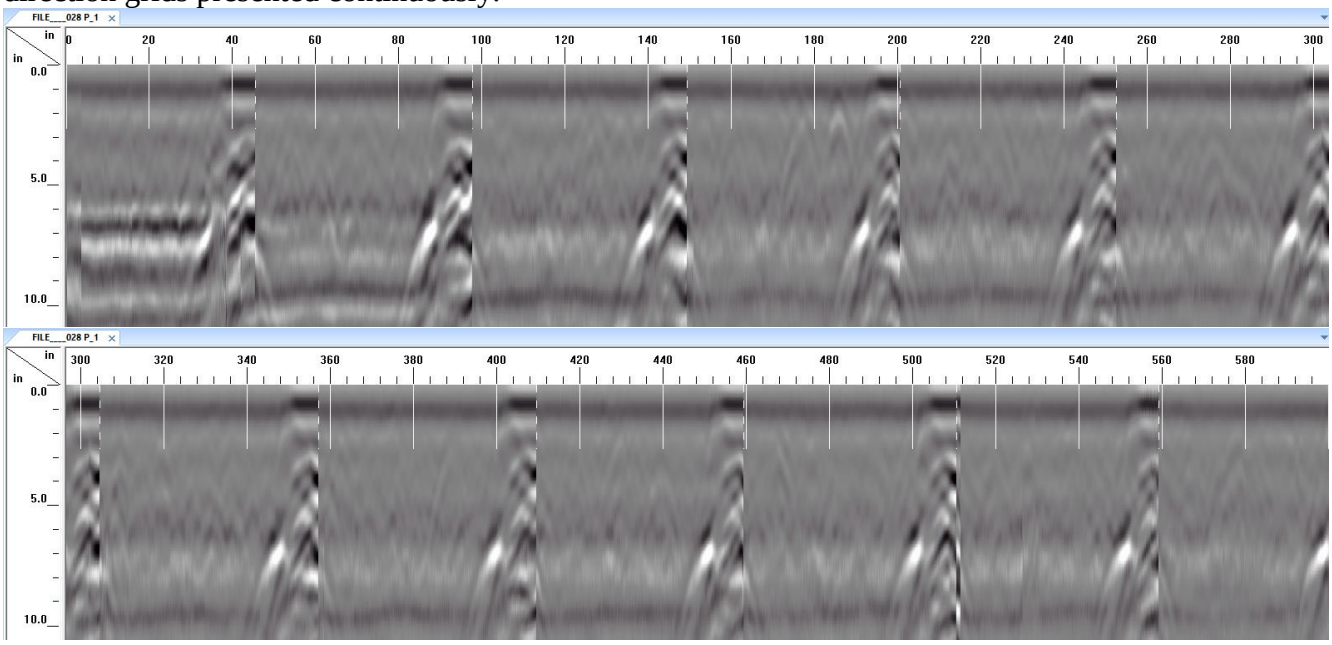

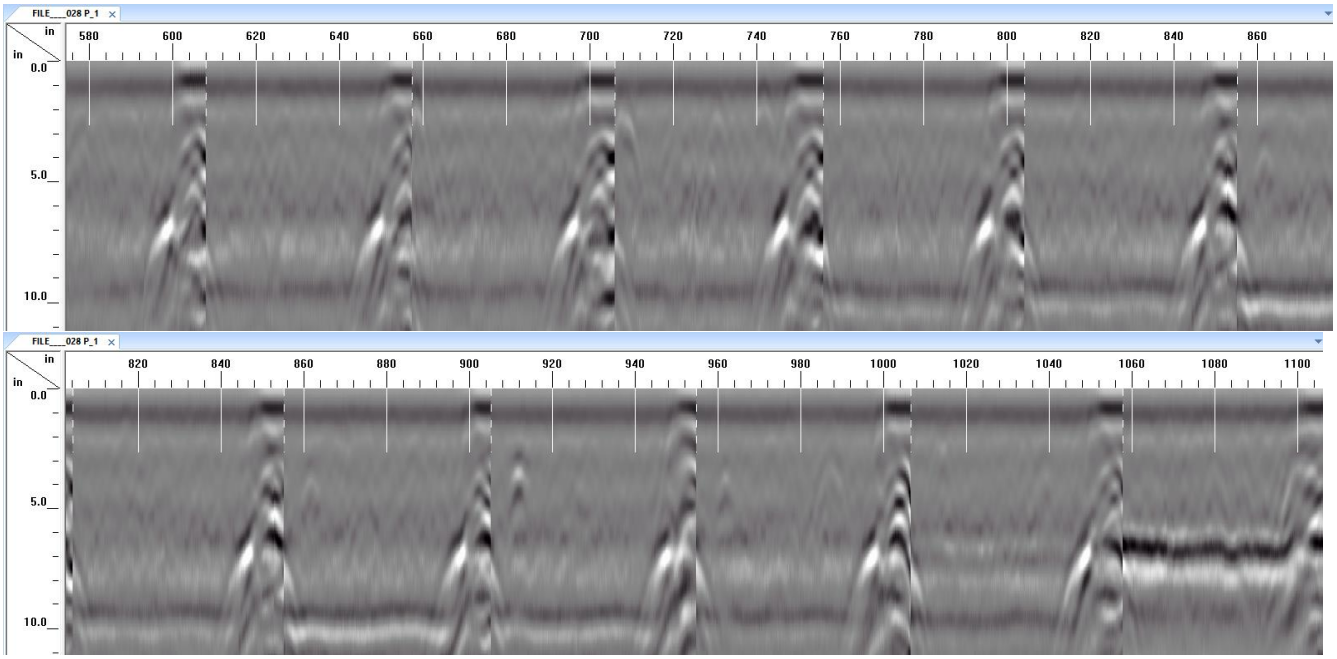

Figure: 51: Slab 1 – Continuous Scan Output (X-Direction)

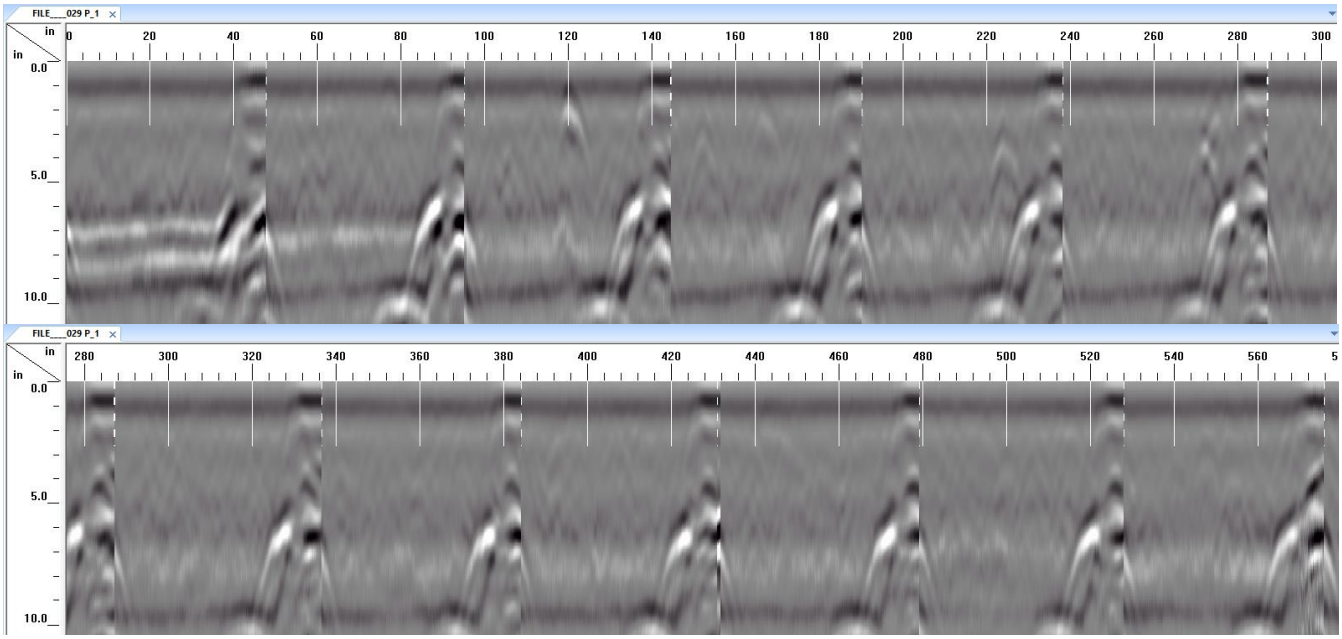

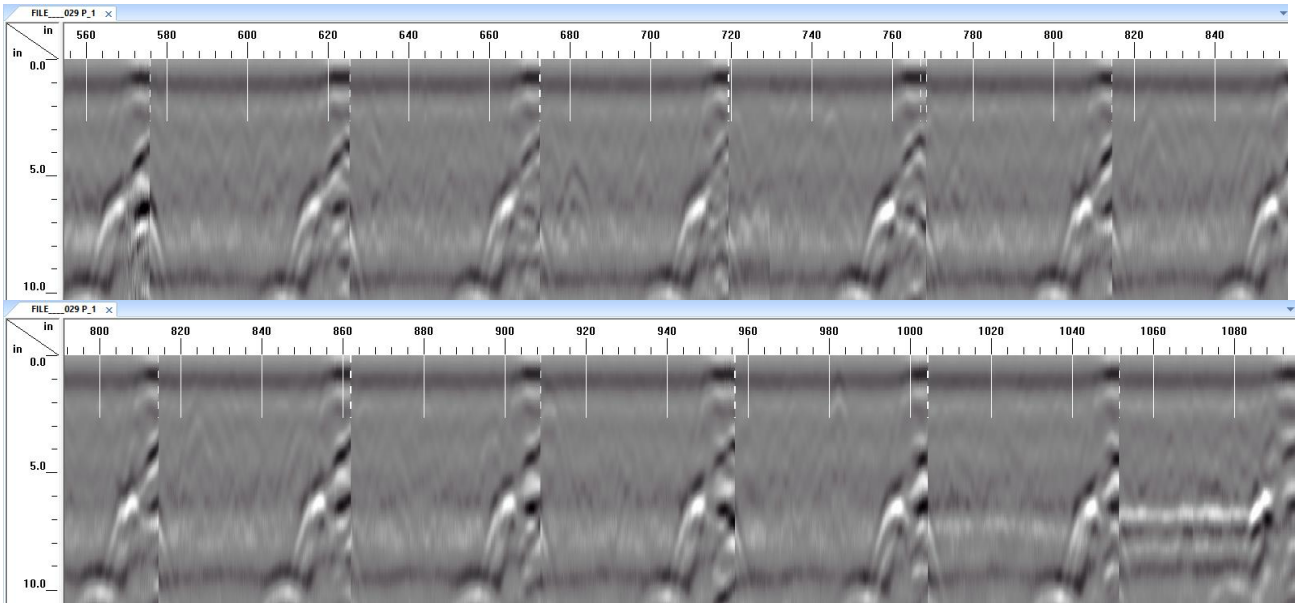

Figure: 52: Slab 1 - Continuous Scan Output (Y-direction)

9 Days From Production

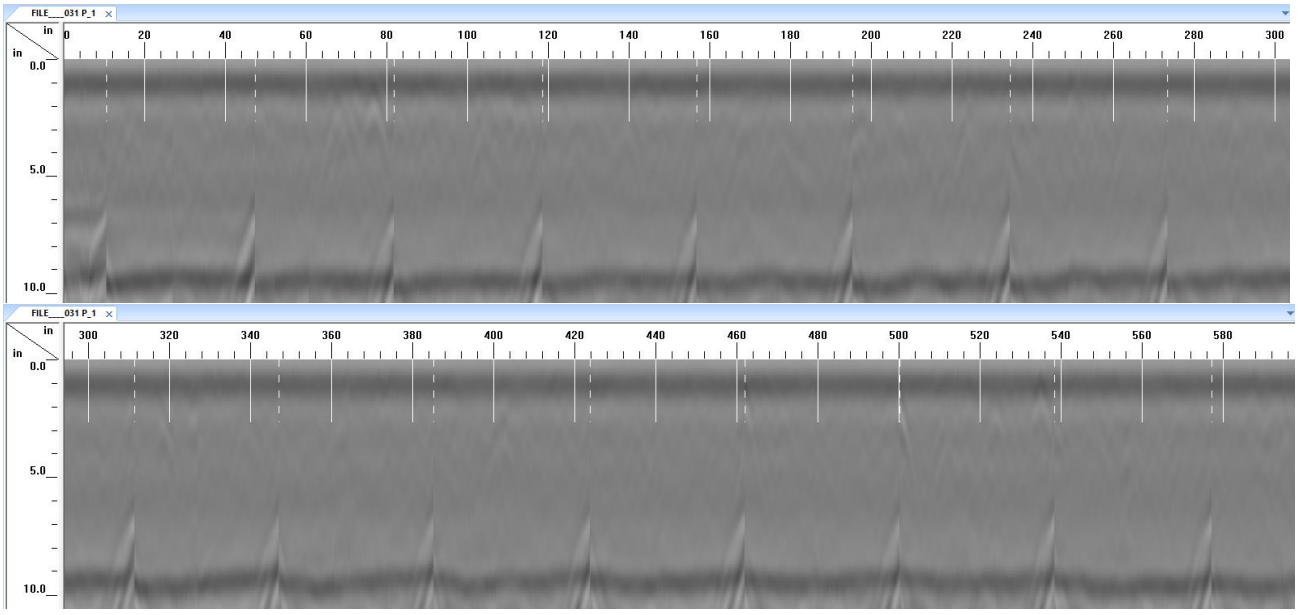

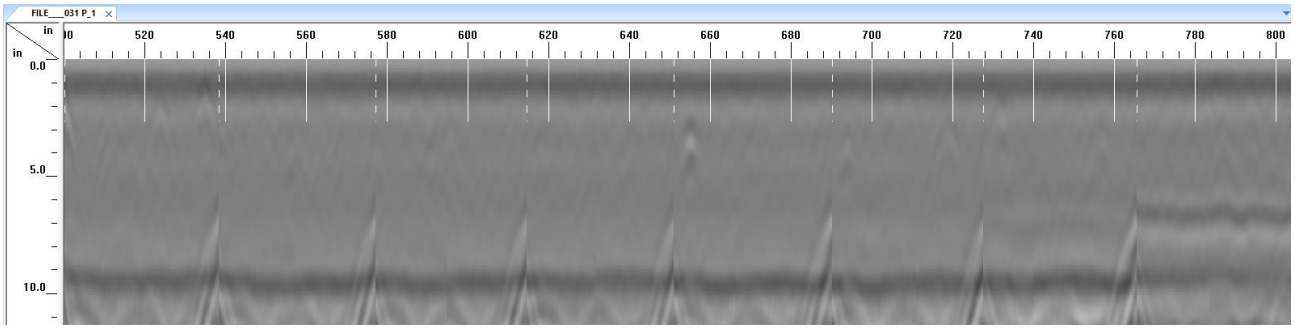

Figure 53: Slab 1 – Continuous Scan Output (X-Direction)

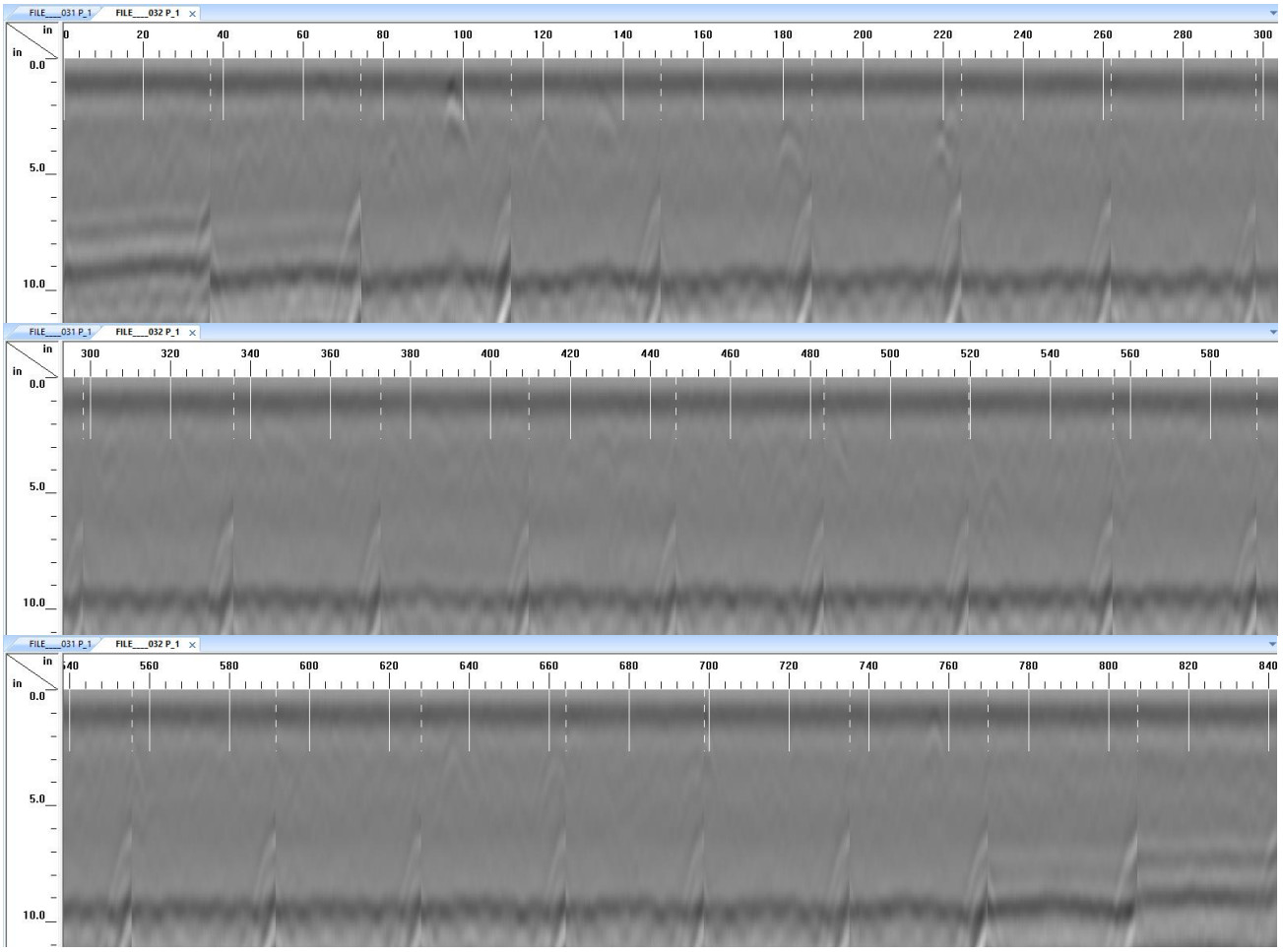

Figure 54: Slab 1 – Continuous Scan Output (Y-Direction)

Coring Photos

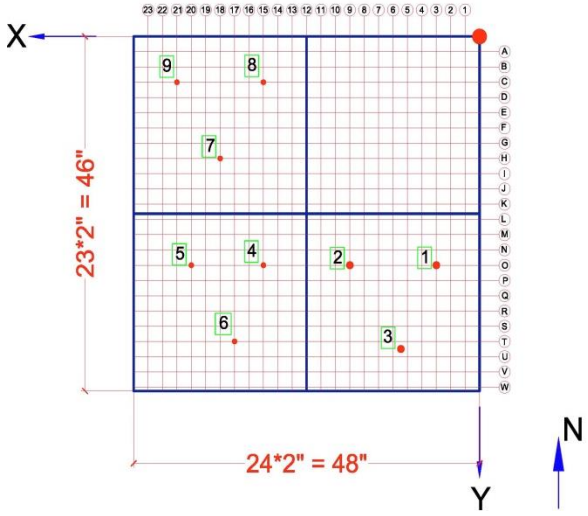

Figure 55: Slab 1 – Core Numbers and Locations

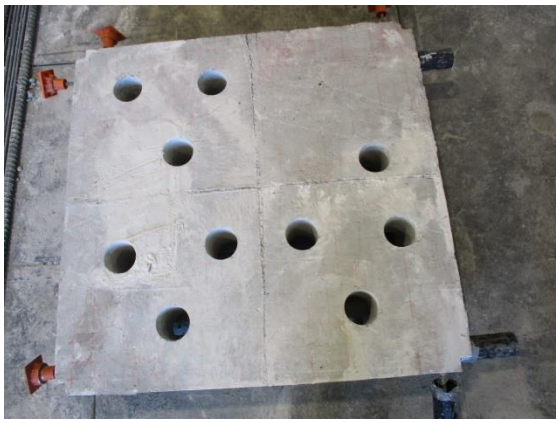

Figure 56: Slab 1 – Cored Slab

Figure 57: Slab 1 – Core 1

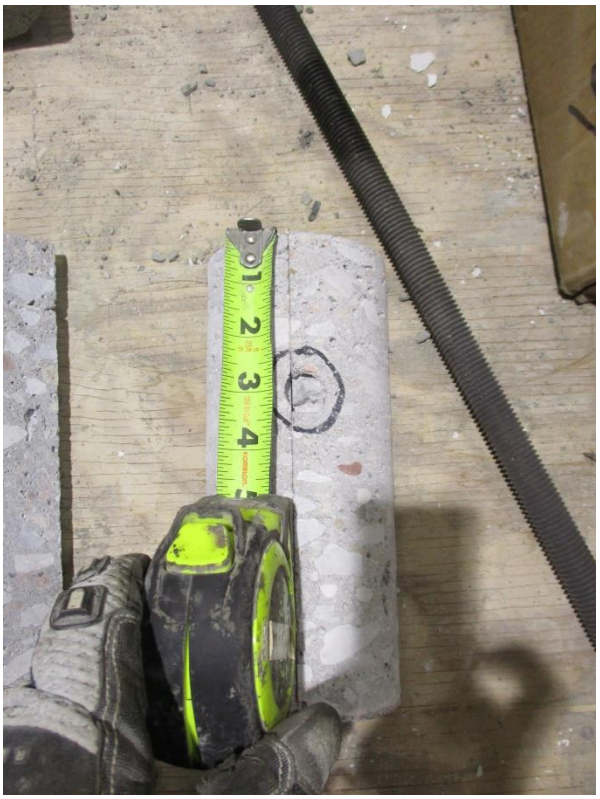

Figure 58: Slab 1 – Core 2

Figure 59: Slab 1 – Core 3

Figure 60: Slab 1 – Core 4

Figure 61: Slab 1 – Core 5

Figure 62: Slab 1 – Core 6

Figure 63: Slab 1 – Core 7

Figure 64: Slab 1 – Core 8

Figure 65: Slab 1 – Core 9

Figure 66: Slab 1 – Core 10

Slab 2

Void Photos

Figure 67: Slab 2 – Artificial Insulation Spray Foam Voids

Table 1: Slab 2 – Void Dimensions and Locations

Core No.	Void Size (Quadrant)	Void Dimension	Location from origin (Inches), (Meters)
1	Type One: Small (NW Corner)	2" x 1.5" (0.05m x 0.038m)	(12, 59), (0.3, 1.5)
2		2" x 1.75" (0.05m x 0.04m)	(14, 50), (0.4, 1.3)
3		1.5" x 1.5" (0.038m x 0.038m)	(23, 60), (0.6, 1.5)
4		2" x 1.5" (0.05m x 0.038m)	(23, 48), (0.6, 1.2)
5	Type One: Large (SW Corner)	2" x 2" (0.05 x 0.05m)	(11, 9), (0.3, 0.2)
6		2.5" x 2" (0.06m x 0.05m)	(26, 10), (0.7, 0.3)
7		2.5" x 1.75" (0.06m x 0.04m)	(13, 24), (0.3, 0.6)
8		4" x 1.5" (0.10m x 0.038m)	(26, 26), (0.7, 0.7)
9	Type One: Long (SE Corner)	3.75" x 1" (0.095m x 0.03m)	(64, 12), (1.6, 0.3)
10		5" x 1" (0.13m x 0.03m)	(51, 13), (1.3, 0.4)
11		5.75" x 1" (0.15m x 0.03m)	(60, 23), (1.5, 0.6)
12		6.5" x 1" (0.17m x 0.03m)	(46, 26), (1.2, 0.7)
13-16	Type Two: Compressed Air (NE Corner)	Random	Unknown

Casting Photos

Figure 68: Slab 2 – Formwork with Reinforcement

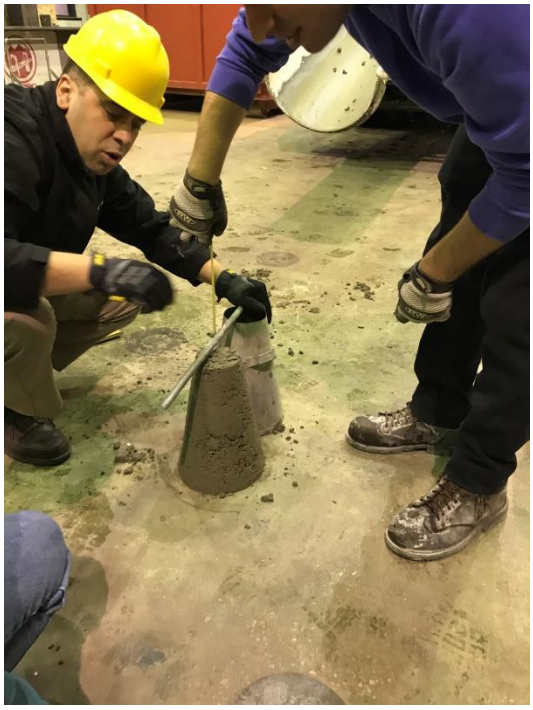

Figure 69: Slab 2 – Slump Testing

Figure 70: Slab 2 – Concrete Placement

Figure 71: Slab 2 – Concrete Vibration

Figure 72: Slab 2 – Concrete Cylinders for Testing

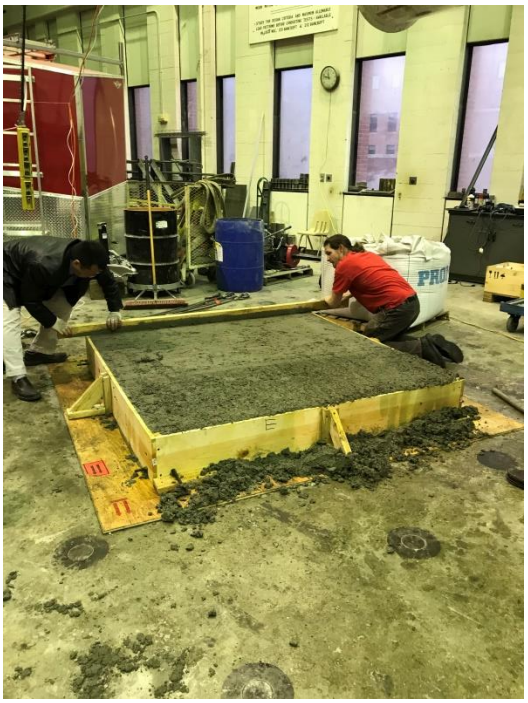

Figure 73: Slab 2 – Leveling for Finishing and Artificial Void Implantation

Figure 74: Slab 2 – Artificial Void Implantation

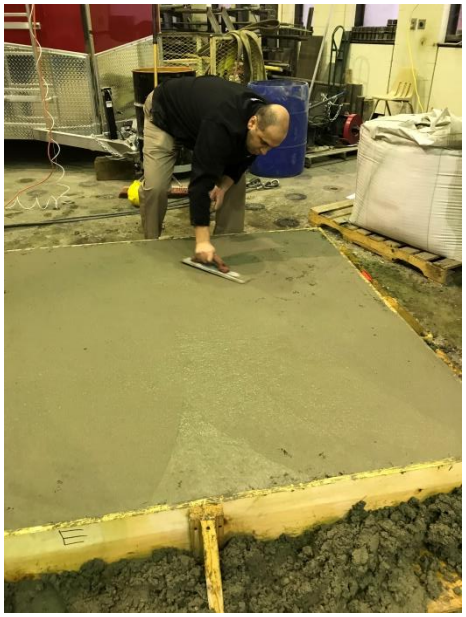

Figure 75: Slab 2 – Slab Finishing

Figure 76: Slab 2 – Void Implantation and Location Measuring

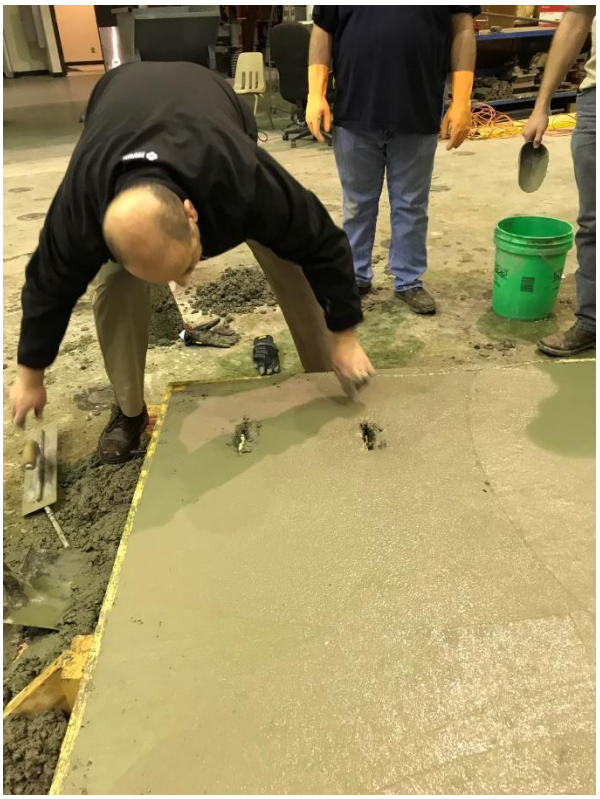

Figure 77: Slab 2 – Oblong Void Implantation

Figure 78: Slab 2 – Oblong Void Location Measurement

Figure 79: Slab 2 – Finished Slab

Figure 80: Slab 2 – Marking of Origin for Measurement Consistency

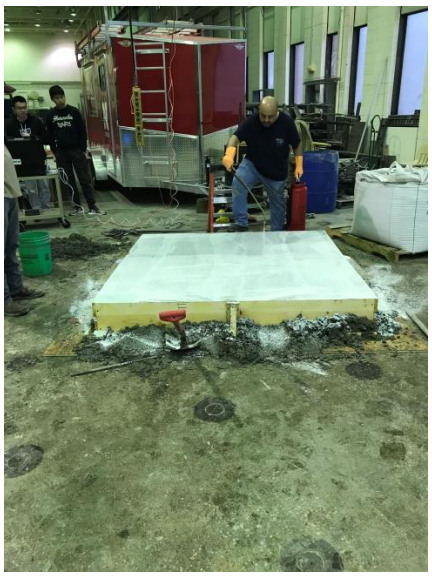

Figure 81: Slab 2 – Curing Compound Spray on Slab

GPR Scans

3 Hours From Production

The following shows the direction of the scan's output for the North-South direction grids and the East-West direction grids presented continuously.

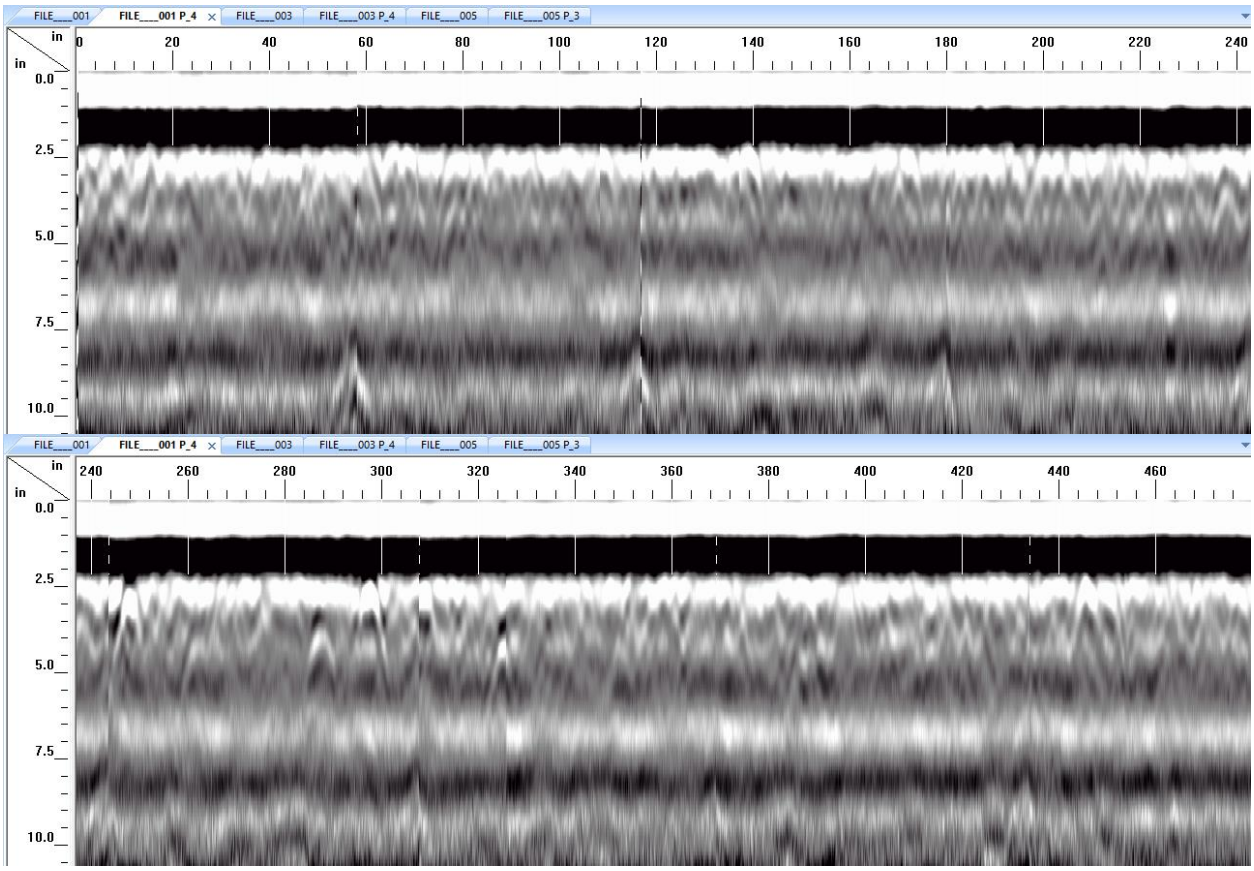
FILE____001
FILE____001 P_4
FILE____003
FILE____003 P_4
FILE____005
FILE____005 P_3
in
in
0
20
40
60
80
100
120
140
160
180
200
220
240
0.0
2.5
5.0
7.5
10.0
FILE____001
FILE____001 P_4
FILE____003
FILE____003 P_4
FILE____005
FILE____005 P_3
in
in
240
260
280
300
320
340
360
380
400
420
440
460
0.0
2.5
5.0
7.5
10.0

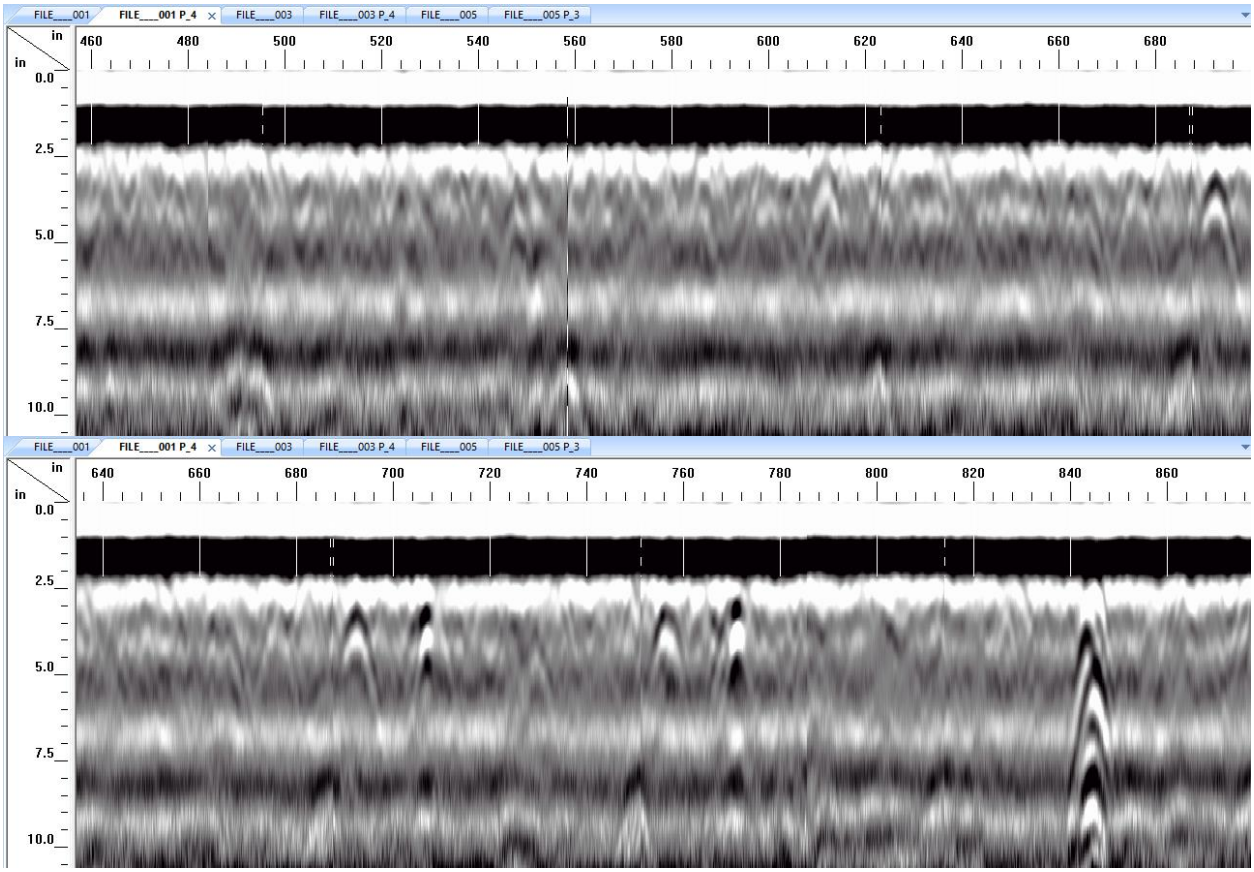

Figure 82: Slab 2 – Continuous Scan Output (North-South Direction)

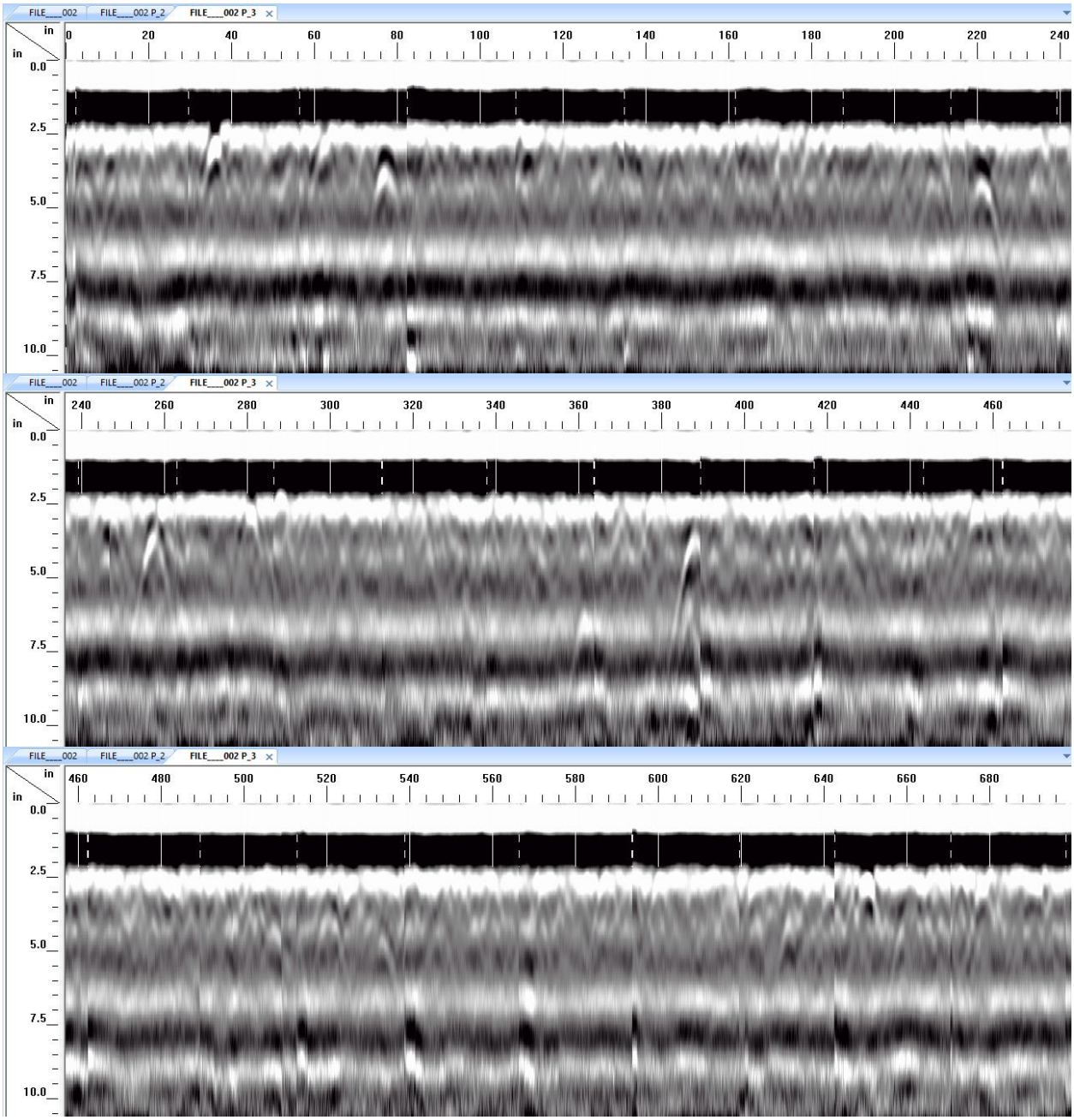
FILE___002
FILE___002 P_2
FILE___002 P_3
in
0 20 40 60 80 100 120 140 160 180 200 220 240
240 260 280 300 320 340 360 380 400 420 440 460
460 480 500 520 540 560 580 600 620 640 660 680
0.0
2.5
5.0
7.5
10.0

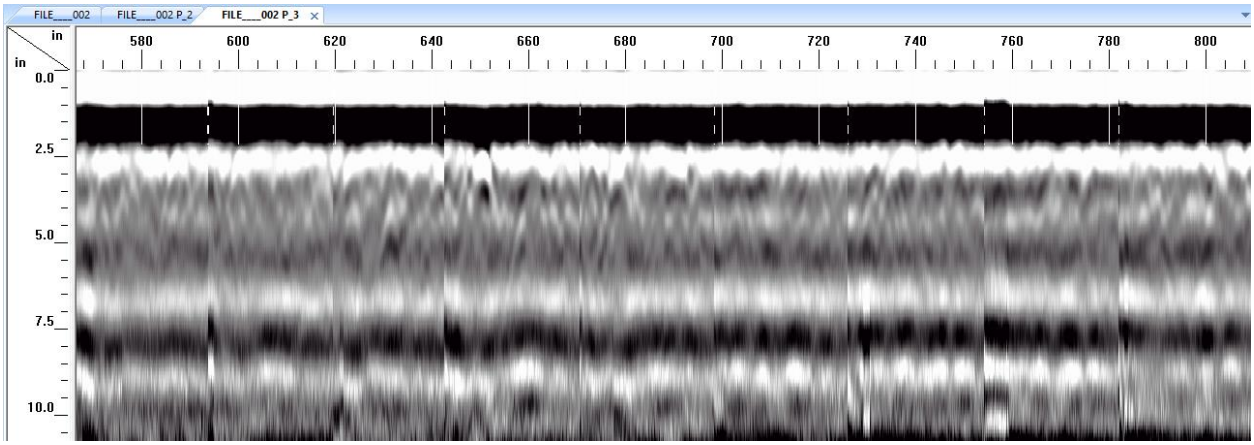

Figure 83: Slab 2 – Continuous Scan Output (East-West Direction)

4 Hours From Production

The following shows the direction of the scan's output for the North-South direction grids and the East-West direction grids presented continuously.

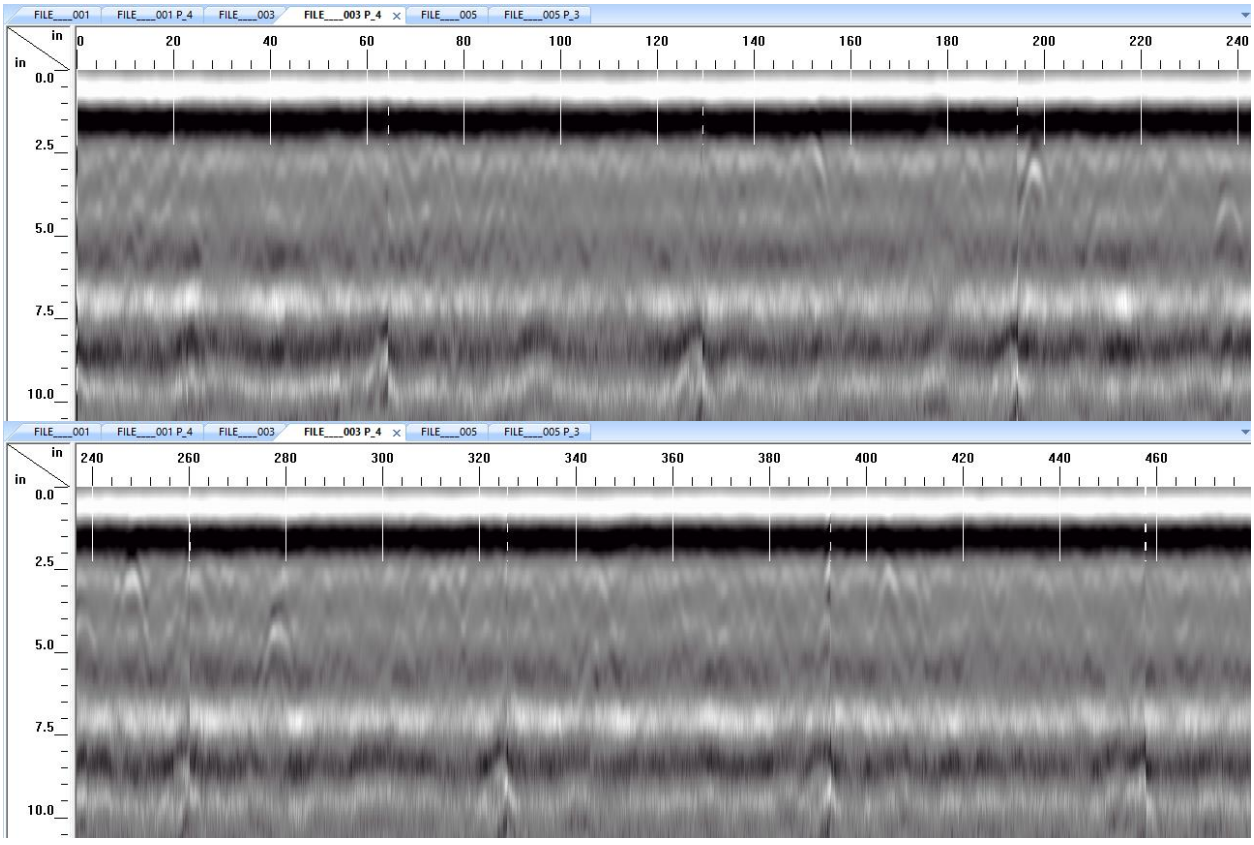

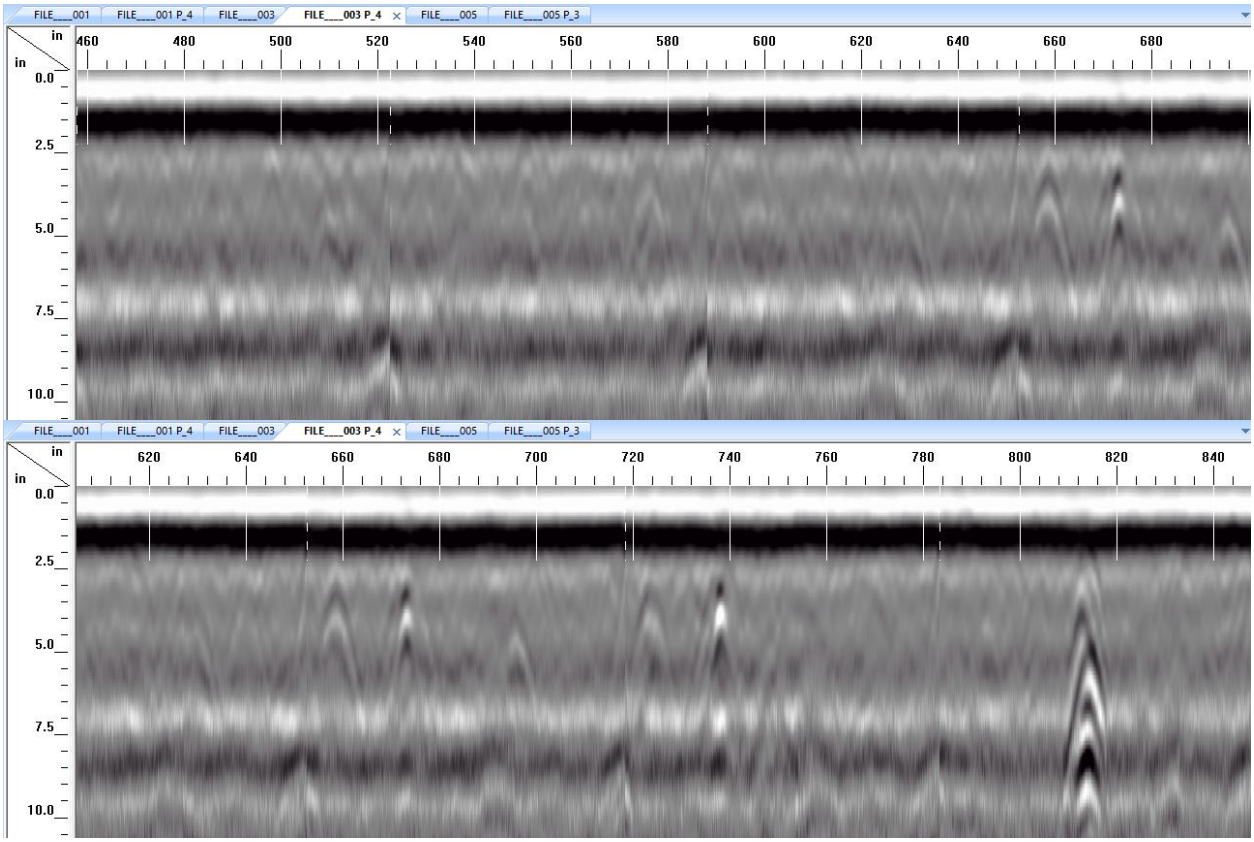

Figure 84: Slab 2 – Continuous Scan Output (North-South Direction)

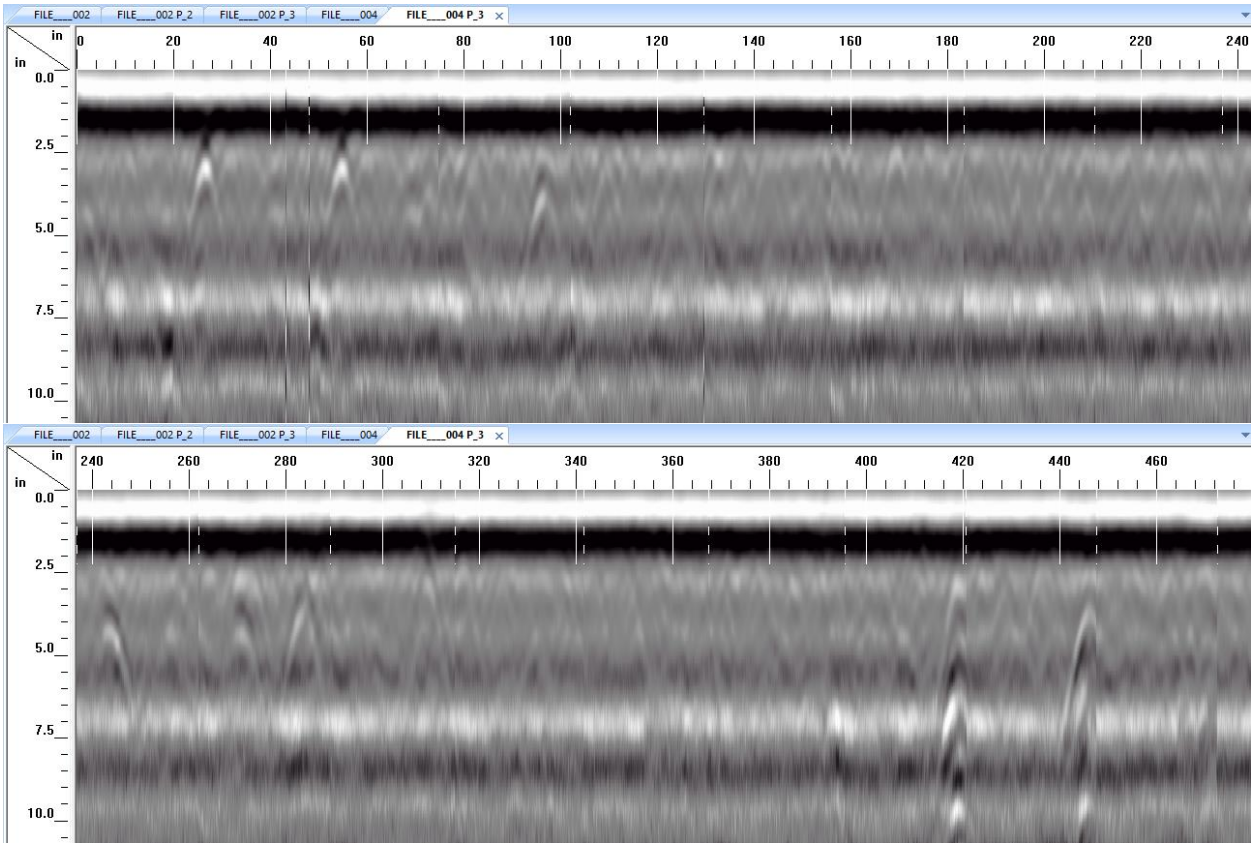
FILE___002
FILE___002 P_2
FILE___002 P_3
FILE___004
FILE___004 P_3
in
0
20
40
60
80
100
120
140
160
180
200
220
240
0.0
2.5
5.0
7.5
10.0
FILE___002
FILE___002 P_2
FILE___002 P_3
FILE___004
FILE___004 P_3
in
240
260
280
300
320
340
360
380
400
420
440
460
0.0
2.5
5.0
7.5
10.0

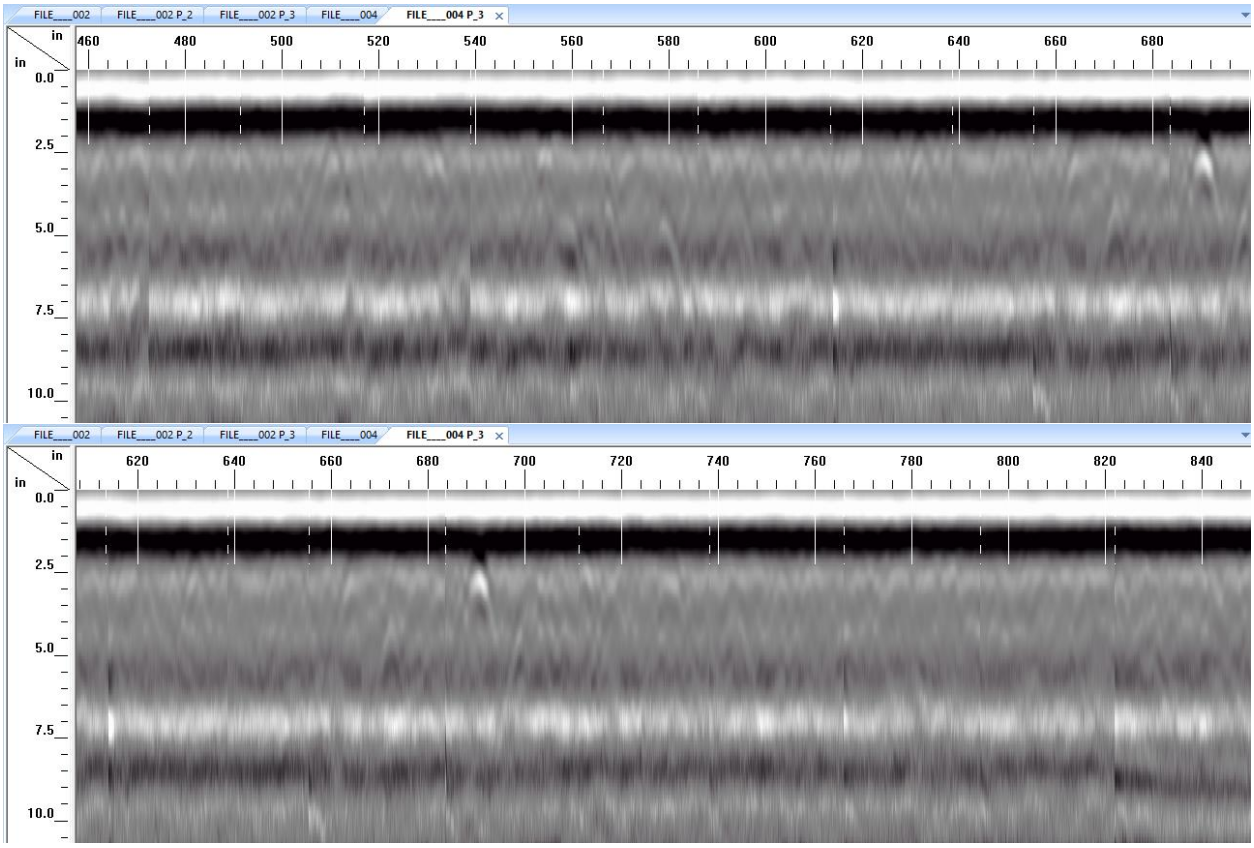

Figure 85: Slab 2 – Continuous Scan Output (East-West Direction)

24 Hours From Production

The following shows the direction of the scan's output for the North-South direction grids and the East-West direction grids presented continuously.

North-South

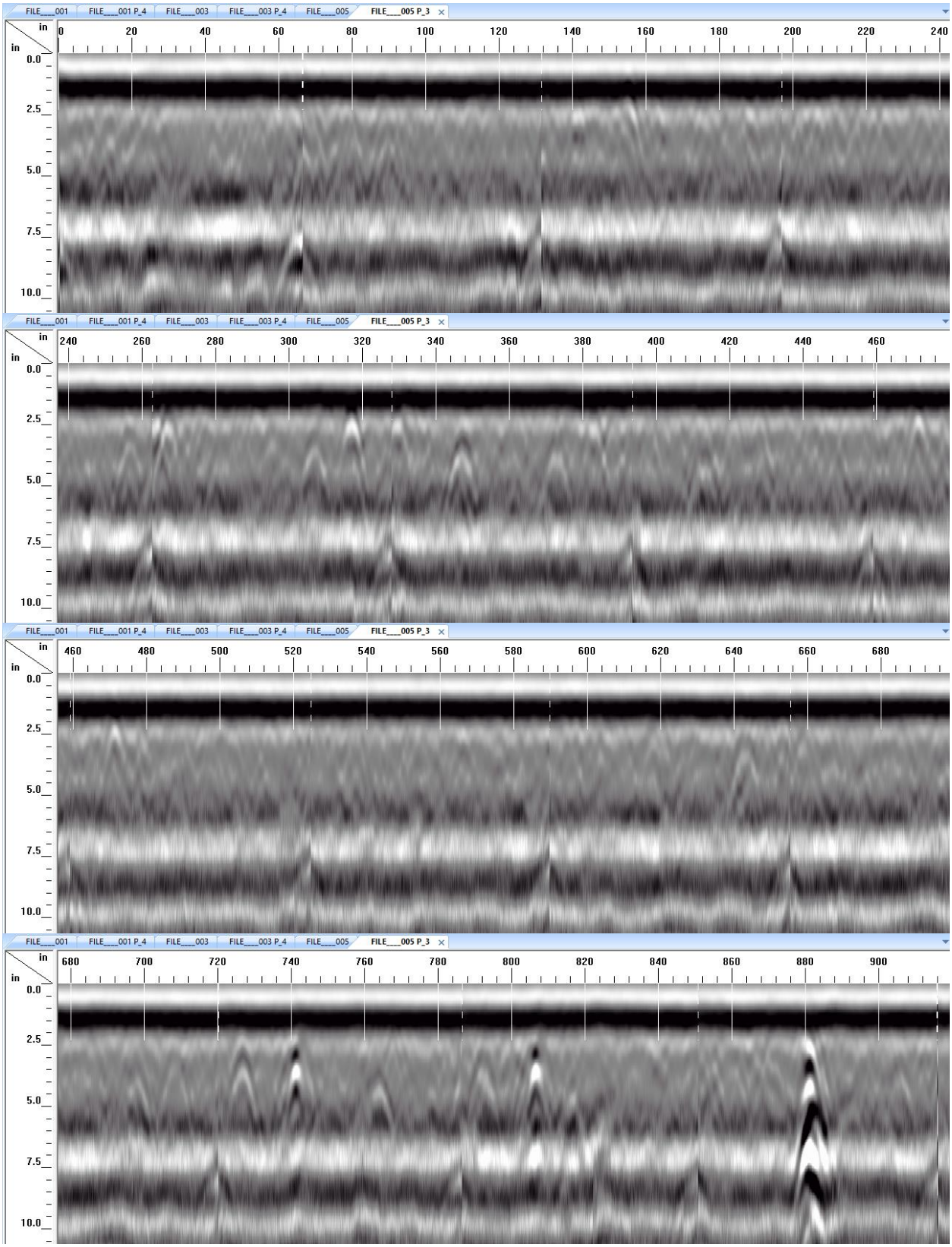
FILE___001
FILE___001 P_4
FILE___003
FILE___003 P_4
FILE___005
FILE___005 P_3
in
0 20 40 60 80 100 120 140 160 180 200 220 240
240 260 280 300 320 340 360 380 400 420 440 460
460 480 500 520 540 560 580 600 620 640 660 680
680 700 720 740 760 780 800 820 840 860 880 900
0.0
2.5
5.0
7.5
10.0

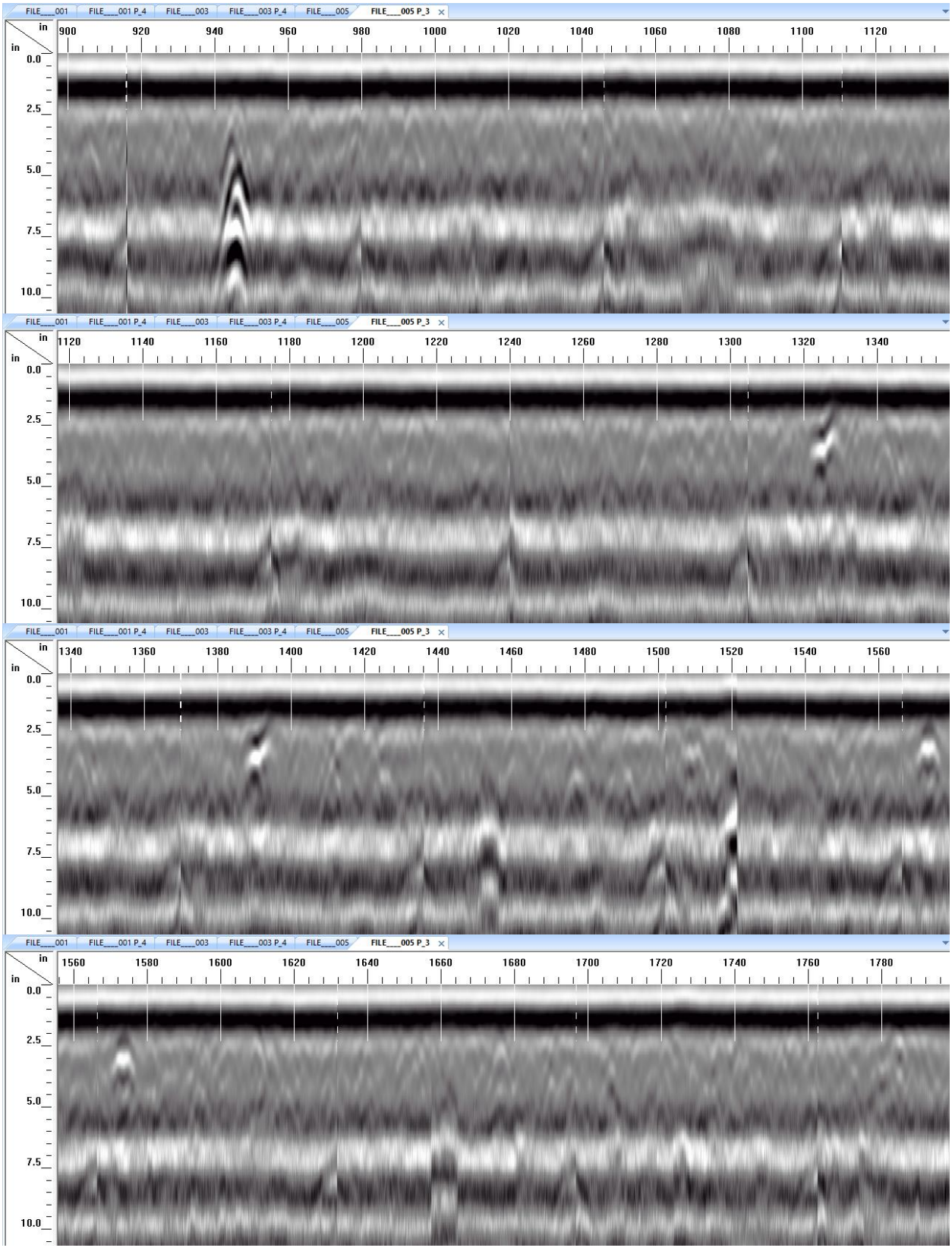
FILE___001
FILE___001 P_4
FILE___003
FILE___003 P_4
FILE___005
FILE___005 P_3
in
900 920 940 960 980 1000 1020 1040 1060 1080 1100 1120
1120 1140 1160 1180 1200 1220 1240 1260 1280 1300 1320 1340
1340 1360 1380 1400 1420 1440 1460 1480 1500 1520 1540 1560
1560 1580 1600 1620 1640 1660 1680 1700 1720 1740 1760 1780
0.0
2.5
5.0
7.5
10.0

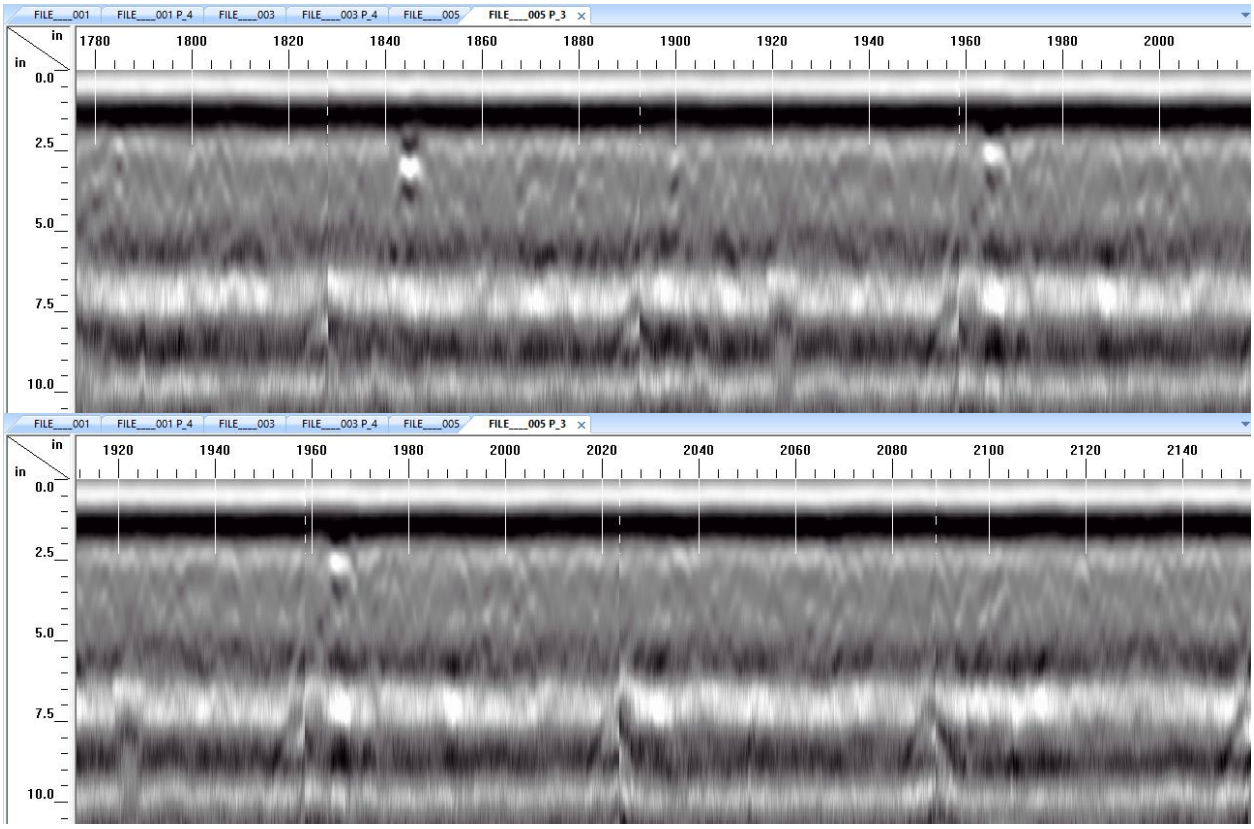

Figure 86: Slab 2 – Continuous Output Scans (North-South Direction)

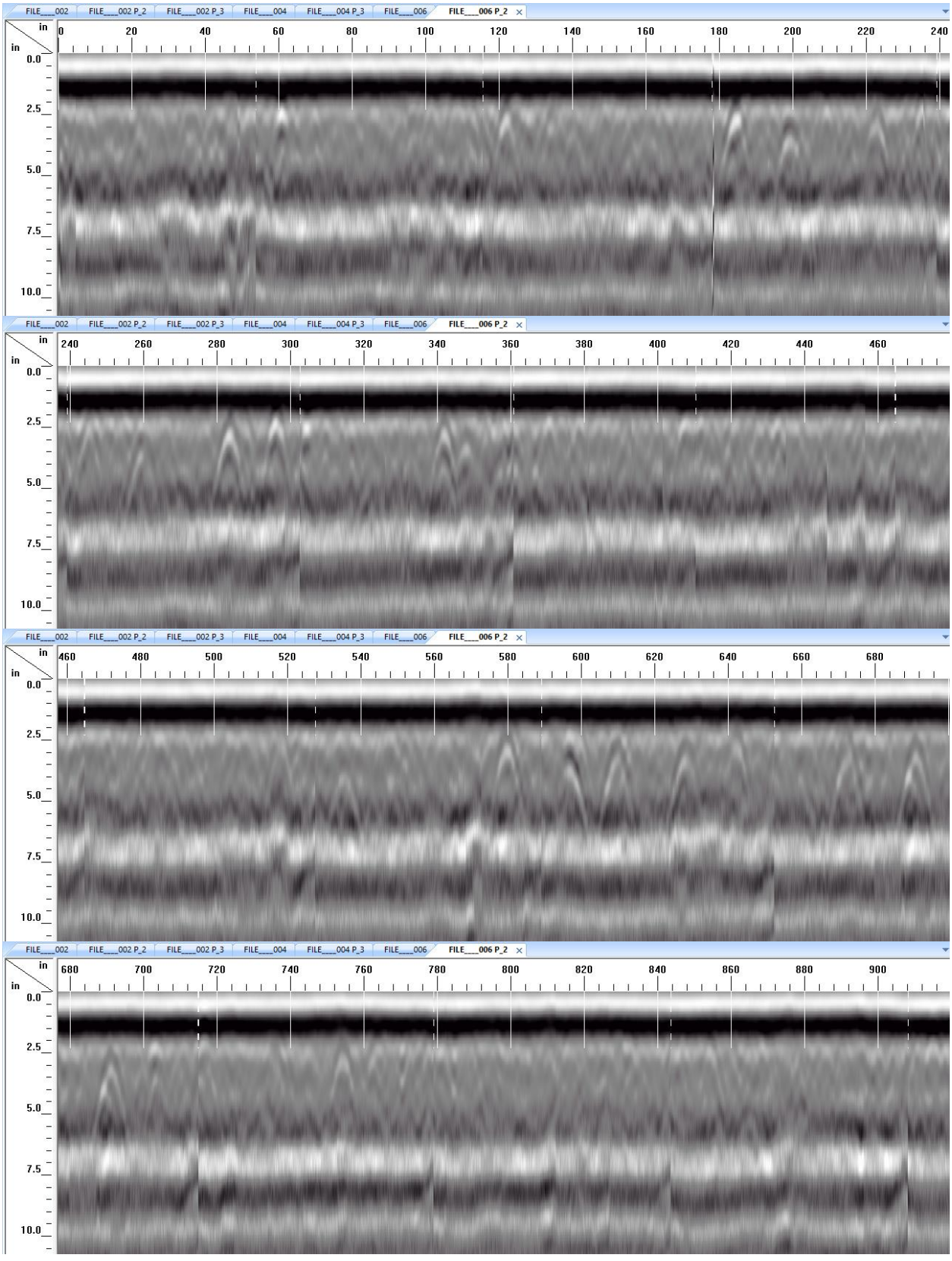
FILE___002
FILE___002 P_2
FILE___002 P_3
FILE___004
FILE___004 P_3
FILE___006
FILE___006 P_2
in
0 20 40 60 80 100 120 140 160 180 200 220 240
240 260 280 300 320 340 360 380 400 420 440 460
460 480 500 520 540 560 580 600 620 640 660 680
680 700 720 740 760 780 800 820 840 860 880 900
0.0
2.5
5.0
7.5
10.0

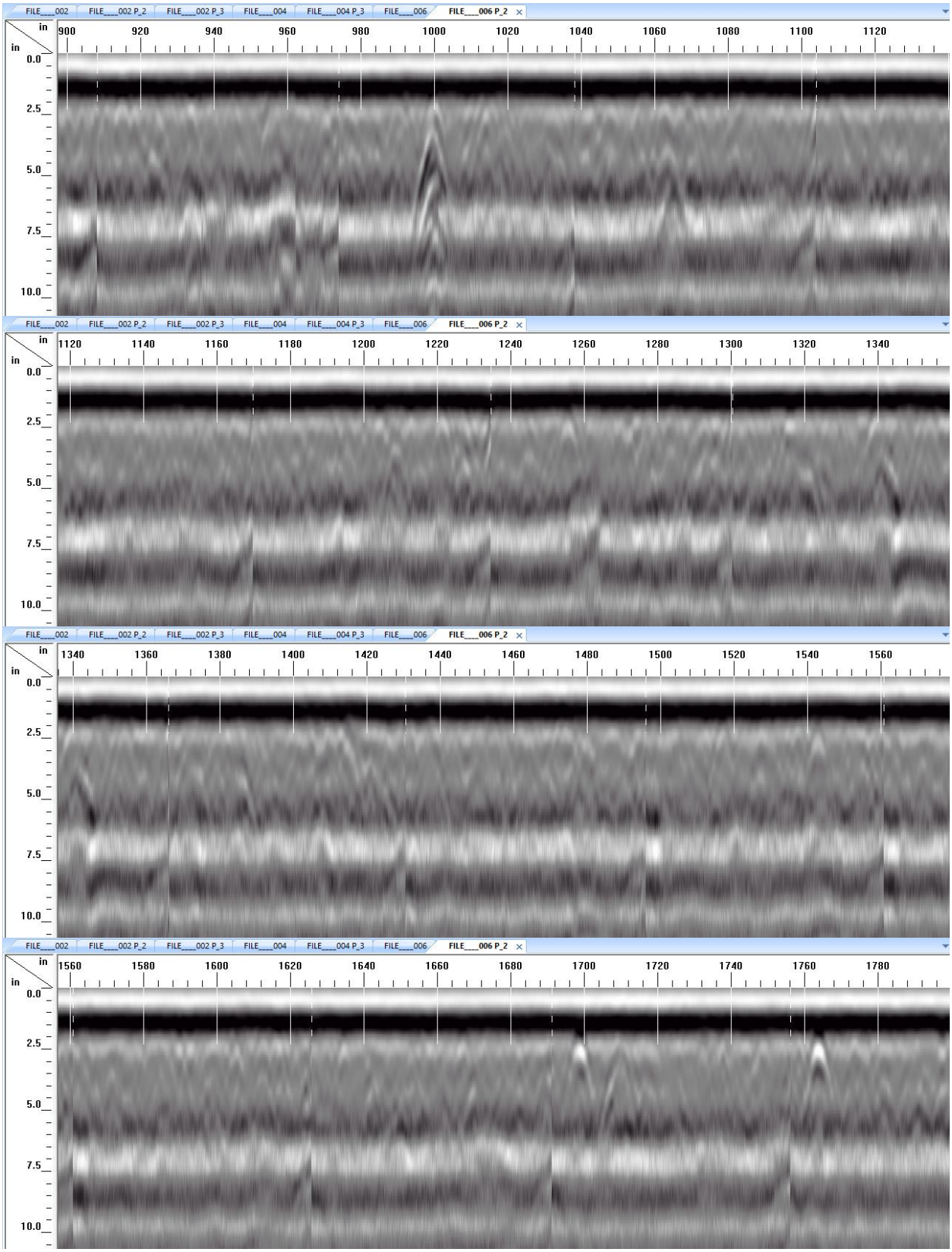
FILE___002
FILE___002 P_2
FILE___002 P_3
FILE___004
FILE___004 P_3
FILE___006
FILE___006 P_2
in
0.0
2.5
5.0
7.5
10.0
900 920 940 960 980 1000 1020 1040 1060 1080 1100 1120
1120 1140 1160 1180 1200 1220 1240 1260 1280 1300 1320 1340
1340 1360 1380 1400 1420 1440 1460 1480 1500 1520 1540 1560
1560 1580 1600 1620 1640 1660 1680 1700 1720 1740 1760 1780

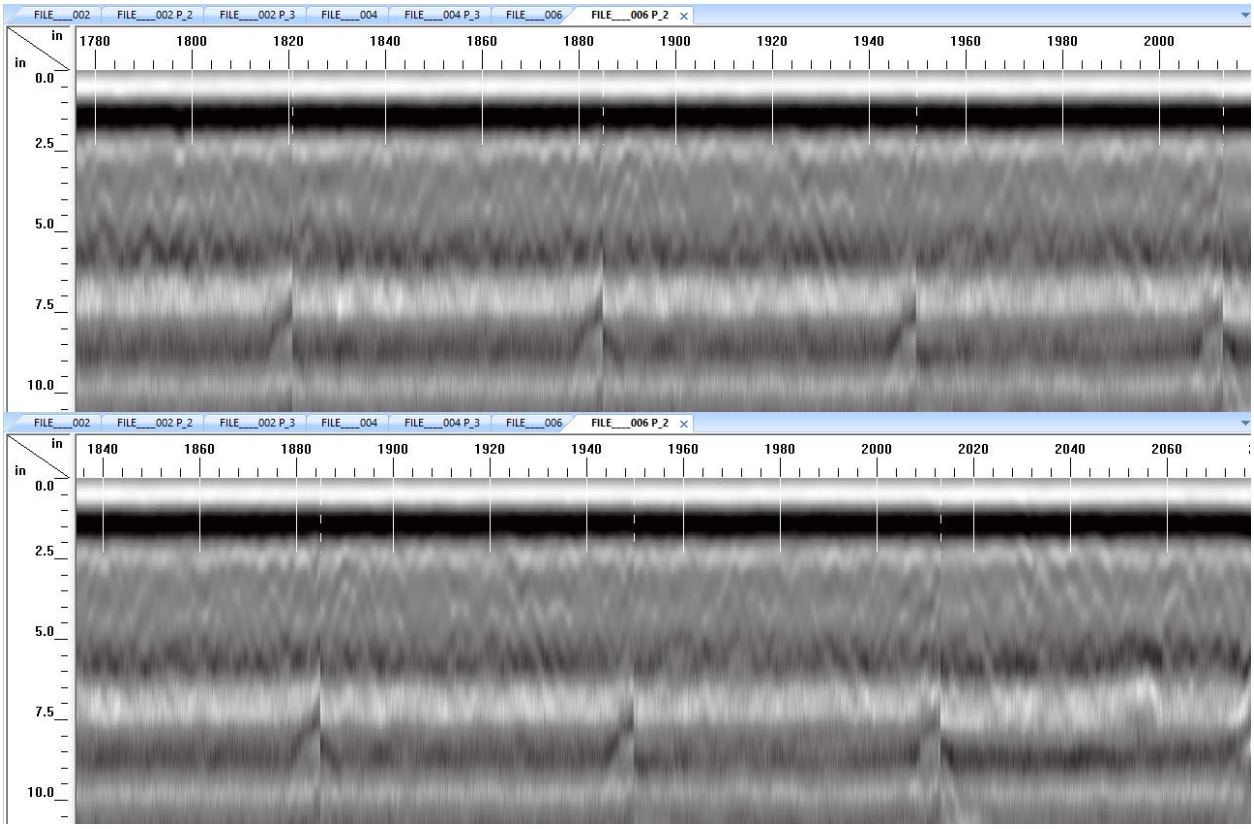

Figure 87: Slab 2 – Continuous Output Scans (East-West Direction)

Coring Photos

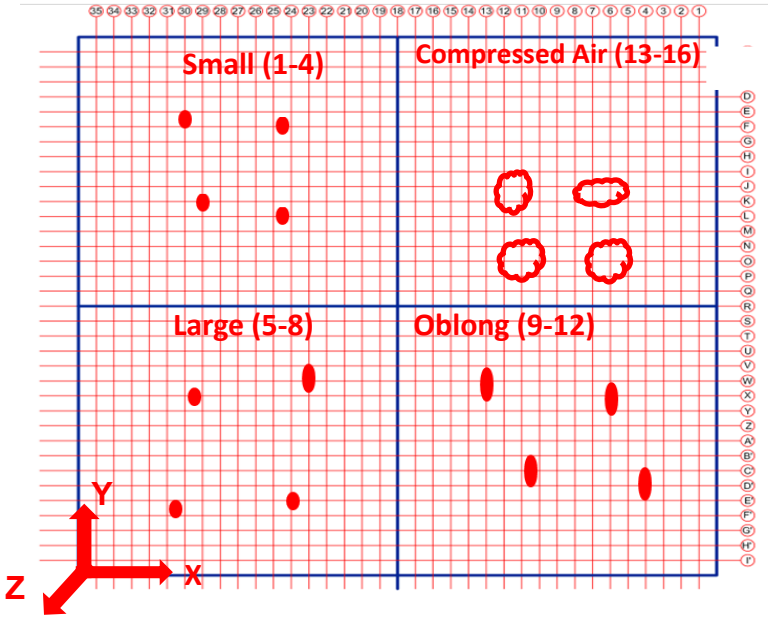

Figure 88: Slab 2 – Void Location and Scanning Coordinate System

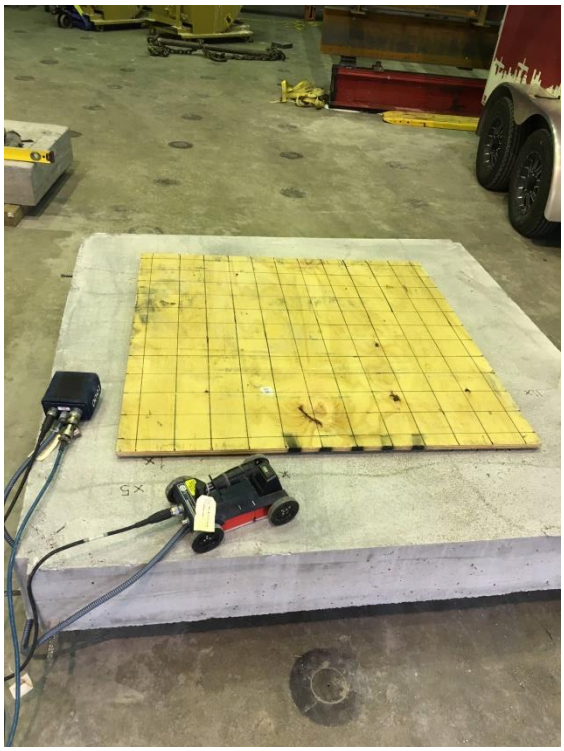

Figure 89: Slab 2 – Elevated Plywood Grid for Scanning

Figure 90: Slab 2 – Coring Equipment and Setup Outside of the Lab

Figure 91: Slab 2 – Tracks Left on Curing Compound From GPR Wheels

Figure 92: Slab 2 – Coring Locations on Slab Surface

Figure 93: Slab 2 – Core 8 (Large Artificial Void)

Figure 94: Slab 2 – Core 12 (Oblong Artificial Void)

Figure 95: Slab 2 – Core 13 (Compressed Air)

Slab 3

Casting Photos

Figure 96: Slab 3 – Formwork Depth Measurement

Figure 97: Slab 3 - Prepared Formwork and Steel Plate

Figure 98: Slab 3 – Mix Preparation

Figure 99: Slab 3 - Hand Pouring of the Slab

Figure 100: Slab 3 – Finished Slab

GPR Scans

Hour 1.5

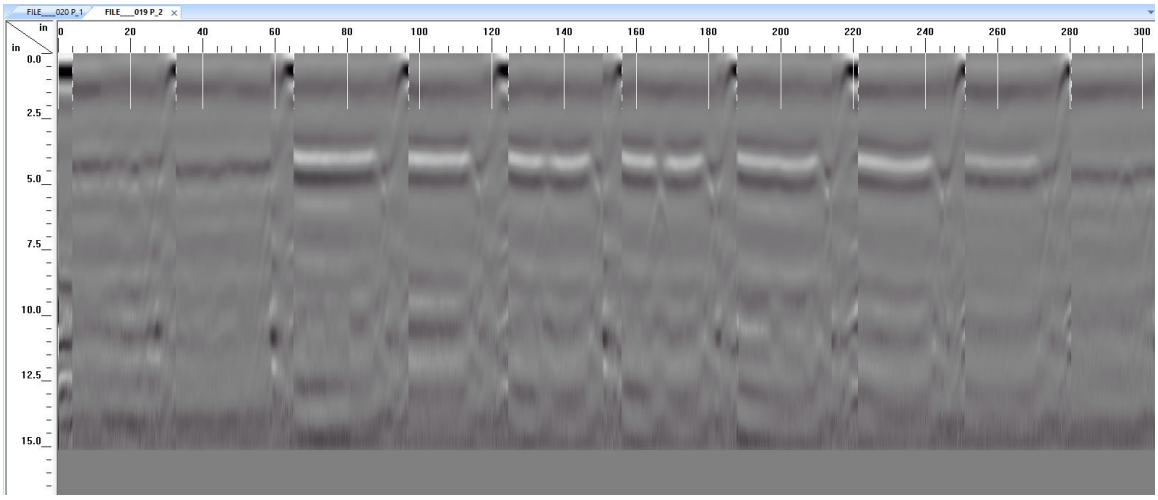

Figure 101: Slab 3 – Hour 1.5 Scan Outputs (X-Direction)

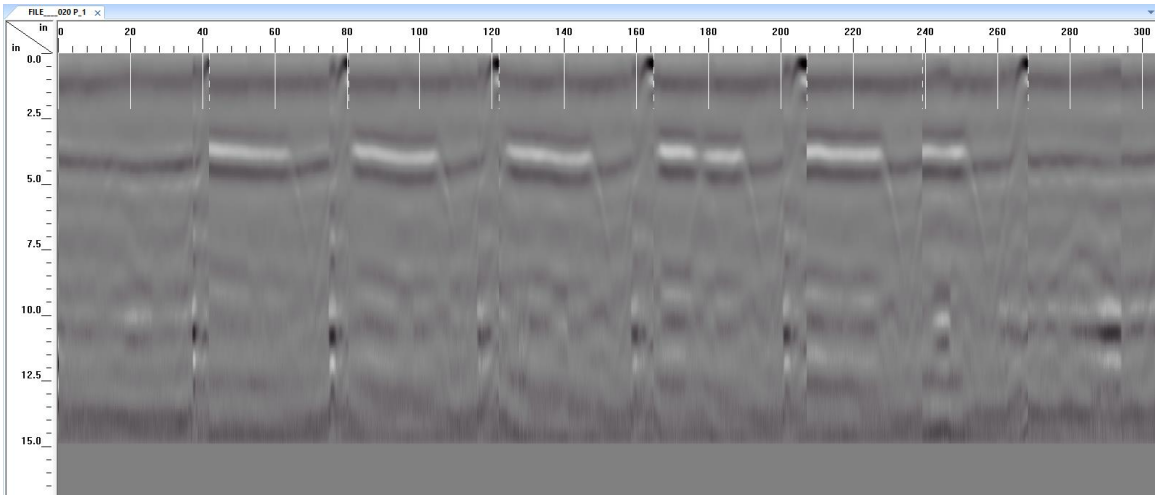

Figure 102: Slab 3 – Hour 1.5 Scan Outputs (Y-Direction)

Hour 2.5

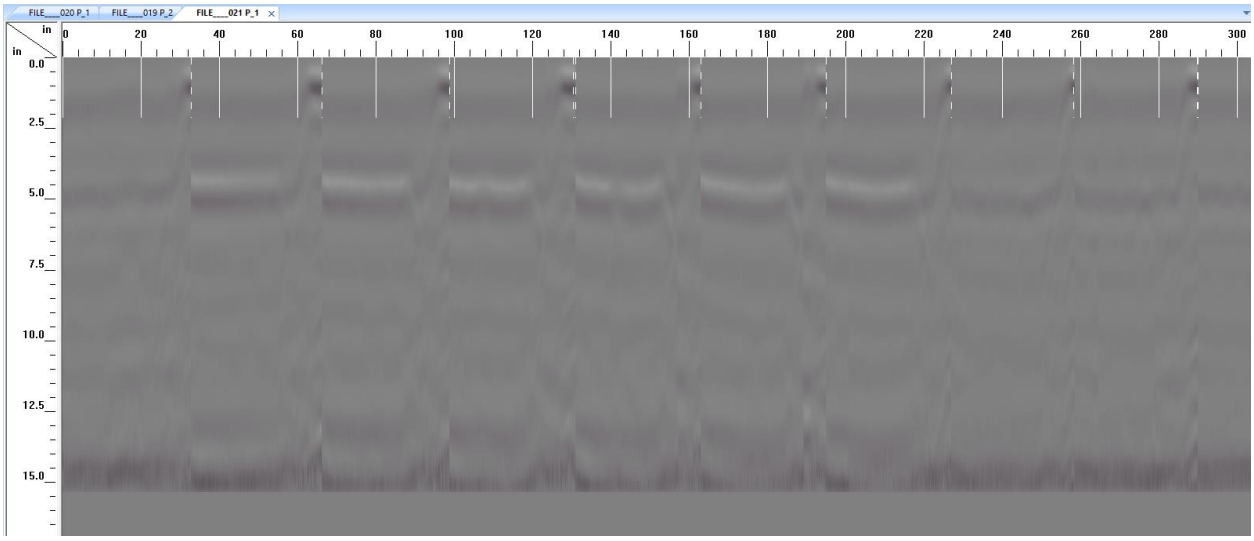

Figure 103: Slab 3 – Hour 2.5 Scan Outputs (X-Direction)

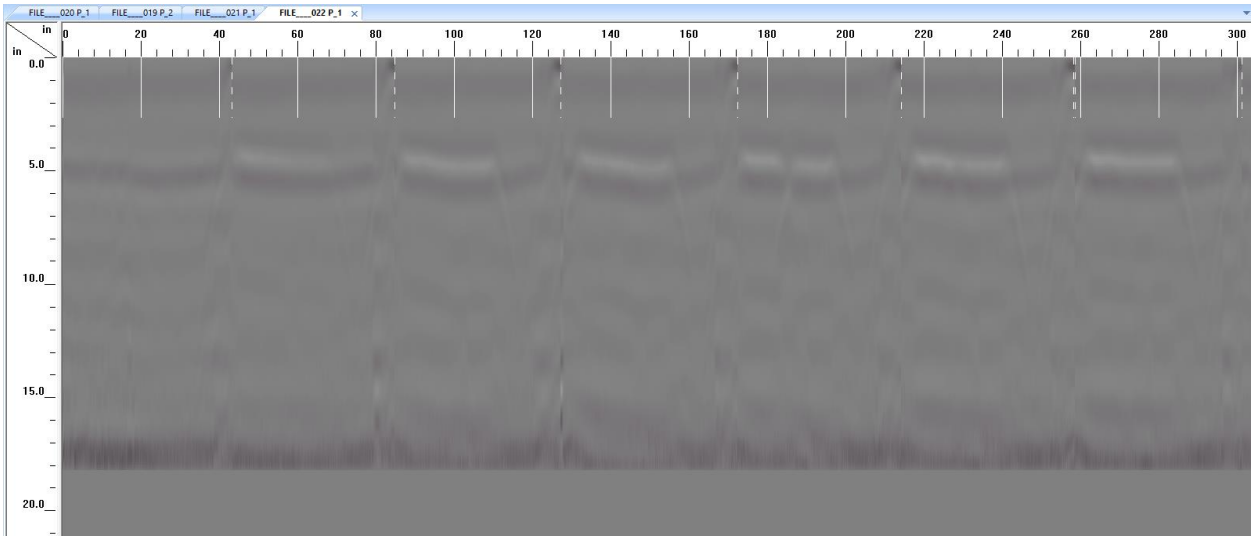

Figure 104: Slab 3 – Hour 2.5 Scan Outputs (Y-Direction)

Hour 3.5

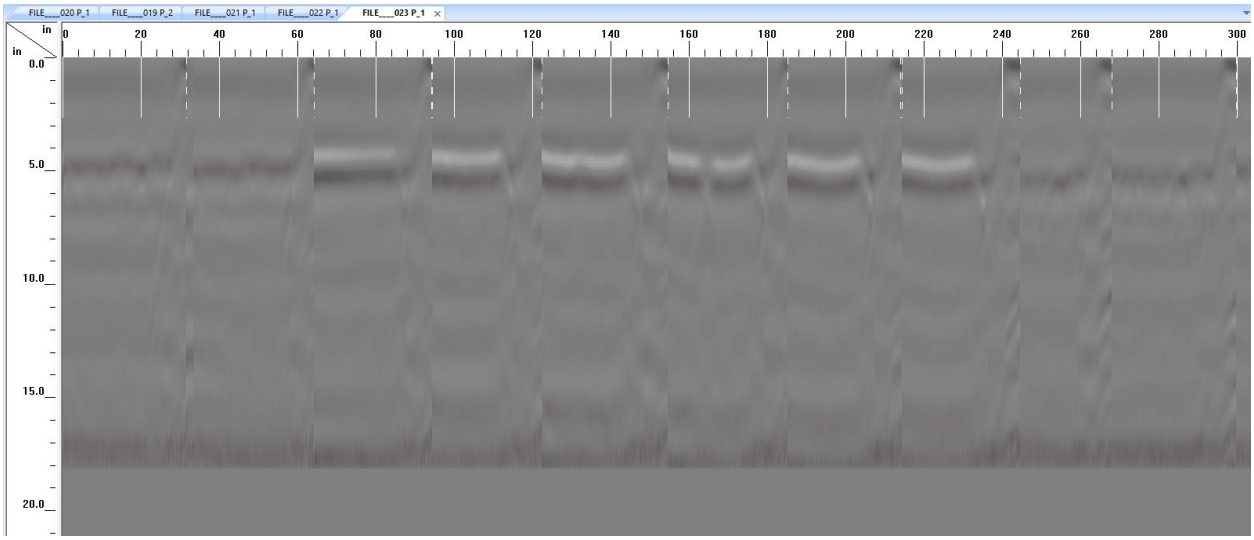

Figure 105: Slab 3 – Hour 3.5 Scan Outputs (X-Direction)

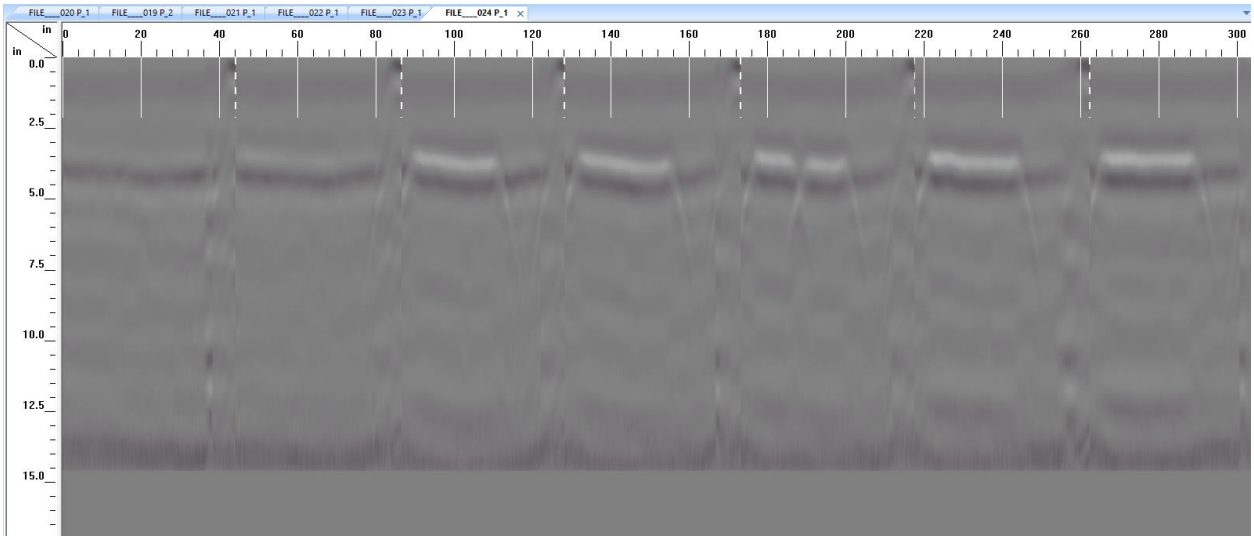

Figure 106: Slab 3 – Hour 3.5 Scan Outputs (Y-Direction)

Hour 4.5

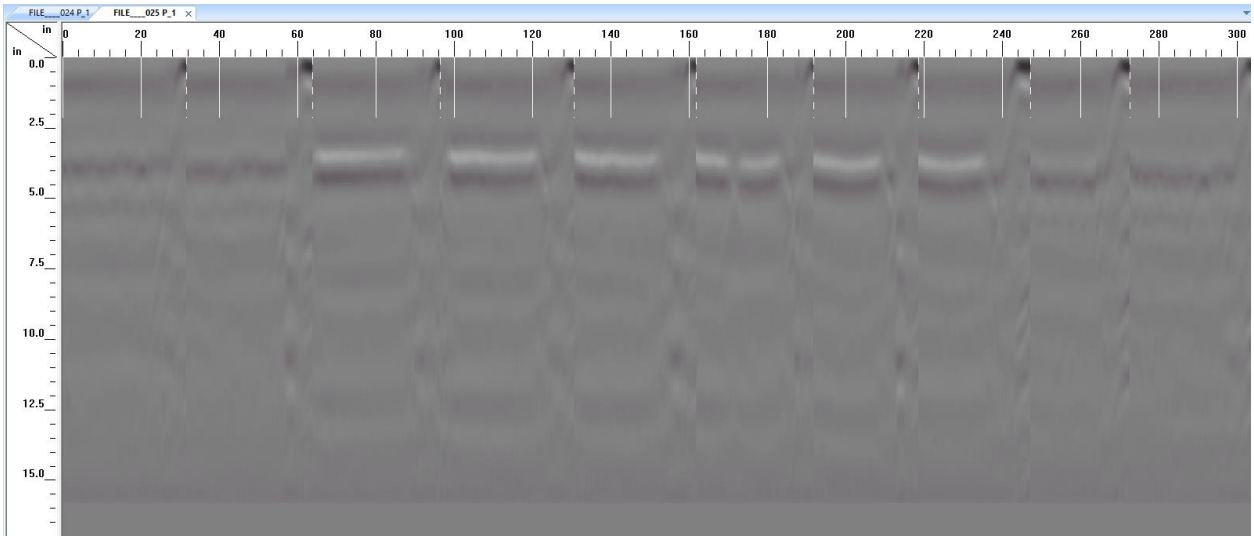

Figure 107: Slab 3 – Hour 4.5 Scan Outputs (X-Direction)

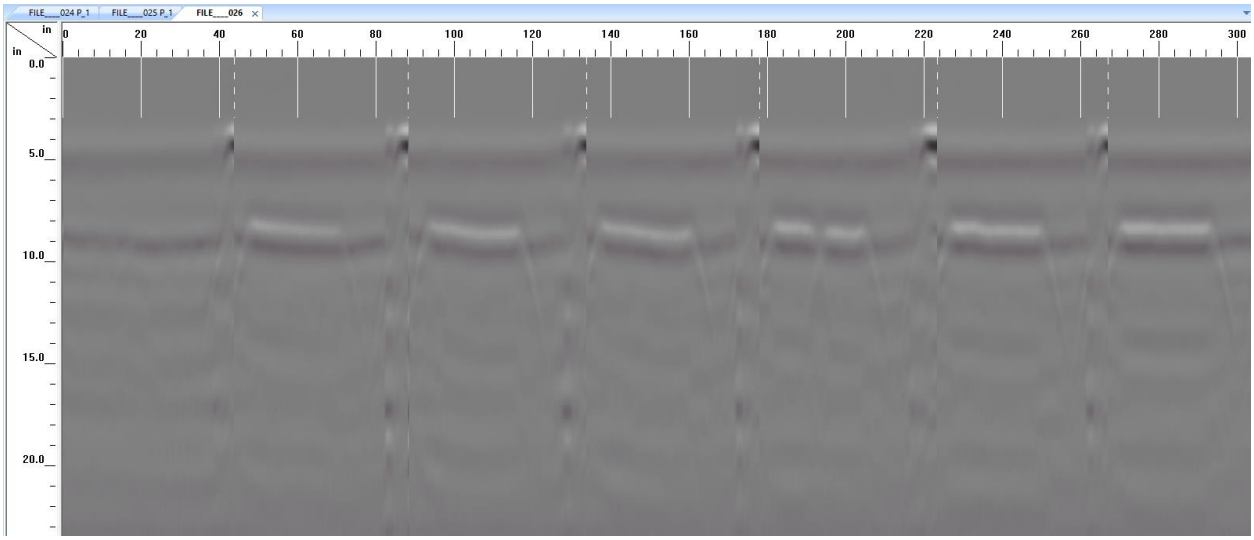

Figure 108: Slab 3 – Hour 4.5 Scan Outputs (Y-Direction)

Hour 5.5

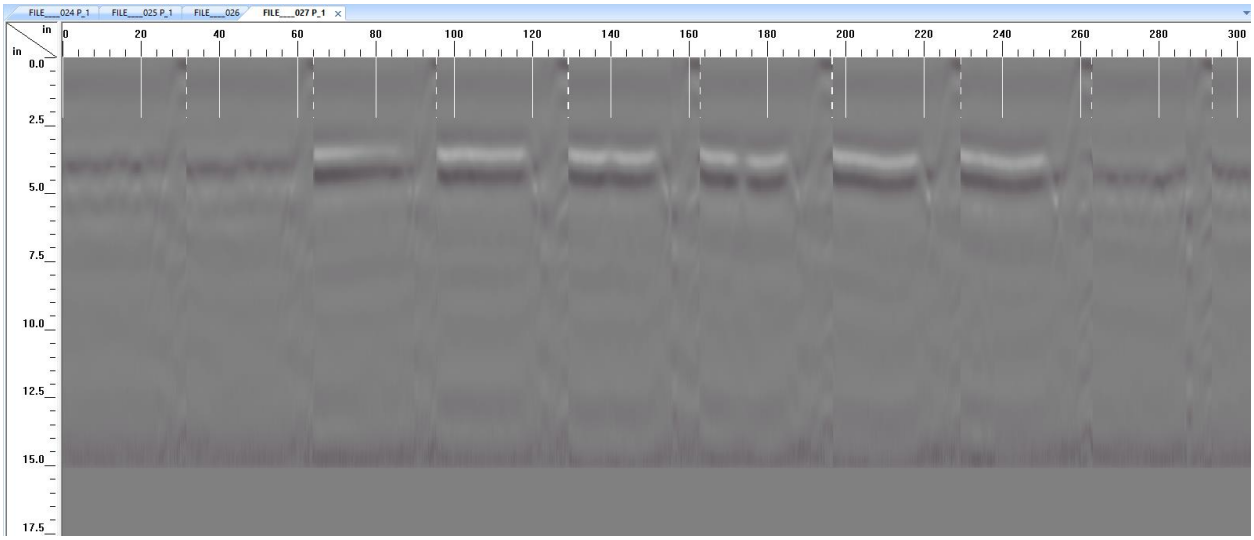

Figure 109: Slab 3 – Hour 5.5 Scan Outputs (X-Direction)

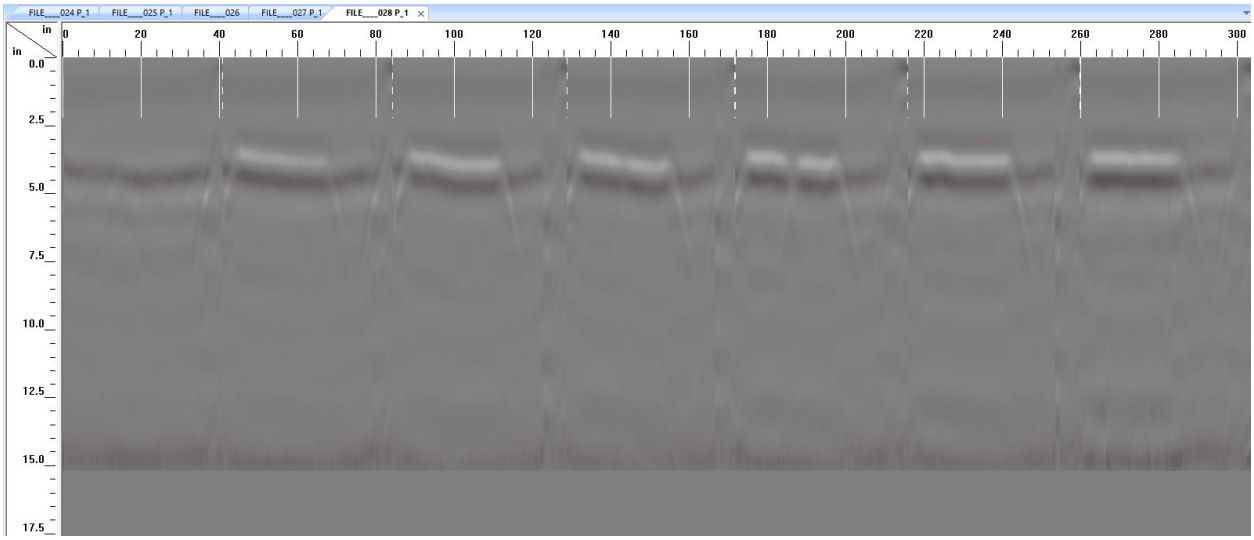

Figure 110: Slab 3 – Hour 5.5 Scan Outputs (Y-Direction)

Hour 6.5

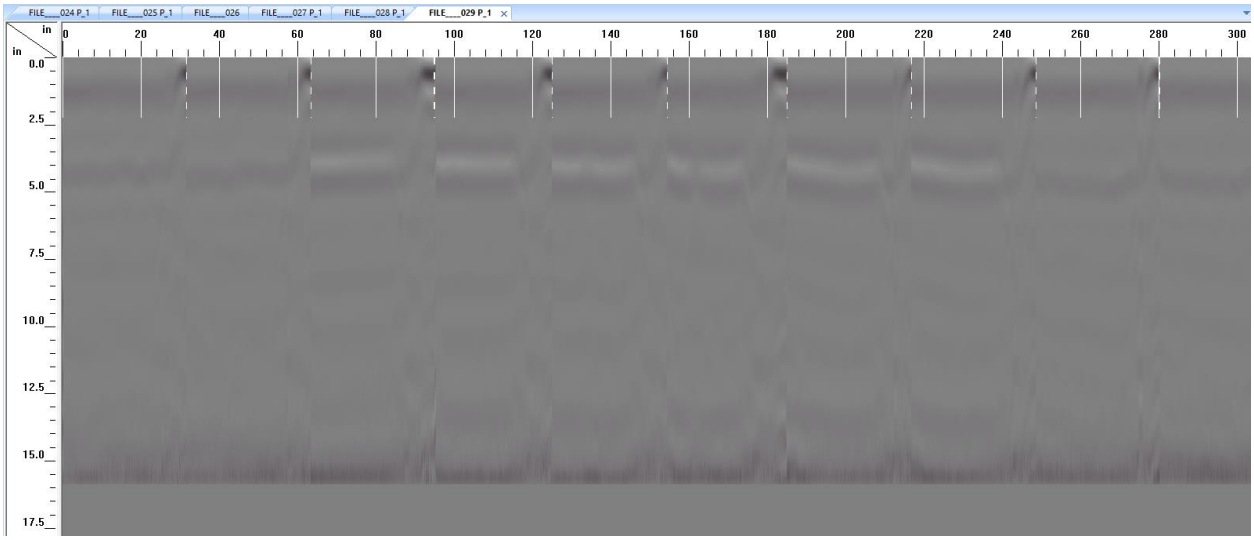

Figure 111: Slab 3 – Hour 6.5 Scan Outputs (X-Direction)

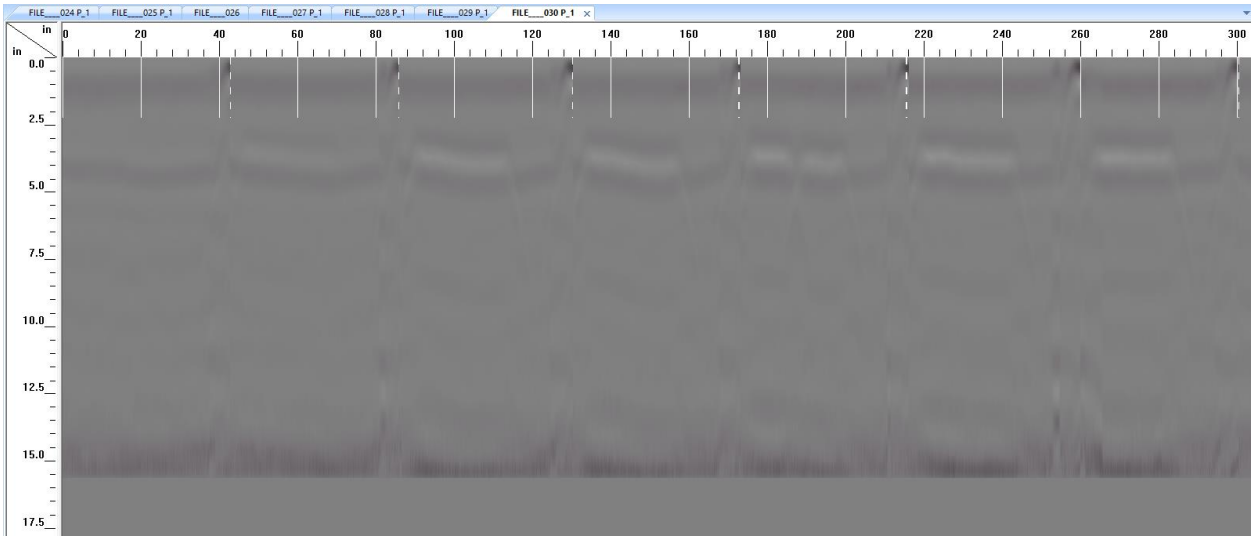

Figure 112: Slab 3 – Hour 6.5 Scan Outputs (Y-Direction)

Hour 7.5

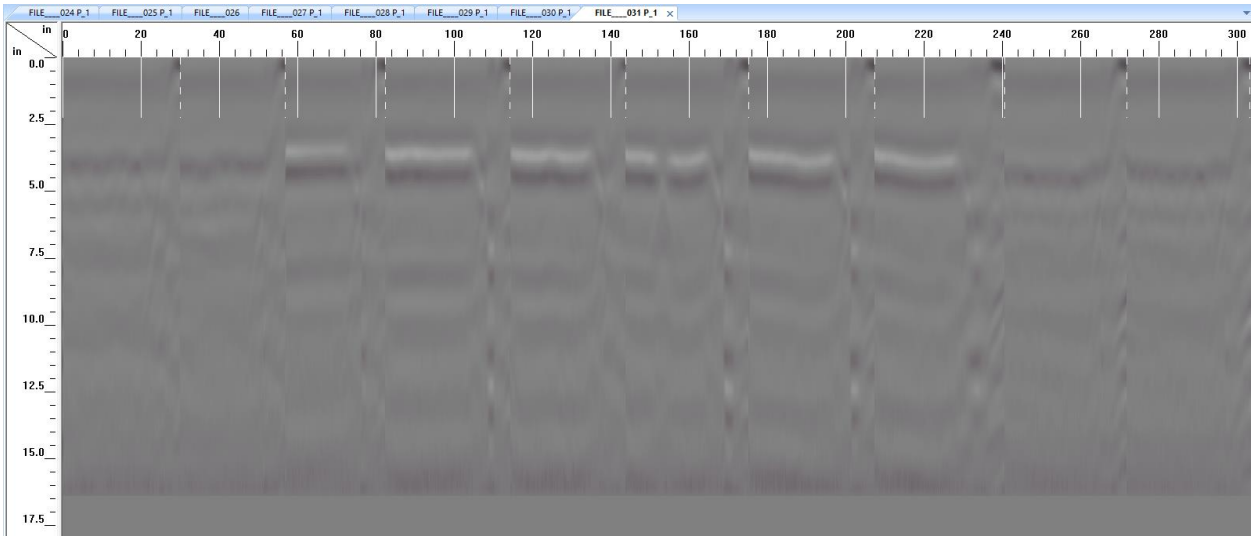

Figure 113: Slab 3 – Hour 7.5 Scan Outputs (X-Direction)

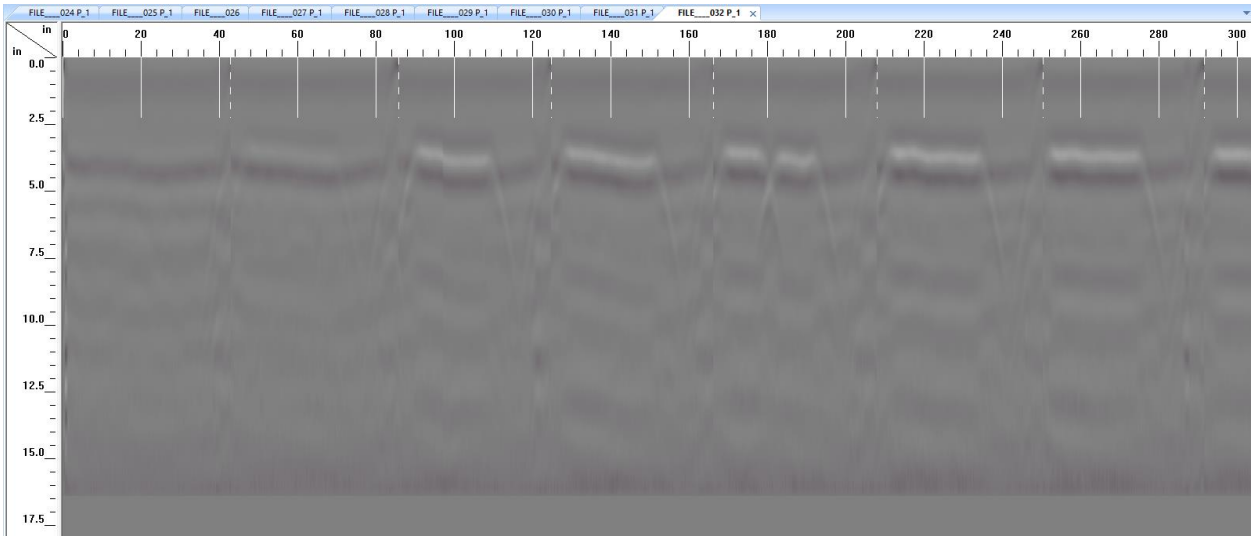

Figure 114: Slab 3 – Hour 7.5 Scan Outputs (Y-Direction)

Hour 8.5

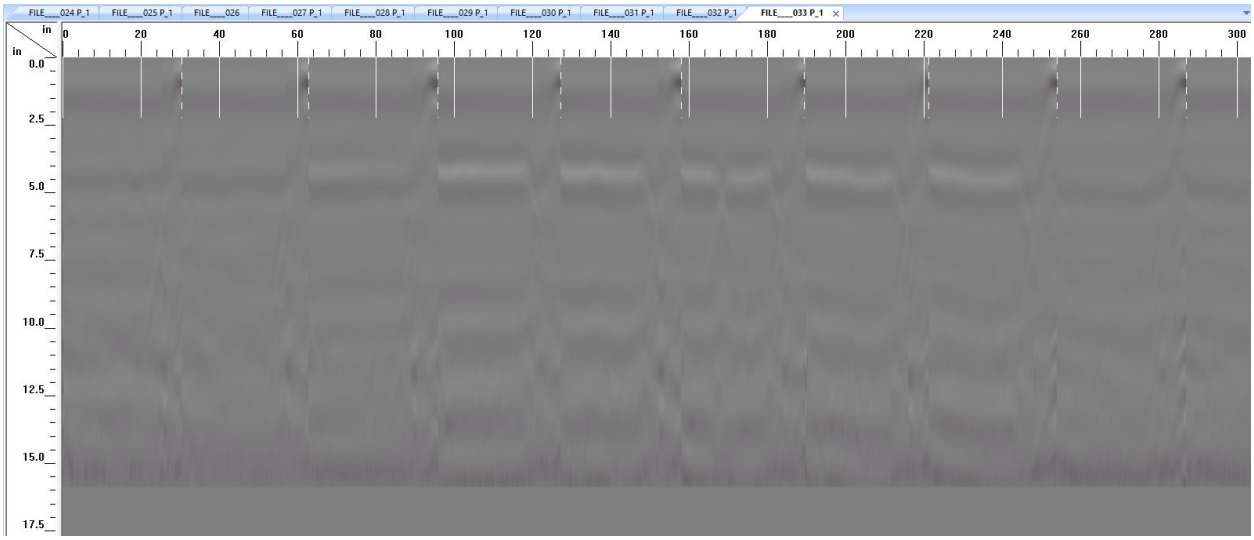

Figure 115: Slab 3 – Hour 8.5 Scan Outputs (X-Direction)

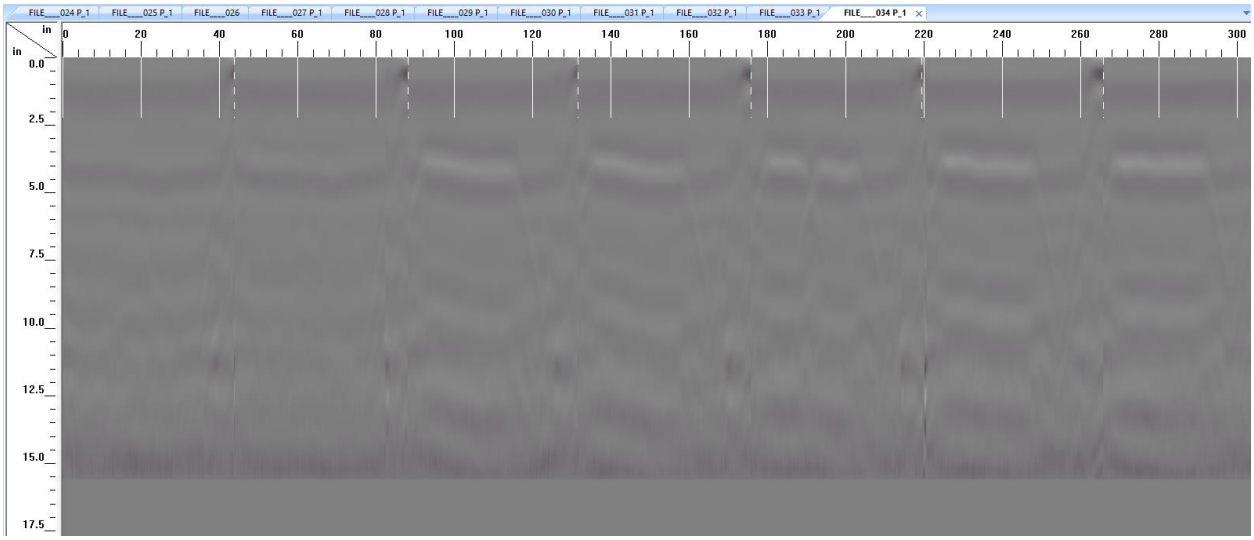

Figure 116: Slab 3 – Hour 8.5 Scan Outputs (Y-Direction)

Hour 9.5

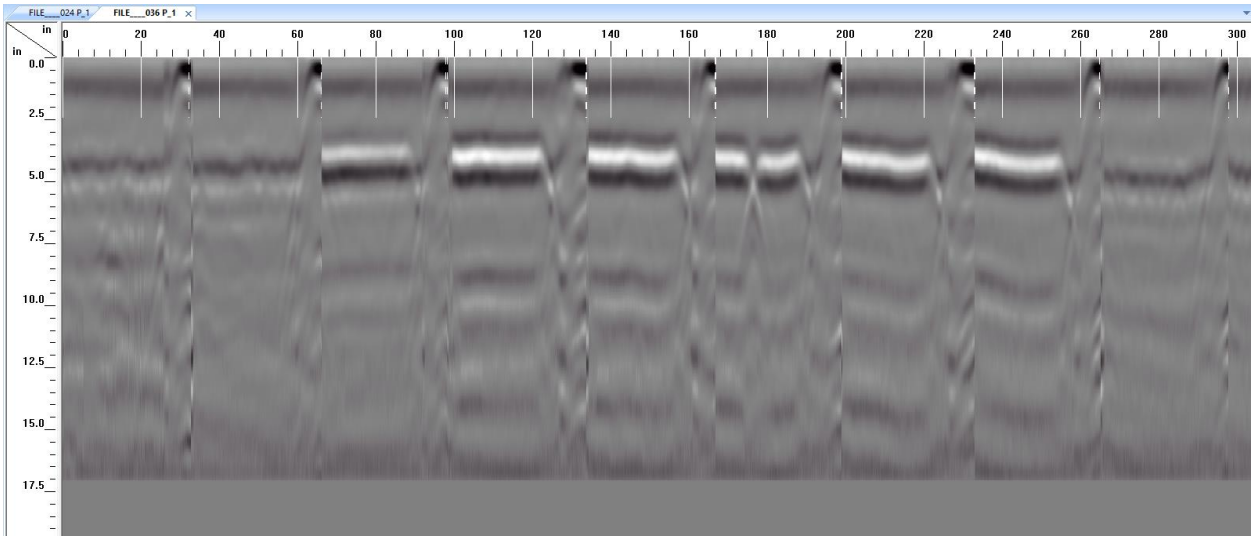

Figure 117: Slab 3 – Hour 9.5 Scan Outputs (X-Direction)

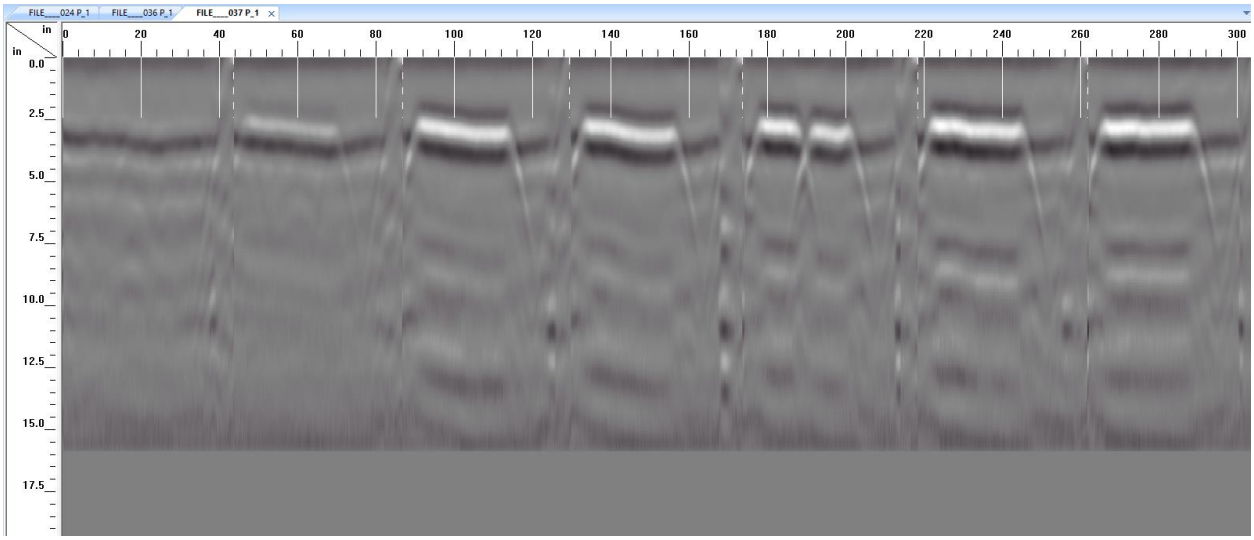

Figure 118: Slab 3 – Hour 9.5 Scan Outputs (Y-Direction)

Hour 10.5

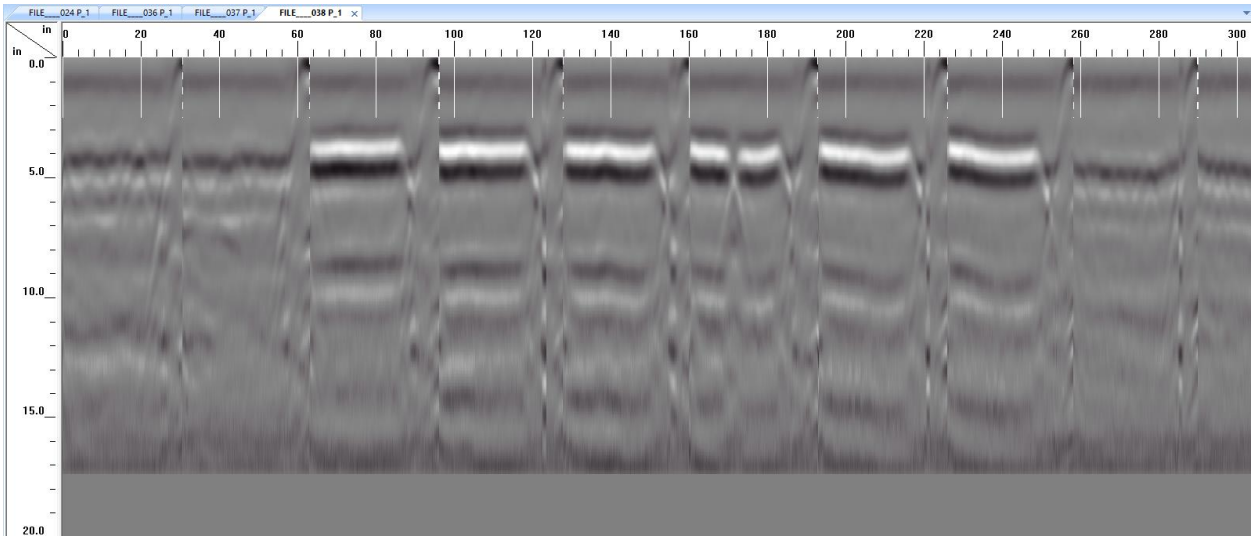

Figure 119: Slab 3 – Hour 10.5 Scan Outputs (X-Direction)

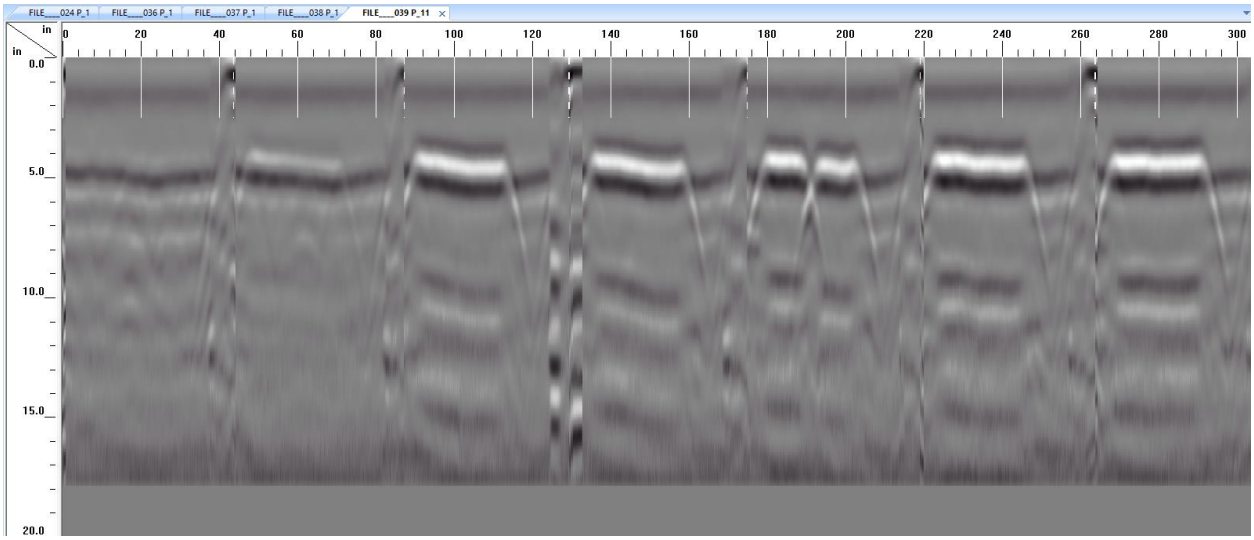

Figure 120: Slab 3 – Hour 10.5 Scan Outputs (Y-Direction)

Hour 11.5

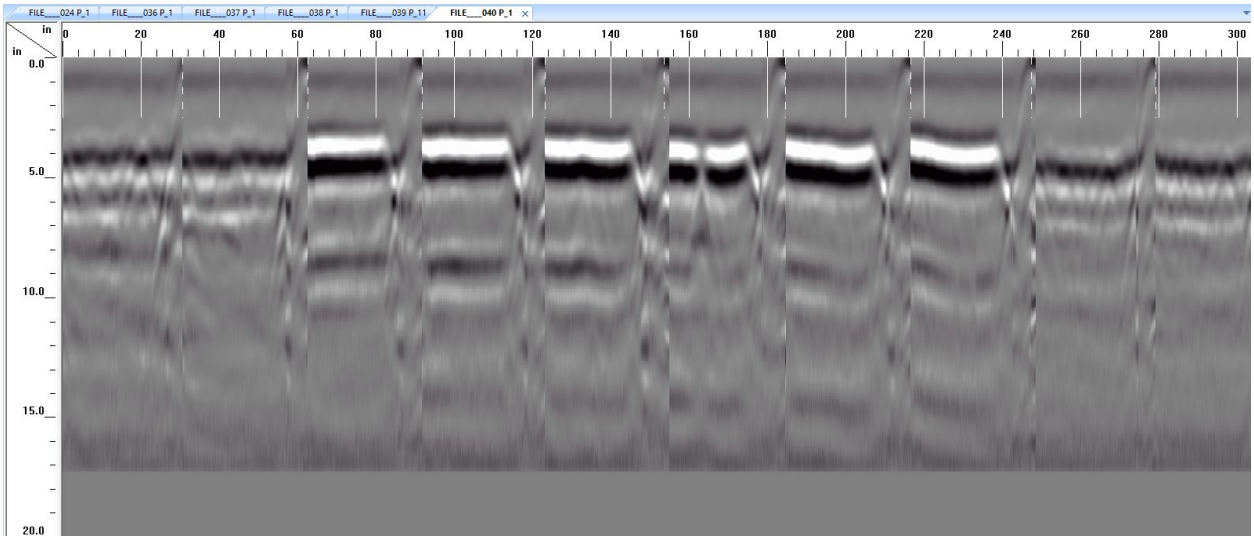

Figure 121: Slab 3 – Hour 11.5 Scan Outputs (X-Direction)

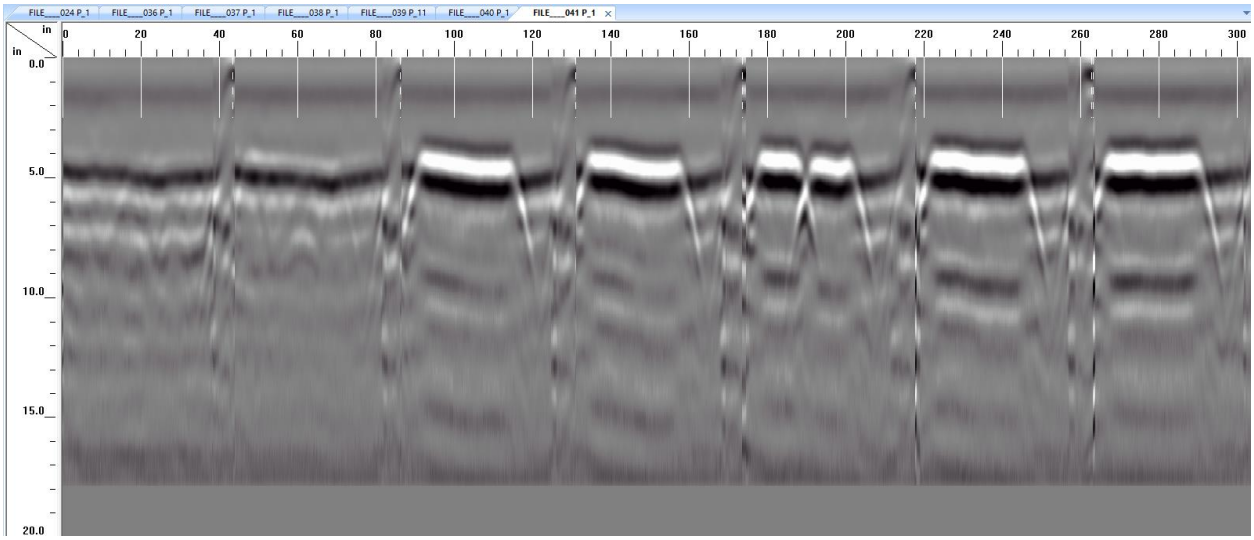

Figure 122: Slab 3 – Hour 11.5 Scan Outputs (Y-Direction)

Hour 12.5

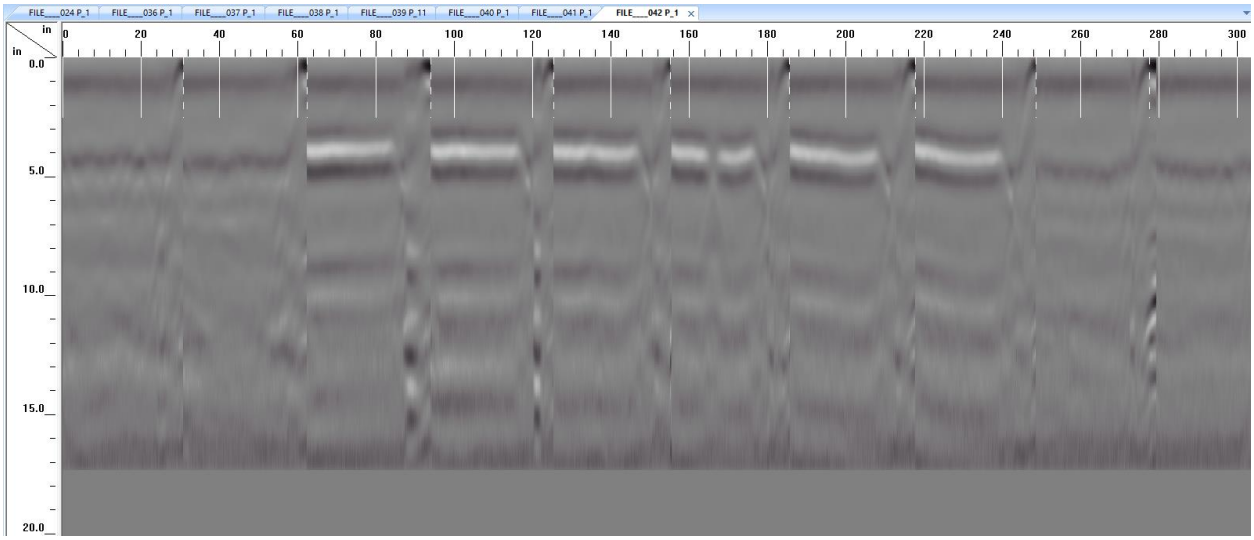

Figure 123: Slab 3 – Hour 12.5 Scan Outputs (X-Direction)

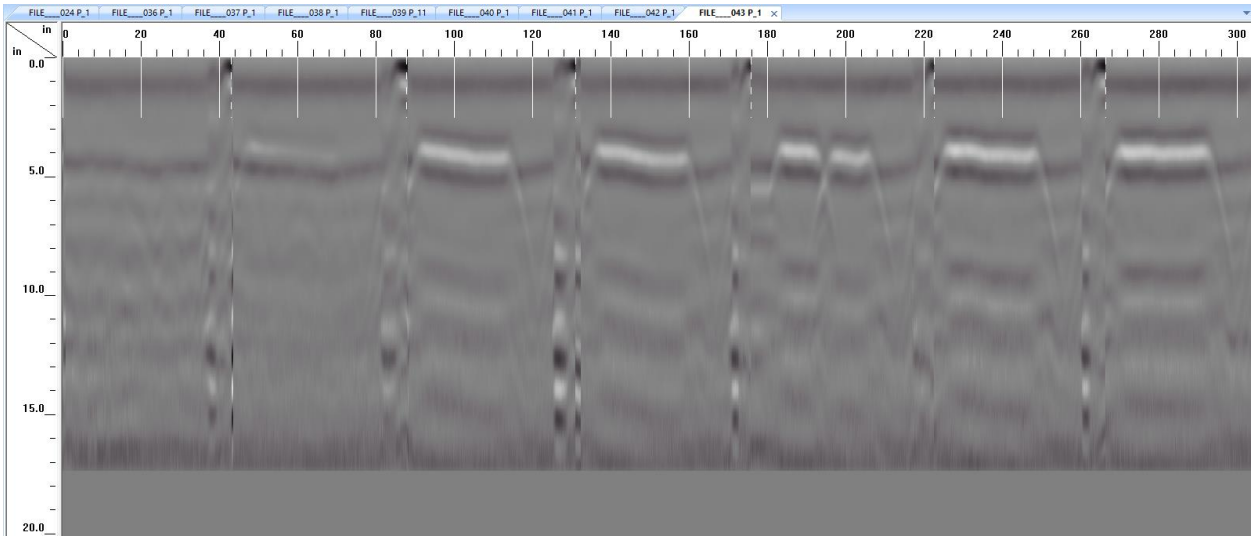

Figure 124: Slab 3 – Hour 12.5 Scan Outputs (Y-Direction)

Hour 13.5

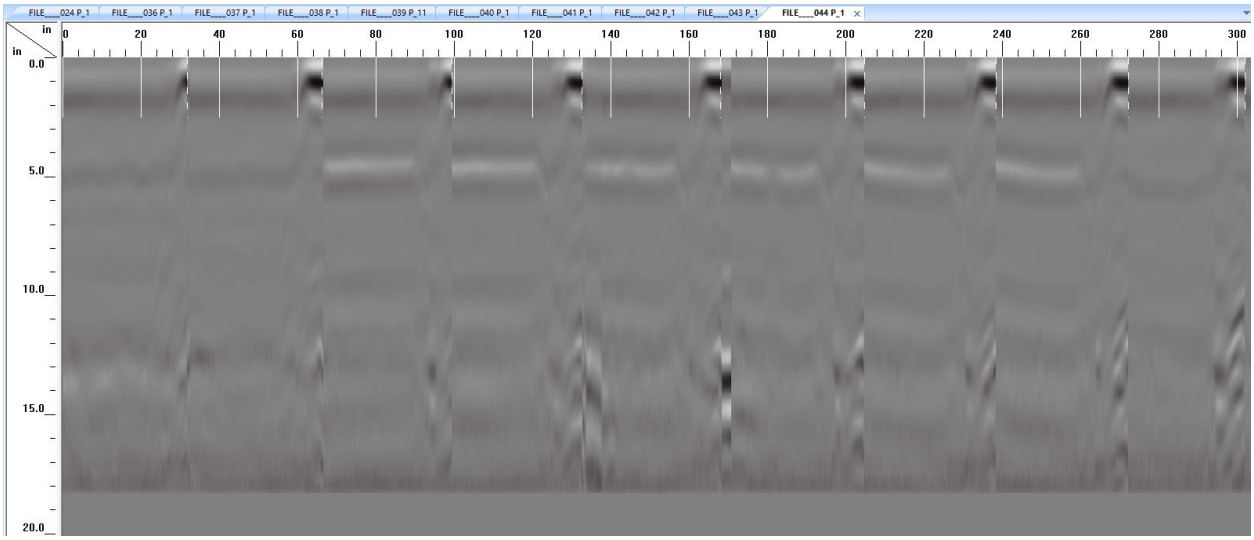

Figure 125: Slab 3 – Hour 13.5 Scan Outputs (X-Direction)

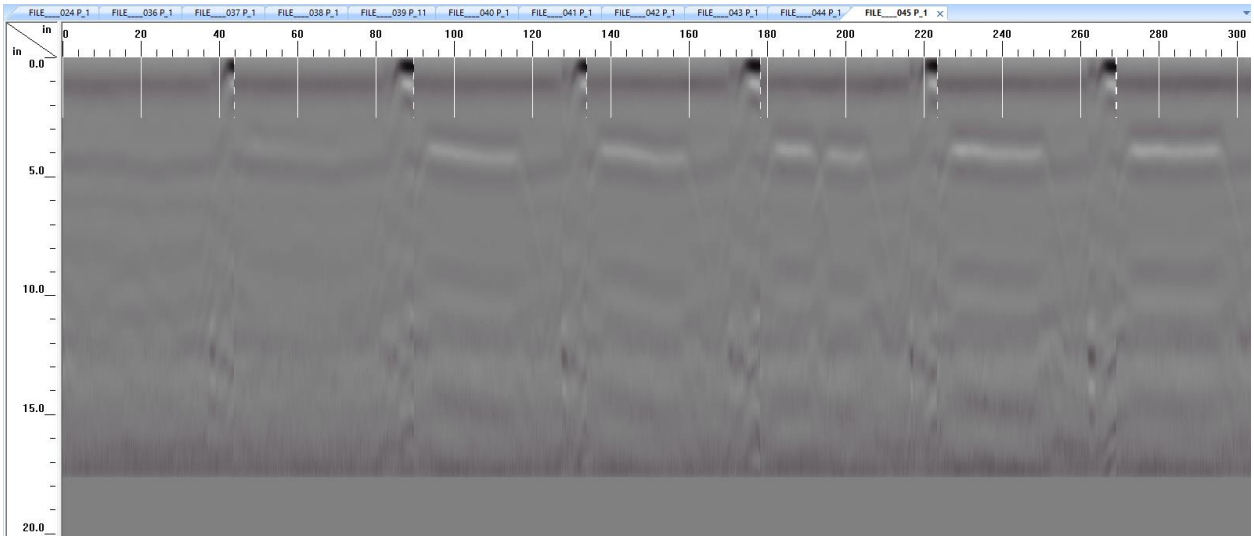

Figure 126: Slab 3 – Hour 13.5 Scan Outputs (Y-Direction)

Hour 14.5

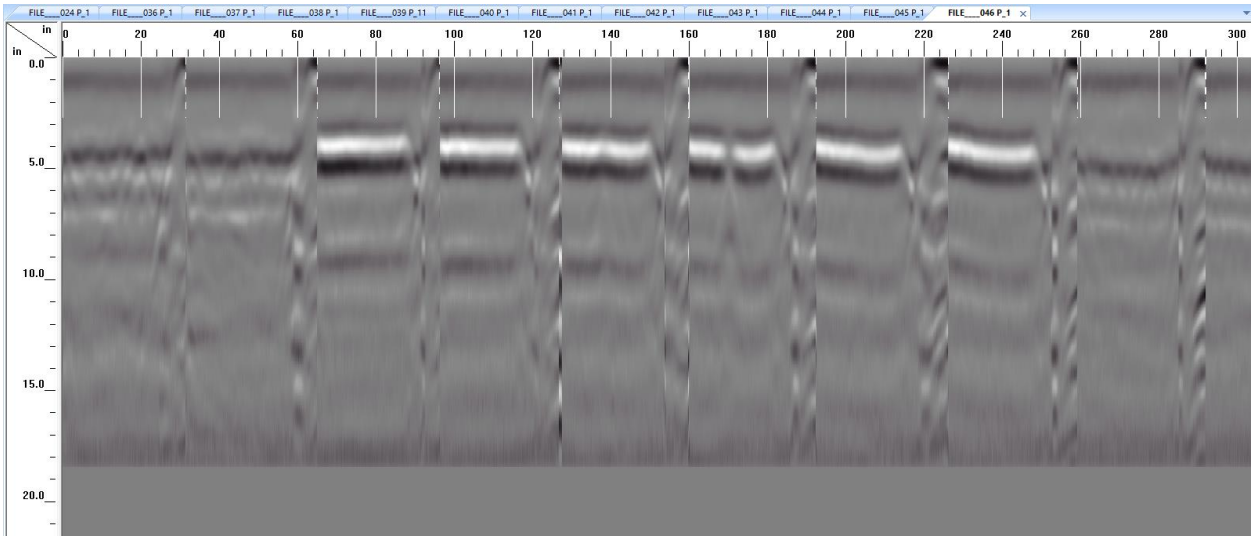

Figure 127: Slab 3 – Hour 14.5 Scan Outputs (X-Direction)

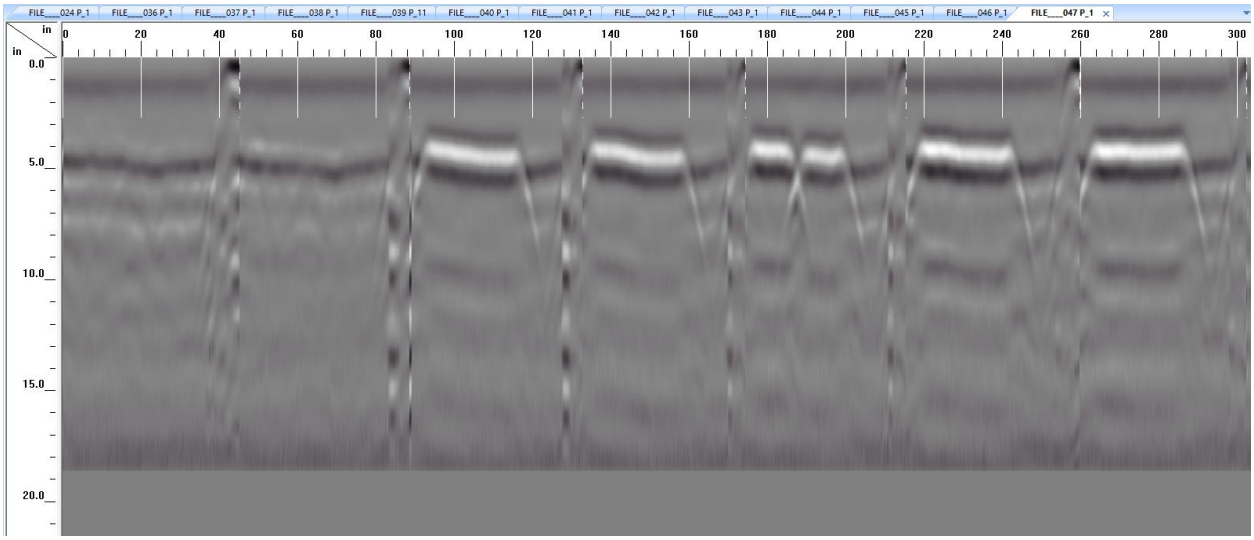

Figure 128: Slab 3 – Hour 14.5 Scan Outputs (Y-Direction)

Hour 15.5

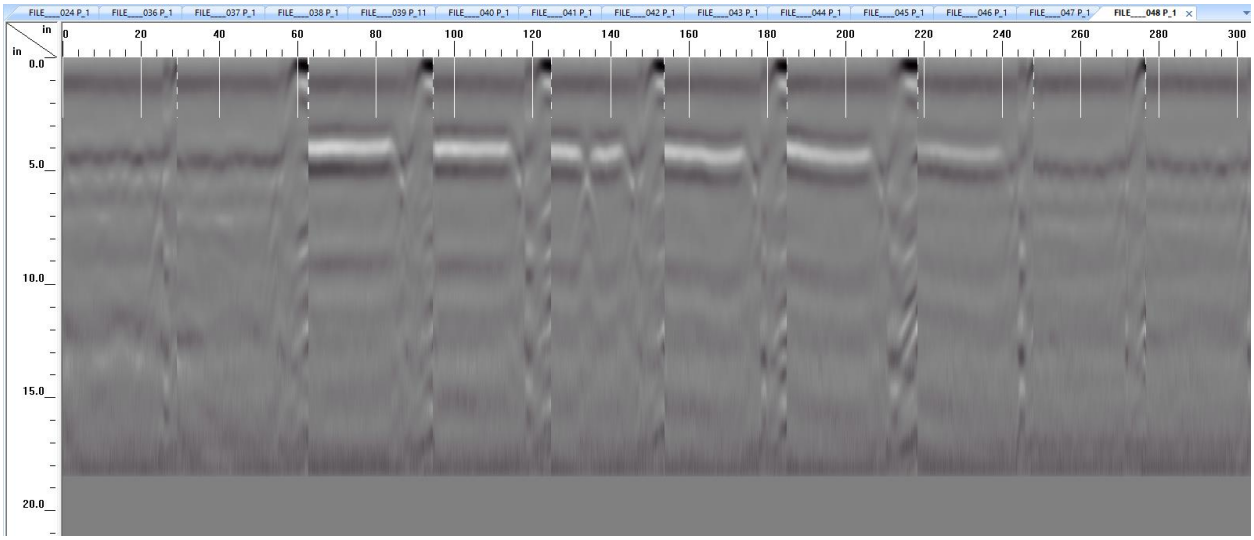

Figure 129: Slab 3 – Hour 15.5 Scan Outputs (X-Direction)

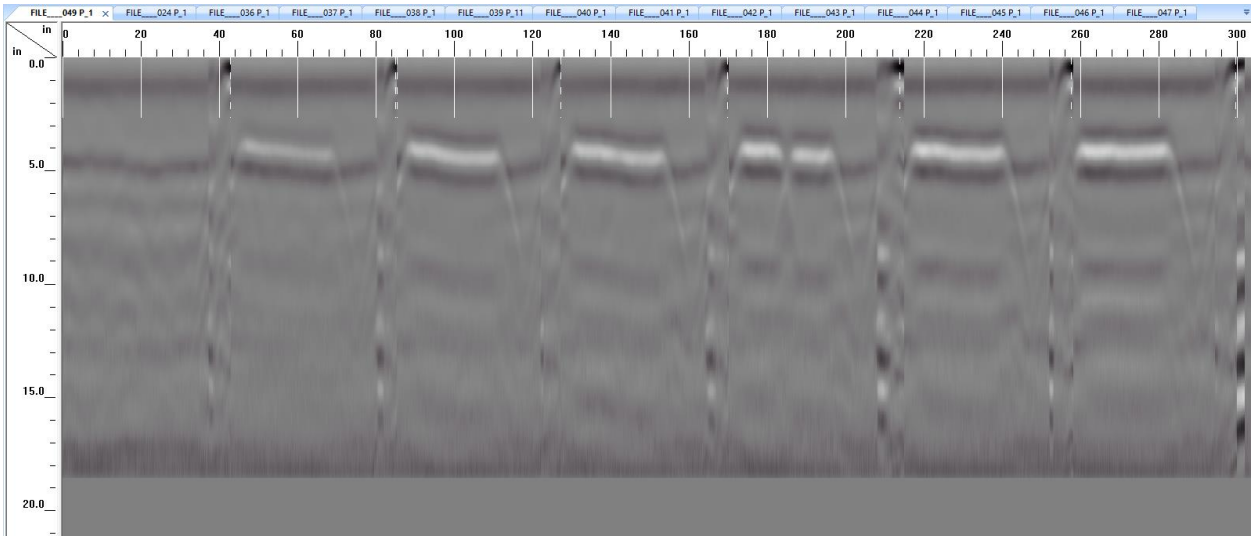

Figure 130: Slab 3 – Hour 15.5 Scan Outputs (Y-Direction)

Hour 16.5

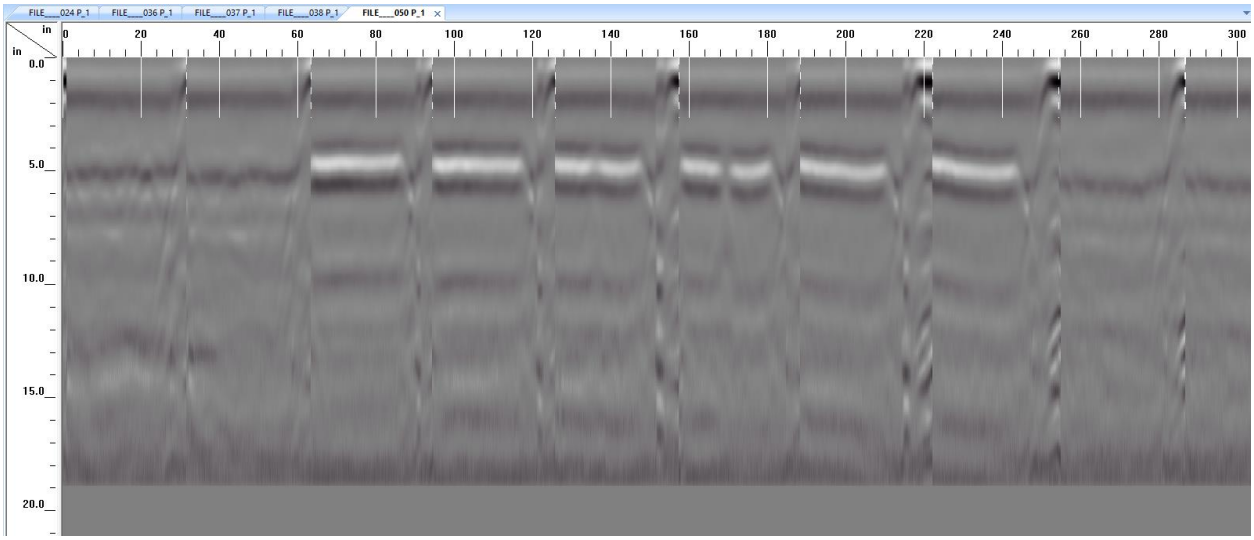

Figure 131: Slab 3 – Hour 16.5 Scan Outputs (X-Direction)

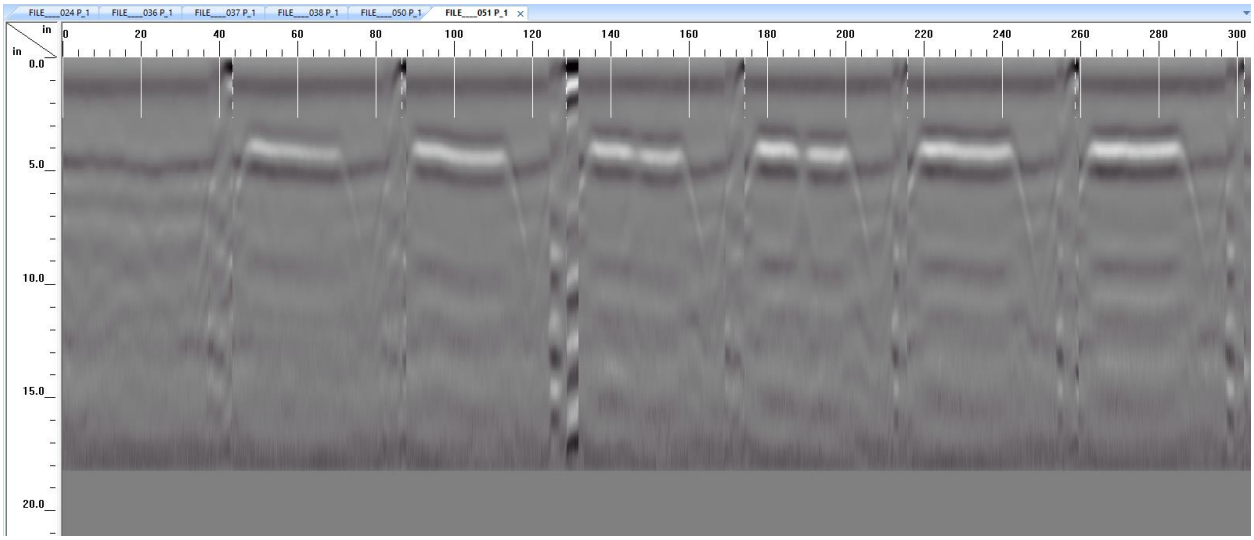

Figure 132: Slab 3 – Hour 16.5 Scan Outputs (Y-Direction)

Hour 17.5

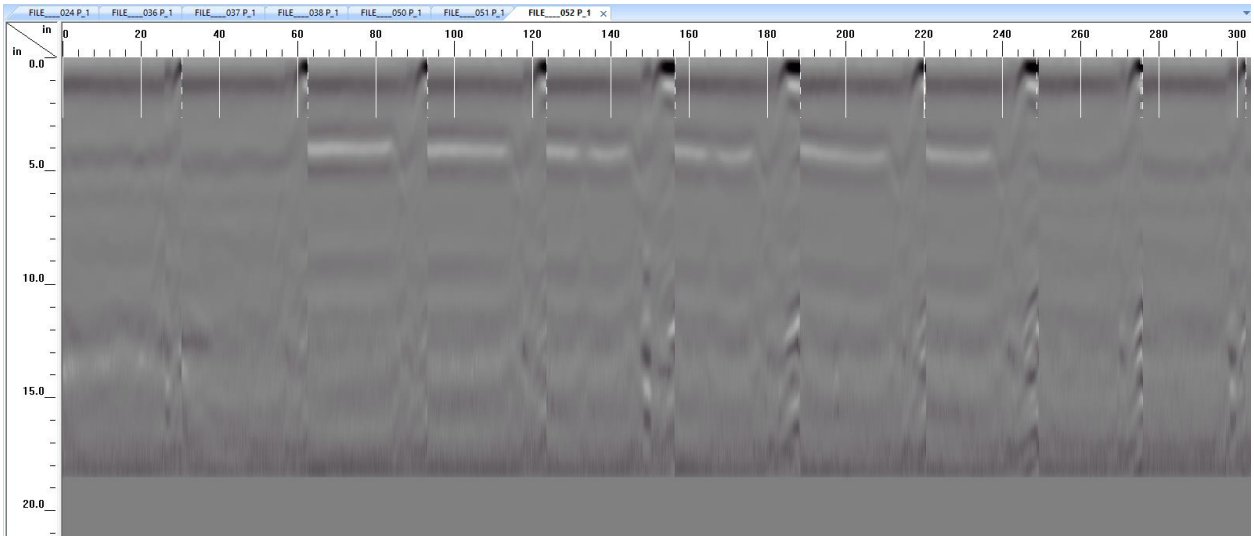

Figure 133: Slab 3 – Hour 17.5 Scan Outputs (X-Direction)

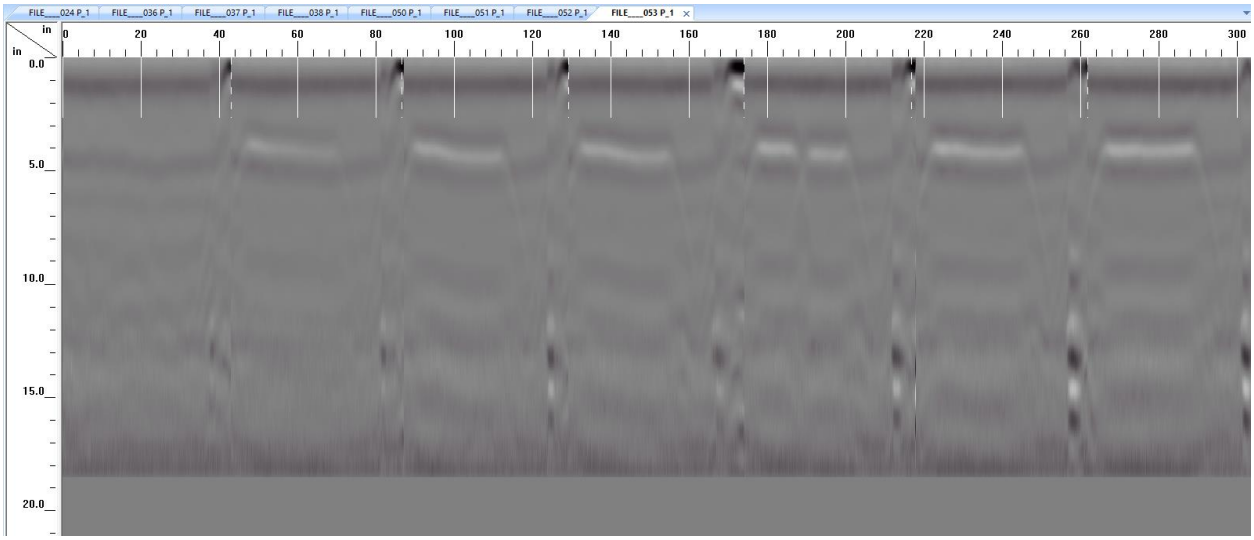

Figure 134: Slab 3 – Hour 17.5 Scan Outputs (Y-Direction)

Hour 18.5

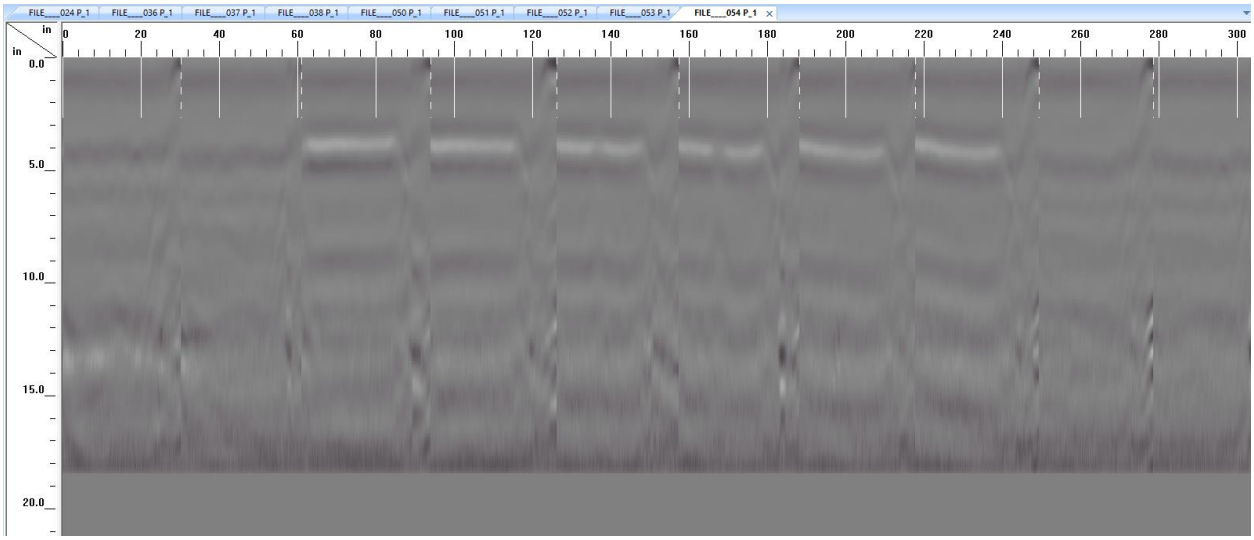

Figure 135: Slab 3 – Hour 18.5 Scan Outputs (X-Direction)

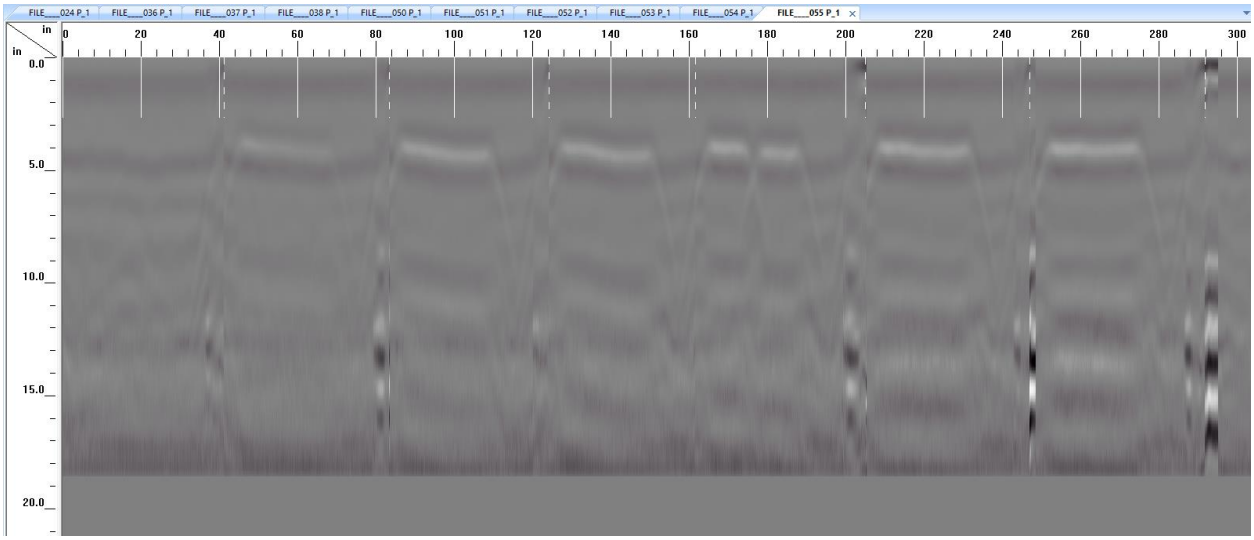

Figure 136: Slab 3 – Hour 18.5 Scan Outputs (Y-Direction)

Hour 19.5

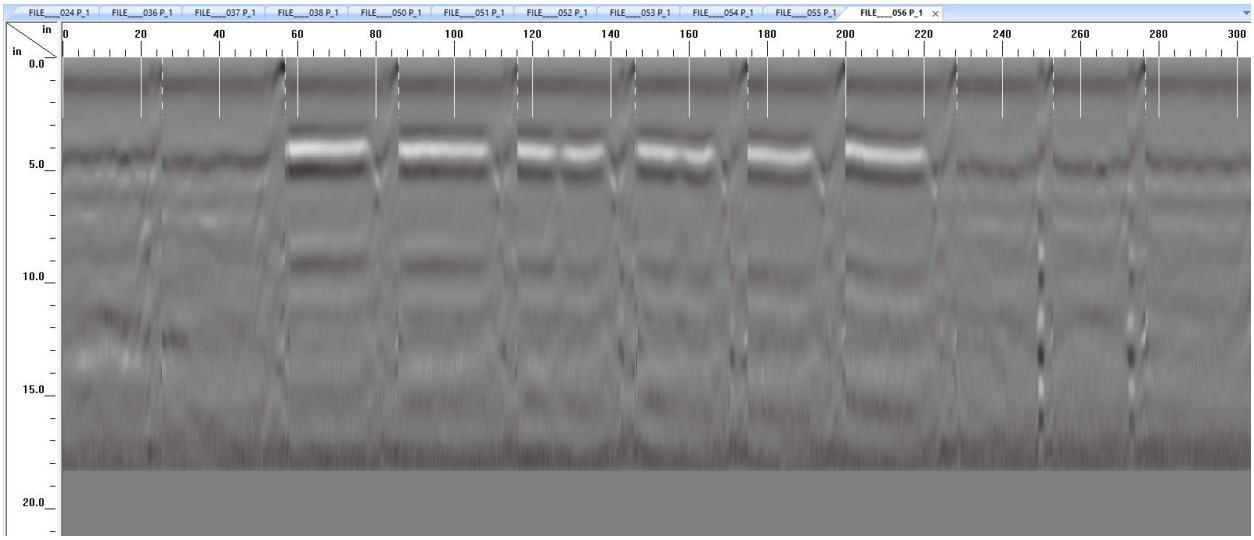

Figure 137: Slab 3 – Hour 19.5 Scan Outputs (X-Direction)

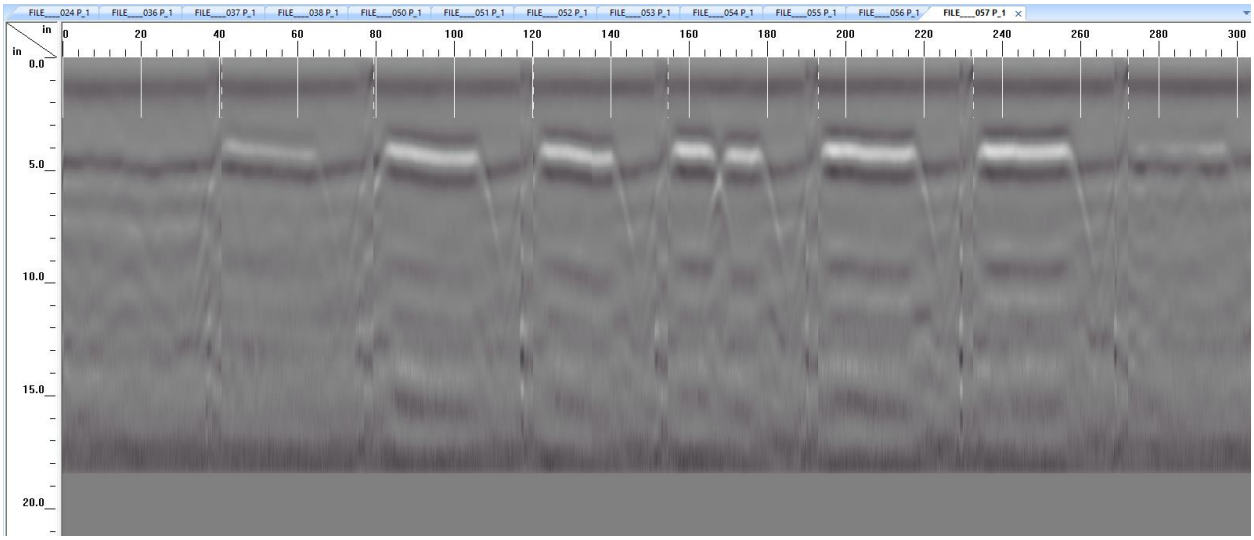

Figure 138: Slab 3 – Hour 19.5 Scan Outputs (Y-Direction)

Hour 20.5

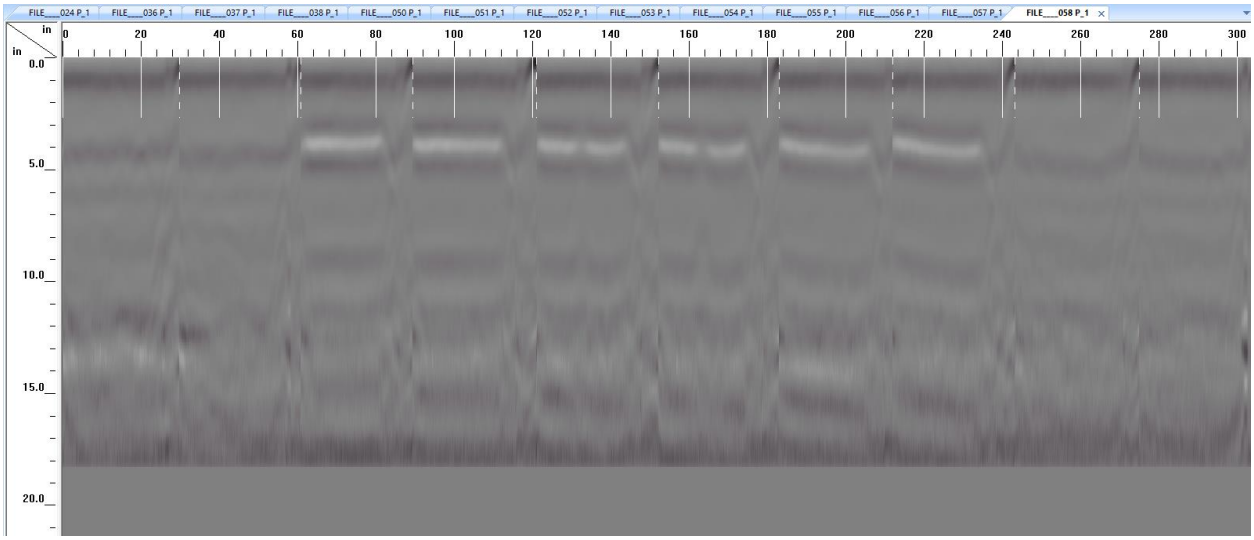

Figure 139: Slab 3 – Hour 20.5 Scan Outputs (X-Direction)

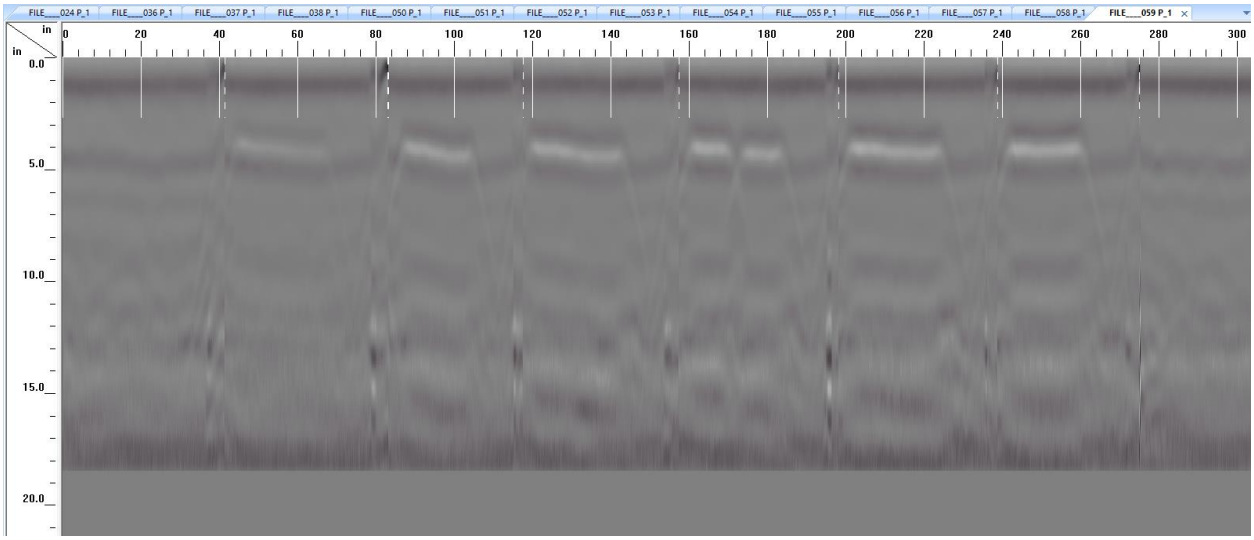

Figure 140: Slab 3 – Hour 20.5 Scan Outputs (Y-Direction)

Hour 21.5

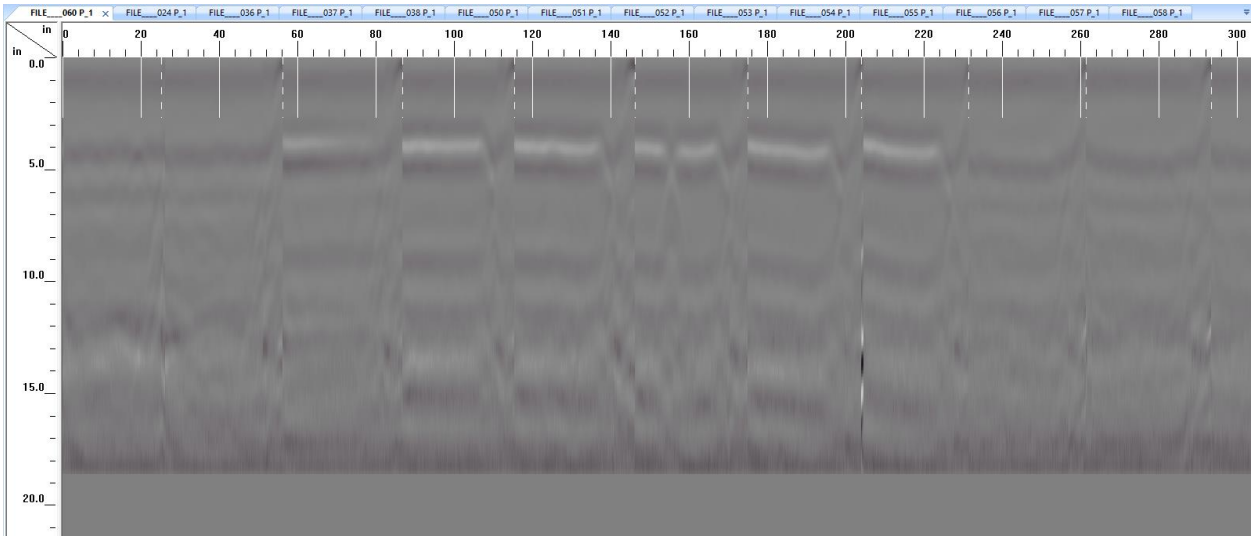

Figure 141: Slab 3 – Hour 21.5 Scan Outputs (X-Direction)

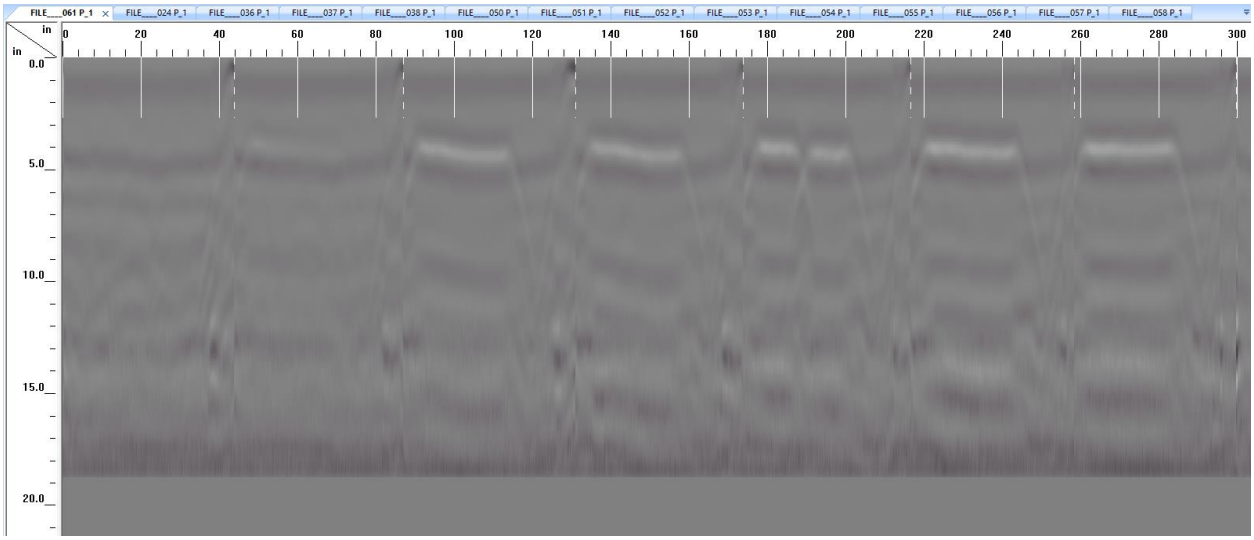

Figure 142: Slab 3 – Hour 21.5 Scan Outputs (Y-Direction)

Hour 22.5

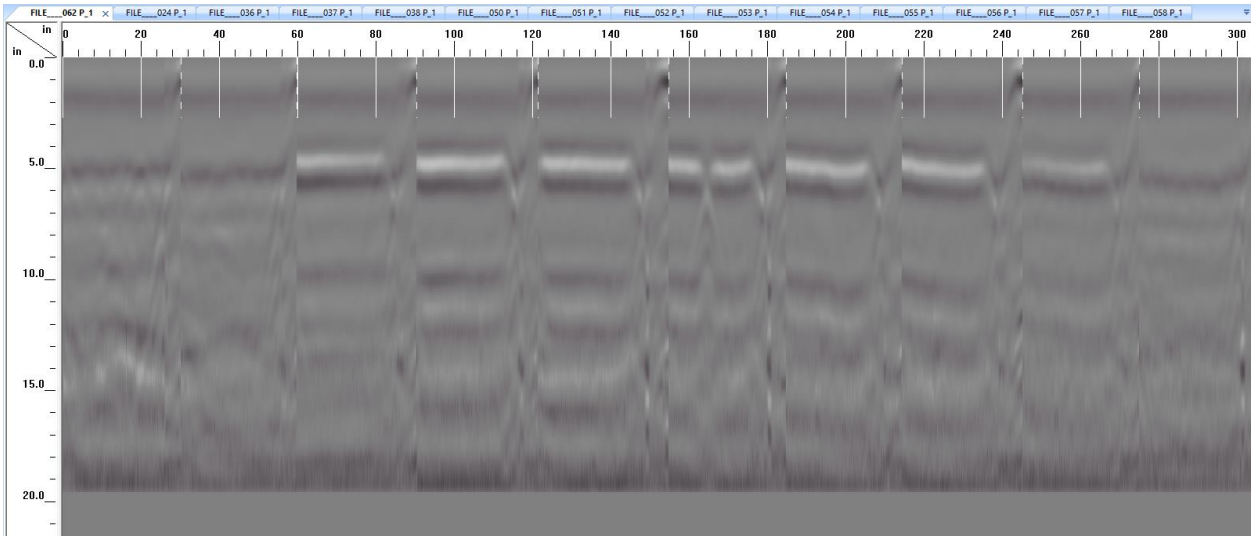

Figure 143: Slab 3 – Hour 22.5 Scan Outputs (X-Direction)

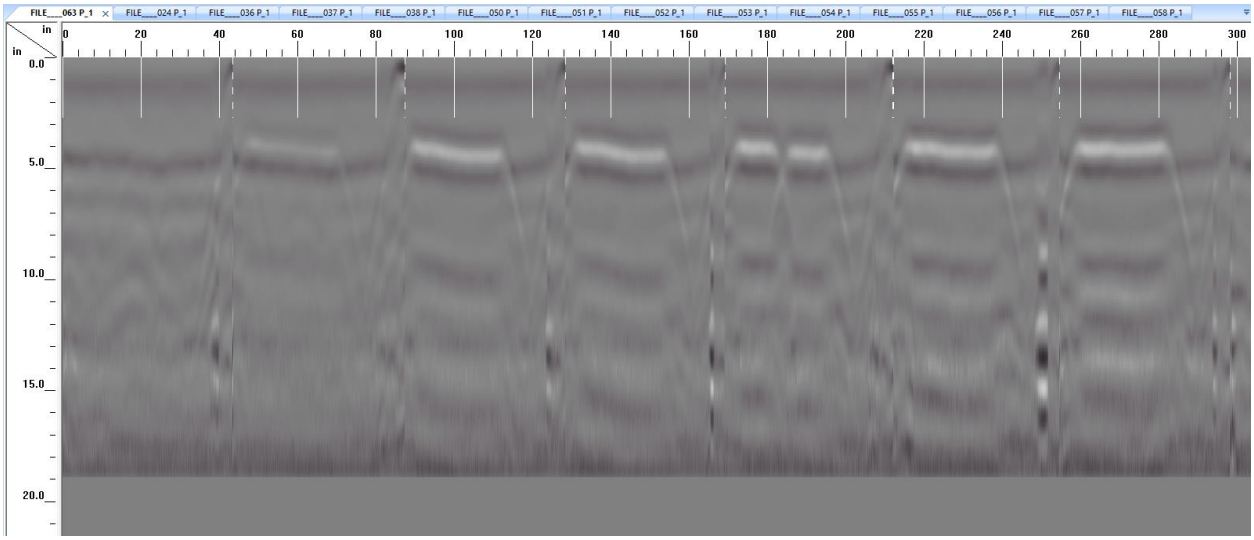

Figure 144: Slab 3 – Hour 22.5 Scan Outputs (Y-Direction)

Hour 23.5

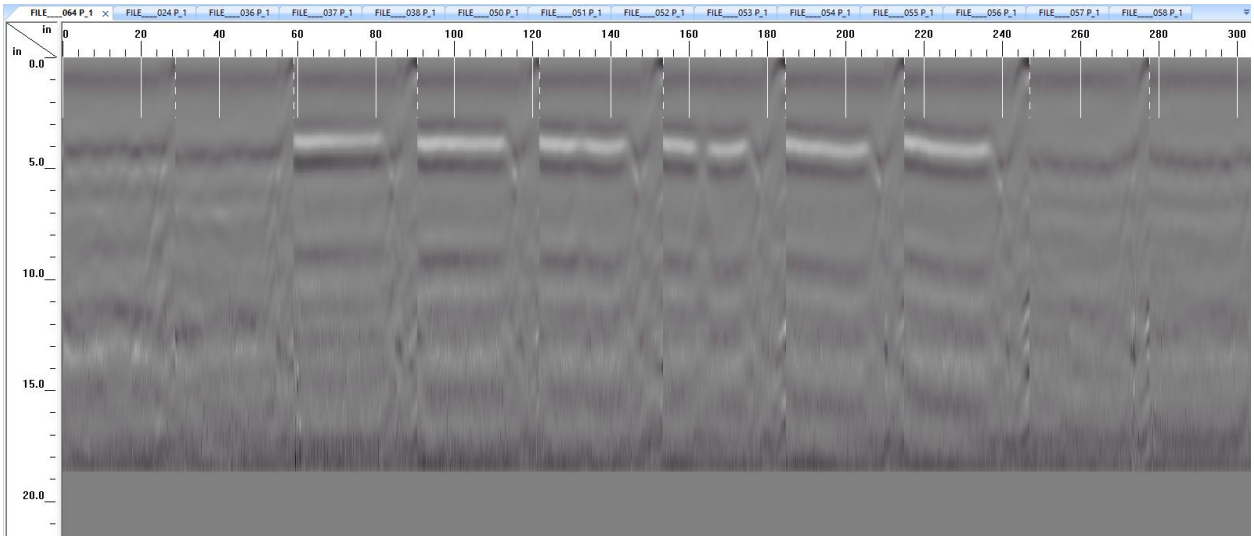

Figure 145: Slab 3 – Hour 23.5 Scan Outputs (X-Direction)

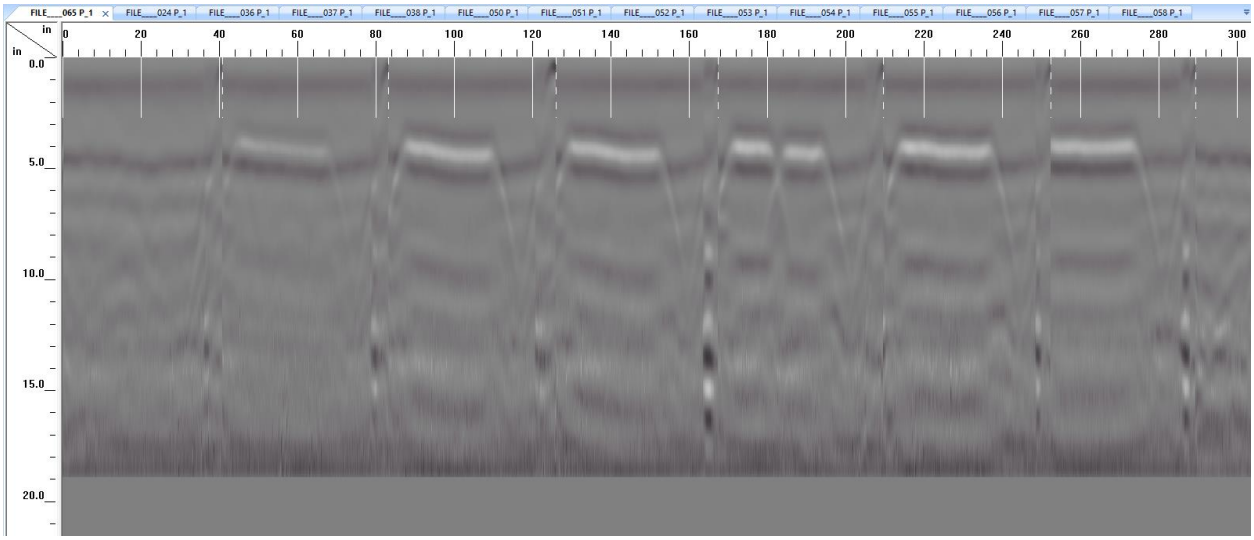

Figure 146: Slab 3 – Hour 23.5 Scan Outputs (Y-Direction)